NEUROLOGICAL APPLICATIONS OF QUANTITATIVE MAGNETIC RESONANCE IMAGING

By

CÉCILE M. MOHR

A DISSERTATION PRESENTED TO THE GRADUATE SCHOOL
OF THE UNIVERSITY OF FLORIDA IN PARTIAL FULFILLMENT
OF THE REQUIREMENTS FOR THE DEGREE OF
DOCTOR OF PHILOSOPHY

UNIVERSITY OF FLORIDA

2000

To my brother Stéphane.

ACKNOWLEDGMENTS

The interdisciplinary aspect of this work characterizes the nature of magnetic resonance research applied to the medical field. This Ph.D. would not have been possible without the help of many people who I would like to acknowledge today.

First, I would like to thank Dr. Stephen Blackband who took me into his laboratory. Steve has always been there for discussions and advice and, through his supervision, has helped develop my critical and scientific approach.

I would like to give particular thanks to Dr. Christiana Leonard who introduced me to Steve and oriented the functional MRI research, and provided financial and moral support throughout this work. Next, I would like to acknowledge Dr. Hazel Jones for her involvement in the hydrocephalus project and in particular with the shunt and sham operations. She has been active not only in the biological aspects of the study but also in the magnetic resonance approach. Finally, I would like to acknowledge the remaining committee members, Dr. Wesley Bolch, Dr. David Hintelang and Dr. Jeffrey Fitzsimmons. Their constructive comments and encouragement have been greatly appreciated.

Several people have contributed to the work presented in this dissertation. I would like to acknowledge.

For the auditory fMRI project (chapter 2): Dr. Wayne King who built the sound-delivery system; Dr. Richard Briggs who provided us with the original pulse sequences and advised our team throughout the study; Dr. Alan Freeman who adapted the acquisition protocol, acquired the data, trained me on the MRI scanner and taught me that "there is nothing like a good shim", Dr. Douglas Noll who provided the University of Florida with the spiral imaging sequence; Dr. Jintong Mao who implemented the sequence on the scanner.

For the hydrocephalus project (chapters 3 to 5): Jonathan Bui, Xeve Silver and Emma Mercer who shared their knowledge of experimental set-up with me; Barbara Beck for teaching me RF design and providing her coils for the experiment; Barbara Carter who provided and monitored the animals during the experiment, and gave useful input on the experimental set-up; Jamie Depelteau for help during imaging experiments; Wendy Norman for her assistance with the hydration measurements and the fluid supplementation protocol. Finally, I would like to acknowledge Jim Rocca, Dan Plant and Dr. Benjamin Inglis for their help on the 4.7T scanner.

I would also like to recognize Dr. David Buckley for useful discussions, particularly concerning the biexponential analysis performed in chapter 5. He always took the time to answer my questions and I respect him greatly despite the fact he "never understood what T_1 really is". Thanks also go to Dr. Peter Thelwall for providing a review of parts of this manuscript.

I would like to add special thanks to Carol Tsekouras. Carol is an invaluable asset to the Center for Structural Biology and I want to recognize her for the wonderful person she is and the great work she has been doing all these years.

I would like to acknowledge the faculty and staff of the department of Nuclear and Radiological Sciences, particularly Ms. Beth Bruce, who guided me throughout my studies at the University of Florida.

Finally, I would like to thank my friends, Dr. Didem Göçkay, Dr. Elizabeth Bossart, Dr. Sarah Kortenkamp, Dr. Alexandra Rapaport, and the aikido club (Linda, Kris, Die). Foreign thanks go to Christos and my other Greek friends and to my French friends (Lionel, Djamel, and all the others) from the "I-NNN-PEE-GEE" (Institut National Polytechnique de Grenoble, France), who helped me keep my sanity while pursuing this work in its final stages.

Last but not least, I would like to acknowledge my family: my father and mother Roger and Claudine Mohr, who have always been there for me in times of doubt and enthusiasm; my brother Stéphane, and my brother Vincent and his fiancée Annika, for their love and friendship.

TABLE OF CONTENTS

ACKNOWLEDGMENTS iii

LIST OF TABLES x

LIST OF FIGURES xii

LIST OF ABBREVIATIONS xiv

ABSTRACT xvii

CHAPTERS

page
1 QUANTITATIVE MAGNETIC RESONANCE IMAGING 1

- Introduction 1
- First Principles of Magnetic Resonance Imaging 2
  - Resonance of the Hydrogen Nucleus 2
  - Relaxation Processes 4
  - Basic Imaging 7
- Introduction to Functional Magnetic Resonance Imaging 16
  - Introduction 16
  - Blood Oxygenation Dependent Imaging 16
  - BOLD Contrast and Brain Activation 17
  - Functional Magnetic Resonance Imaging Experiments 19
- Principles of T_2 Mapping 20
  - Introduction 20
  - Mapping Principles 20
  - Mono- and Biexponential Models 21
  - Considerations on the Use of Multiple Echoes Sequences 22
- Principles of Diffusion Mapping 25
  - Diffusion Processes in Biological Tissues 25
  - Apparent Diffusion Coefficient Mapping Sequences and Parameters 26
  - Limits of the Monoexponential Model 27
  - Protocol Selection for ADC Mapping 30
- Conclusion 32

2 INFLUENCE OF SPEECH INTENSITY ON THE ACTIVATION OF AUDITORY CORTEX DETECTED BY MRI 33

Introduction 33
Materials and Methods 35
  Subjects 35
  Selection of Stimuli and Sound Delivery Set-up 35
  Selection of Intensity Levels and Experimental fMRI Design 36
  Imaging Protocol 38
  Data Processing 38
  Data Analysis 40
Results 41
  Intensity Level and Intelligibility 41
  Reproducibility 42
  Activation Pattern 43
  Effect of Intensity Level 46
Discussion 49
  Intelligibility and Sound Intensity 49
  Intra- and Intersubject Variability 49
  Lateralization of Activation 50
  Influence of Stimulus Intensity and Intelligibility 51
Conclusion 53

3 MONOEXPONENTIAL T_2 AND ADC MAPPING OF BRAIN MATURATION IN NORMAL AND HYDROCEPHALIC H-TX RATS 55

Introduction 55
  What is Hydrocephalus? 55
  Animal Models for Hydrocephalus 56
  Previous MR Studies on Hydrocephalus 57
Materials and Methods 60
  Animals 60
  Imaging Protocol 60
  Data Analysis 61
Results 64
  General Observations 64
  ADC measurements 65
  T_2 Measurements 66
  Anatomical Measurements 69
  Verification of Anatomical Measurements 70
  Reproducibility of T_2 Measurements 70
Discussion 72
  Anatomical Measurements 72
  Monoexponential Measurements of ADC 72
  Monoexponential Measurements of T_2 73
  Brain T_2 Relaxation Times 75

Maturation-related T_2 Changes 76
Regional Differences 78
Hydrocephalus-related T_2 Changes 78
Rates of Change of T_2 80
Conclusion 80

4 MONOEXPONENTIAL T_2 MAPPING FOR MONITORINGOF SHUNT TREATMENT OF NEONATAL HYDROCEPHALIC H-TX RATS 82

Introduction 82
Materials and Methods 84
Animals 84
Imaging Protocol 86
Data Analysis 87
Results 88
Shunt Efficiency 88
General Observations 89
Regional and Temporal Differences 90
Contributions of each Factor 94
Hydration Level 96
Discussion 97
Animal Groups 97
Hydration Level 99
Effects of Repetitive Anesthesia and Fluid Supplements 99
Effects of Surgical Operation 101
Effects of the Release of Intracranial Pressure 102
Conclusion 105

5 BIEXPONENTIAL T_2 AND ADC MAPPING OF BRAIN MATURATION IN NORMAL AND HYDROCEPHALIC H-TX RATS 106

Introduction 106
Multiexponential T_2 Studies 106
Multiexponential Diffusion Studies 108
Rationale and Aims of Biexponential Studies of H-Tx brain Maturation 111
Materials and Methods 112
Animals 112
Temperature Control 112
Immobilization Device 112
Sequence Selection 113
In vivo Data Analysis 116
Results 117
Animal Set-up 117
Phantom T_2 Measurements 118
In Vivo T_2 Measurements 121
Diffusion Measurements 123
Discussion 128

Animal Set-up 128
T_2 Measurements 128
Monoexponential tr(ADC) Measurements 130
Biexponential tr(ADC) Measurements 131
Conclusion 134

6 SUMARY AND CONCLUSIONS 136

Summary 136
Auditory Functional MRI 136
Brain Maturation 137
Monitoring of Shunt Treatment 138
Conclusion 139

APPENDIX A REGIONAL T_2 MATURATION CHANGES 140

APPENDIX B REGIONAL T_2 CHANGES FOR CON, HON, CNF CNN, COF AND HOF ANIMAL GROUPS 141

APPENDIX C REGIONAL MATURATION CHANGES OF MONO- AND BIEXPONENTIAL ADC IN CONTROL AND HYDROCEPHALIC RATS 146

APPENDIX D LIST OF PUBLICATIONS 151

REFERENCES 154

BIOGRAPHICAL SKETCH 165

LIST OF TABLES

Table Page

2-1: Reproducibility of activation. ..43

2-2: Number of subjects demonstrating activation in STS, PT and HG. ..45

2-3: Mean percent signal change for "repeated" voxels at the lowest and highest stimulus intensity. ..47

2-4: Individual percent signal change for "repeated" voxels at the lowest and highest stimulus intensity ..48

3-1: Mean $ADC_{inf/sup}$ in all ROIs at the 3 ages. ..65

3-2: Mean $ADC_{ri/le}$ in all ROIs at the 3 ages. .65

3-3: Accuracy of anatomical measurements. .71

3-4: Reproducibility of T_2 measurements in the 4 ROIs. .71

4-1: Number of animals included in the study. .90

4-2: Residual T_2 change due to fluid supplements, operation and hydrocephalus .95

4-3: Mean protein concentration in the CNF and CNN group. .97

4-4: Potential sources of T_2 changes for each animal group… .98

4-5: Semi-quantitative effects of the different phenomena on T_2. 103

5-1: Biexponential analysis of *in vivo* adult and 9-day-old rat. 113

5-2:Results of the T_2 phantom experiments. 124

5-3:Mean T_2 in normal and hydrocephalic rats 125

5-4: Mean tr(ADC) averaged over all ROIs in normal and hydrocephalic rats. 124

5-5: Mean tr(ADC) in each ROI in normal and hydrocephalic rats 129

5-6: Mean f_{fast}, tr(ADC_{fast}) and tr(ADC_{slow}) averaged over all ROIs in normal and hydrocephalic rats 130

5-7: Mean f_{fast}, tr(ADC_{fast}) and tr(ADC_{slow}) in each ROI in nol and hydrocephalic rats 131

A-1: Mean T_2 in the PC of normal and hydrocephalic rats 140

A-2: Mean T_2 in the AC of normal and hydrocephalic rats 140

A-3: Mean T_2 in the BG of normal and hydrocephalic rats 140

A-4: Mean T_2 in the TH of normal and hydrocephalic rats 140

B-1: Mean T_2 in the PC of the control CON, HON, CNF, CNN, COF and HOF groups 141

B-2: Mean T_2 in the AC of the control CON, HON, CNF, CNN, COF and HOF groups 142

B-3: Mean T_2 in the BG of the control CON, HON, CNF, CNN, COF and HOF groups 142

B-4: Mean T_2 in the TH of the control CON, HON, CNF, CNN, COF and HOF groups 143

B-5: Mean rate of change of T_2 in the PC of the control CON, HON, CNF, CNN, COF and HOF groups 143

B-6: Mean rate of change of T_2 in the AC of the control CON, HON, CNF, CNN, COF and HOF groups 144

B-7: Mean rate of change of T_2 in the BG of the control CON, HON, CNF, CNN, COF and HOF groups 144

B-8: Mean rate of change of T_2 in the TH of the control CON, HON, CNF, CNN, COF and HOF groups 145

C-1: Mean ADC (read-phase direction) in the PC of normal and hydrocephalic rats 146

C-2 Mean ADC (read-slice direction) in the AC of normal and hydrocephalic rats 147

C-3 Mean ADC (phase-slice direction) in the BG of normal and hydrocephalic rats 147

C-4: Mean f_{fast}, ADC_{fast} and ADC_{slow} (phase-slice direction) in the TH of normal and hydrocephalic rats 148

C-5 Mean f_{fast}, ADC_{fast} and ADC_{slow} (read-phase direction) in the PC of normal and hydrocephalic rats 149

C-6 Mean f_{fast}, ADC_{fast} and ADC_{slow} (read-slice direction) in the AC of normal and hydrocephalic rats 150

LIST OF FIGURES

Figure Page

1-1: Energy diagram for a ^{1}H nucleus placed in a strong magnetic field B_0 2

1-2: Timing diagram and k-space representation of a conventional spin-echo sequence. 12

1-3: Timing diagram and k-space representation of the multi-echo sequence 13

1-4: Timing diagram and k-space representation of the RARE sequence. 14

1-5: Timing diagram and k-space representation of a single-shot blipped-echo-planar imaging sequence. 15

1-6: Time course of the blood oxygenation level dependent MR signal. 18

1-7: Representation of water molecules in an in vivo sample 23

1-8: a) Monoexponential and b) biexponential decay curves. 23

1-9: Mechanisms of the stimulated echo. 25

1-10: Timing diagram of the spin-echo diffusion sequence 28

1-11: Schematic representation of isotropic and anisotropic diffusion 28

2-1: Auditory fMRI setup 36

2-2: Location of the functional slices and a typical pattern of activation. 40

2-3: Subject response curve to the detection task at the 5 intensity levels 42

2-4: Time course of auditory cortex voxels. 44

2-5: Individual volumes of repeated activation in the right and left hemispheres. 45

2-6: The repeated percent signal change, ΔS_{5rep}, as a function of intelligibility level. 47

3-1: Picture of two 4-day-old H-Tx rats 56

3-2: Sequence of pathological changes in hydrocephalic H-Tx rats in relation to normal maturational events. 59

3-3: T_2-weighted dataset of a hydrocephalic rat 62

3-4: Diffusion-weighted dataset of a hydrocephalic rat 62

3-5: Illustration of the ROI location 63

3-6: Regional comparisons of T_2 in control rat pups at three postnatal ages. 67

3-7: T_2 changes with age in control and hydrocephalic rats in 4 ROIs. 68

3-8: Graph of volume (cortical + sub-cortical structures) versus age. 70

3-9: T_2 versus cortical water content in the posterior cortex 77

4-1: Placement of a peritoneal shunt. 82

4-2: Three slices from a hydrocephalic rat pre-, 1, 4 and 6 days post-shunt 88

4-3: Changes of ventricular volume with age after shunt-treatment 89

4-4: T_2 changes in the 4 ROIs of the HON, CON, HOF and COF groups 91

4-5: Schematic representation of T_2 changes during normal maturation, following dehydration, shunt or sham operation. 104

5-1: Images of a control and hydrocephalic rat at the 8 b-values used in the study 119

5-2: Effect or the rare factor on phantom image quality. 119

5-3:MR signal decay with TE in a) a linear and b) a logarithmic plot 122

5-4:a) Uncorrected and b) corrected MR signal decay with the b-value. 124

LIST OF ABBREVIATIONS

AC: anterior cortex

ADC: apparent diffusion coefficient

ADC_{fast}: apparent diffusion coefficient of the fast diffusing water population

ADC_{slow}: apparent diffusion coefficient the slow diffusing water population

BG: basal ganglia

BOLD: blood-oxygenation level dependent

C: control

CBF: cerebral blood flow

CBV: cerebral blood volume

$cMRO_2$: cerebral metabolic rate of oxygen consumption

cMRgl: cerebral metabolic rate of glucose consumption

COF: control, operated, with fluid supplementation

CON: control, operated, no fluid supplementation

COV: coefficient of variation

CNF: control, not operated, with fluid supplementation

CNN: control, not operated, no fluid supplementation

CSF: cerebrospinal fluid

DW: diffusion-weighted

ECS: extracellular space

EPI: echo planar imaging

ES: echo spacing

ETL: echo train length

FA: flip angle

f_{fast}: volume fraction of the fast diffusing water population

FID: free induction decay

fMRI: functional magnetic resonance imaging

HC: hydrocephalus/hydrocephalic

HOF: hydrocephalic, operated, with fluid supplementation

HON: hydrocephalic, operated, no fluid supplementation

ICP: intracranial pressure

ICS: intracellular space

IL: intelligibility level

ME: multi-echo

MHz: mega Hertz

MR: magnetic resonance

MRI: magnetic resonance imaging

NFR: non-fluid replaced

NMR: nuclear magnetic resonance

PC: posterior cortex

RARE: rapid relaxation enhancement

RF: radio frequency

ROI: region of interest

SE: spin echo

SEM: standard error of the mean

SNR: signal to noise ratio

SO: sham-operated

δ: duration of diffusion gradients

Δ: time between onset of diffusion gradients

T: tesla

τ: diffusion time

T_1: spin-lattice relaxation time

T_1W: T_1-weighted

T_2: spin-spin relaxation time

T_2^*: effective T_2

T_2W: T_2-weighted

TE: echo time

TE_{eff}: effective echo time

TH: thalamus

TR: repetition time

tr(ADC): trace of the ADC

Abstract of Dissertation Presented to the Graduate School
of the University of Florida in Partial Fulfillment of the
Requirements for the Degree of Doctor of Philosophy

NEUROLOGICAL APPLICATIONS OF QUANTITATIVE MAGNETIC RESONANCE IMAGING

By

Cécile M. Mohr

May, 2000

Chairman: Wesley E. Bolch
Major Department: Nuclear and Radiological Engineering

Clinical magnetic resonance imaging (MRI) is currently used qualitatively by radiologists. To improve the value of MRI for basic scientists, quantitative approaches need to be developed and this is the topic of this dissertation. First, the implementation of human auditory functional MRI is presented. Secondly, mono- and biexponential water T_2 and diffusion measurements of hydrocephalic rat brain are reported during maturation and following shunt treatment.

Functional MRI (fMRI) allows brain function to be studied by observing changes in endogenous MRI contrast mechanisms. Although it has been widely used for the study of the motor and visual cortex, the observation of auditory cortex activity is challenging as the background scanner noise competes with stimulus presentation. This work presents an experimental set-up and data analysis scheme that was used to detect and assess the dependence of MR signal on speech sound intensity. Results showed that fMRI percent signal change increased with increasing speech intensity. These results will help assess the influence of basic stimulation parameters to take into account for more complex language studies,f

Hydrocephalus (HC) is characterized by an abnormally high accumulation of cerebrospinal fluid (CSF) in the ventricles, commonly treated by diverting into a body cavity (known as "shunting"). A non-acute model of hydrocephalus, the H-Tx rat model, was investigated and water T_2 and apparent diffusion coefficient (ADC) were measured. T_2 decreased dramatically with maturation and showed regional brain differences. The ADC also decreased significantly with maturation as the fast-diffusing water fraction, which is indicative of the size of extracellular space, decreased during development.

Although few T_2 differences were shown during maturation of control and hydrocephalic animals, differences in ADC indicated a transient increase followed by a decrease in the fast-diffusing water fraction of hydrocephalic rats. Shunt treatment data showed the need for fluid supplementation as T_2 was shortened by dehydration. In addition, reduced cortical T_2 decrease in hydrocephalic rats suggested CSF infiltration in the tissue after the operation. This work demonstrated that quantitative MRI techniques can monitor microscopic changes in the properties of the water during the development of progressive hydrocephalus and traumatic shunt treatment.

CHAPTER 1
QUANTITATIVE MAGNETIC RESONANCE IMAGING

Introduction

The magnetic resonance phenomenon was discovered by two independent researchers, Bloch and Purcell, in 1946, for which they were awarded the Nobel Prize in 1952. Until the seventies, nuclear magnetic resonance (NMR) was used for chemical analysis. In 1972, x-ray computed tomography was introduced in the field of radiology. This technique allowed reconstructing 2-dimensional images using a series of 1-dimensional projections. In 1973, Lauterbur presented the principles of magnetic resonance imaging (MRI) using NMR combined with the back-projection technique used in x-ray tomography (Lauterbur, 1973). In 1975, Ernst suggested a new way of encoding directional information, known as phase and frequency encoding, techniques which are still used today. In 1980, Edelstein *et al.* (1980) applied these methods and produced the first images of the body. Further improvements, which greatly reduced the acquisition times, were achieved during the eighties and brought MRI to the successful place that it has in radiology practice today.

Since the onset of diagnostic imaging in 1895 when x-rays were discovered, radiologists have made diagnoses on the basis of the gray scale representation of images. Despite a great success with MR images, the mechanism for contrast in some pathologies such as ischemia is not well understood. Therefore, to develop MRI as a more efficient diagnostic and research tool, it is necessary to understand the effects of biological phenomena on contrast and to develop indexes to evaluate the state of disease and recovery. This dissertation is inscribed in this framework and pursues the goal of developing reliable quantitative methods for MR brain imaging.

In this first chapter, the basics of MRI will be presented. Then the first principles of the three quantitative techniques used in this work, functional MRI, T_2 mapping and diffusion mapping, will be introduced. The conclusion will then introduce the specific aims of this dissertation.

First Principles of Magnetic Resonance Imaging

Resonance of the Hydrogen Nucleus

The hydrogen nucleus or proton (^1H) has an angular momentum (spin=½). Because of their charge and angular momentum, protons exhibit a nuclear magnetic moment. When placed in a static magnetic field $\mathbf{B_0}$, they experience the Zeeman interaction. For a nuclear spin of ½, the Zeeman interaction gives rise to two energy levels (figure 1-1). Spins in the lower energy level are parallel to $\mathbf{B_0}$, and spins in the higher energy level are oriented in the opposite direction to $\mathbf{B_0}$. At room temperature, the lower energy level is slightly more populated (~1 nucleus per million) than the higher one. Therefore, the sample, which can be described as a large ensemble of spins, exhibits a net magnetization $\mathbf{M_0}$.

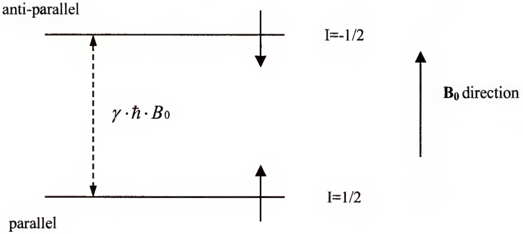

Figure 1-1: Energy diagram for a ^1H nucleus placed in a strong magnetic field B_0.

Each spin placed in a magnetic field is not statically aligned parallel or anti-parallel along $\mathbf{B_0}$ but precesses around $\mathbf{B_0}$, at a characteristic frequency ω_0. It can be shown using either a quantum or classical mechanics approach that this precession frequency ω_0, the Larmor frequency, is given by

$$\omega_0 = \gamma \cdot B_0 \qquad [1\text{-}1]$$

where ω_0 is in Hz, γ is the gyromagnetic ratio (42.6 MHz.T^{-1} for protons), and $\mathbf{B_0}$ is the main (and static) magnetic field strength (in T). At typical clinical and research field strengths of 1.5 T and 4.7 T, protons precess around $\mathbf{B_0}$ at a frequency of 64 MHz and 200 MHz, respectively. Although spins are precessing at the same frequency, they are not in phase. Therefore as a sample is placed in $\mathbf{B_0}$, the net magnetization $\mathbf{M_0}$, exhibits a resulting longitudinal (i.e., along $\mathbf{B_0}$) component, but no transverse (i.e., in the plane perpendicular to $\mathbf{B_0}$) component.

Relaxation Processes

When an oscillating magnetic field **B₁** produced by a radio frequency (RF) pulse and oscillating at the Larmor frequency ω_0, is applied perpendicularly to a main magnetic field $\mathbf{B_0}$, the spins enter a resonance phenomenon and the net magnetization is disturbed from its initial alignment. This process is called RF excitation. The power and duration of the pulse control the amount by which the net magnetization is rotated, that is the flip angle θ measured relative to the direction of $\mathbf{B_0}$. In addition, the spins, which were initially out of phase, are now in phase or in "coherence": the net magnetization exhibits a non-null transverse component $M_{x,y} = M_0.\ \sin(\theta)$, and a longitudinal component $M_z = M_0.\cos(\theta)$. By selecting imaging timing parameters, the echo time TE, the repetition time TR and flip angle FA, images with contrast based on T_1, T_2 or spin-density tissue differences can be acquired: such images are called T_1-weighted (T_1W), T_2-weighed (T_2W) or spin-density weighted images, respectively.

Classical description of T_1 and T_2

Upon termination of an RF pulse, the disturbed spin-system returns to equilibrium following relaxation processes. Relaxation is characterized by two phenomenological time constants presented in [1-2]: the longitudinal relaxation time T_1 and the transverse relaxation time T_2. T_1 and T_2 are also called the spin-lattice and the spin-spin relaxation times, respectively.

$$\begin{aligned} \frac{dM_z}{dt} &= -\frac{(M_z - M_0)}{T_1} \\ \frac{dM_{x,y}}{dt} &= -\frac{M_{x,y}}{T_2} \end{aligned} \qquad [1\text{-}2]$$

Equation [1-2] is the differential form of an exponential function with characteristic time-constants T_1 and T_2: following a 90° pulse excitation, T_1 is the time necessary for the sample longitudinal magnetization to recover 63% of its initial value. Similarly, T_2 is related to the rate of loss of the transverse magnetization and it is the time after which 63% of the transverse magnetization has been lost.

Quantum description of T_1 and T_2

In ^1H NMR, neighboring atoms and nuclei have local electric and magnetic fields that interact with nuclear magnetic dipoles. Therefore, relaxation mechanisms are due to magnetic dipole-dipole coupling.

Following RF stimulation, nuclei are brought to an excited (higher energy level) state. To return to their ground state, the nuclei need to dissipate their excess energy to the surroundings, which is also called the lattice. This process, "spin-lattice relaxation", is characterized by a time constant T_1, which is the time by which 63% of a population of nuclei will have returned to their ground state.

Nuclei in ground or excited states exchange energy with each other. Due to imperfections in the magnetic field, nuclei precess at slightly different frequencies and loose coherence. Contrary to T_1 relaxation, there is no net loss of energy during T_2 relaxation.

T_1, T_2 and correlation time

The process of energy dissipation is not spontaneous but requires stimulation by a RF field that is produced by other magnetic fields. In liquids, the RF field responsible for that stimulation is due to rotational and translational random thermal motion of neighboring nuclei (Brownian motion).

Although relaxation times are phenomenological, using a theory developed by Bloembergen, Purcell and Pound (Bloembergen *et al.*, 1948), the BPP theory, T_1 and T_2 can be related to τ_c the correlation time. τ_c is the minimum time for a molecule to rotate by one radian and represents the local interactions of the atoms and nuclei. In other words, the correlation time characterizes rotational motion. In water, there is a uniform distribution of energy as a function of frequency up to the frequency $1/\tau_c$. When the correlation time is long, nuclei are in contact long enough to exchange energy and therefore, relaxation is more efficient. However, when the correlation time is short, nuclei tumble too rapidly to exchange energy and the relaxation is inefficient. Another approach consists of examining the spectral density for different correlation times: at long correlation times, there are overall more nuclei tumbling at the frequency necessary to stimulate energy exchange than at short correlation times.

T_1 and T_2 are linked to molecular motion and therefore to τ_c . However, only exchange which transfers energy to the lattice contributes to T_1, while other interactions during which no net energy is lost contribute to T_2 (Bloembergen *et al.,* 1948).

T_2*, the effective spin-spin relaxation

T_2* is the observed T_2: it is the time-constant that characterizes the loss of transverse magnetization not only due to intrinsic nuclei interaction (which is T_2) but also due to spatial inhomogeneities in the main magnetic field. A practical example of the importance of T_2* in biological samples is when one considers oxygen in blood. Oxygenated hemoglobin is diamagnetic, it is negatively susceptible to magnetization by the external field, whereas deoxygenated hemoglobin is paramagnetic, that is a large magnetization is induced by the external field. When hemoglobin changes from its diamagnetic to its paramagnetic configuration, there is a decrease in T_2^* and the signal on T_2^*-weighted images increases.

Basic Imaging

Frequency encoding

Let's assume a homogeneous sample placed in a static magnetic field $\mathbf{B_0}$, on which is superimposed a linear magnetic field gradient G (in $mT.m^{-1}$). At any location x along the direction of G, the spins experience a magnetic field B(x) and precess at a spatially dependent frequency ω(x):

$$\begin{aligned} B(x) &= B_0 + G \cdot x \\ \omega(x) &= \gamma \cdot B(x) \end{aligned} \qquad [1\text{-}3]$$

Using this formula, spatially encoding an image in one direction is achieved by the following manipulation. A sample is excited and during signal detection, a gradient is turned on along **X**. The induced signal incorporates all the range of frequencies that was imposed by the application of the gradient where each frequency represents a location x, and its amplitude depicts the number of nuclei resonating at that frequency. These quantities, frequencies and their relative amplitude can be extracted from the signal by a mathematical transformation, the Fourier transform (FT). Through the FT, the time domain signal is transformed into 1-dimensional (1D) representation (i.e., projection) in the frequency domain. Because of the relationship between space and frequency, this frequency representation is equivalent to a spatial projection of the object along **X**. Since the signal is digitally sampled N_x times, once every δt_x, the phase ϕ_x of the signal arising from a tissue located at x is

$$\Phi_x(x, \delta t_x) = \gamma \cdot G_x \cdot \delta t_x \cdot x \qquad [1\text{-}4]$$

The gradient is referred as the frequency encoding gradient and its direction, noted conventionally as **X**, is referred as the read or frequency encoding direction.

Selective excitation

By simultaneously applying gradients and frequency selective radio-frequency pulses, it is possible to excite the spins in a specific region of the sample. The simplest case is called slice selection and is generally used to get a signal from a "slice" sometimes referred as a 2-dimensional (2D) plane as the thickness is much smaller than the other 2 dimensions. By applying a linear gradient along the **Z** direction, the nuclear spins in the plane located between z_0 and z_1 resonate at frequencies in the range of $[\omega_0+z_0.G_z.\gamma; \omega_0+z_1.G_z.\gamma]$. To specifically excite these spins, the excitation RF pulse is chosen to contain the same range of frequencies and is applied simultaneously with the **Z** gradient. By convention, the slice selection gradient direction assigned along **Z** results in the excitation of an **X-Y** plane.

Phase encoding

To perform imaging, it is necessary to code the remaining dimension, **Y**, the phase encoding direction. Phase encoding is typically performed using the "spin-warp" technique. Every time an excitation is repeated or what is called every repetition time (TR), the amplitude δG_y of the **Y** gradient is changed in incremental steps while its duration t_y is kept constant. The phase resulting from the application of such a gradient at the y location is

$$\Phi_y(y, \delta G_y) = \gamma \cdot \delta G_y \cdot t_y \cdot y \qquad [1\text{-}5]$$

To obtain an image with a matrix size of N_x by N_y points, it is necessary to acquire enough data points in order to extract the $N_x.N_y$ relative amplitudes emanating from each individual picture element (or pixel) located at (x;y). This is achieved by repeating the phase encoding steps N_y times with a different G_y every TR while performing N_x frequency encoding steps during each signal acquisition.

k-space

By generalizing the approach of phase and frequency encoding, we can now write the signal at a time t, obtained from a sample of spin density $\rho(\mathbf{r})$, where **r** is the vector position in the magnet, in the following terms:

$$\begin{aligned} &dS(\mathbf{G};t) = \rho(\mathbf{r}) \cdot d\mathbf{r} \cdot \exp(i \cdot \omega(\mathbf{r}) \cdot t) \\ &\text{where} \quad \omega(\mathbf{r}) = \gamma \cdot (B_0 + \mathbf{G} \cdot \mathbf{r}) \\ &S(t) = \iiint_{\text{all } \mathbf{r}} \rho(\mathbf{r}) \cdot \exp(i \cdot \mathbf{G} \cdot \mathbf{r} \cdot t) \cdot d\mathbf{r} \end{aligned} \qquad [1\text{-}6]$$

In [1-6], only the application of the gradients is considered the source of dephasing and the loss of coherence due to spin-spin interactions (i.e., T_2) is neglected. Since [1-6] has the form of a Fourier transform, one can introduce the quantity **k**, the reciprocal space vector expressed as (Twieg, 1983)

$$\mathbf{k} = \frac{\gamma \cdot \mathbf{G} \cdot t}{2\pi} \qquad [1\text{-}7]$$

k depends on the duration and amplitude of the gradient. Using **k**, [1-7] becomes

$$\begin{aligned} &S(\mathbf{k}) = \iiint_{\text{all } \mathbf{r}} \rho(\mathbf{r}) \cdot \exp(i \cdot 2\pi\mathbf{k} \cdot \mathbf{r}) \cdot d\mathbf{r} \qquad [1\text{-}8] \\ &\rho(\mathbf{r}) = \iiint_{\text{all } \mathbf{k}} S(\mathbf{k}) \cdot \exp(-i \cdot 2\pi\mathbf{k} \cdot \mathbf{r}) \cdot d\mathbf{k} \end{aligned}$$

These relationships demonstrate that the spin density $\rho(\mathbf{r})$ is obtained by a simple Fourier Transform of the signal S(t). K-space is a convenient tool to represent pulse sequences and the trajectory in k-space will be presented later for different sequences relevant to this work.

An important note should be made on data represented in k-space: one line of k-space data is acquired during frequency encoding. On the other hand, data points along the pseudo time direction (phase encoding) are acquired each time that the amplitude of the phase encoding gradient is changed, that is typically every TR. This fundamental difference between time and pseudo time has considerable influence on the type and propagation of artifacts, especially motion artifacts, across the image.

Conventional 2D spin-echo sequence

The timing diagram of the spin-echo (SE) pulse sequence and its k-space representation are shown on figure 1-2. The main advantage of this sequence is that it refocuses main magnetic field inhomogeneities and the images reflect T_2 and not T_2*values. This is especially important at high magnetic field strengths (3T and above) where inhomogeneities can induce severe distortions.

The k-space diagram shows that points from the same line of k-space are acquired every δt_x. Every TR, G_y is incremented and another line of k-space is acquired. For this reason, k_x and k_y are referred respectively as the time and pseudo-time dimensions.

When k-space data is acquired in Cartesian coordinates, the image is reconstructed by performing a 2-dimensional (2D) FT.

Multi-echo sequences

To speed up data acquisition, sequences that use multiple echoes in one TR have been developed. One of these sequences, the multi-echo (ME) sequence timing diagram and its k-space representation are presented on figure 1-3. Multiple echoes are created by applying successive 180° pulses. Each echo is acquired with an identical phase encoding. The number of echoes is called the echo train length (ETL) and the time between two successive echoes is called the echo spacing (ES). Each echo contributes to one of the multiple images from which T_2 calculations will be performed (see figure 1-3). In one TR, ETL echoes are acquired for each slice. Depending on the number of slices and the TR, up to 64 echoes (ETL: 2-128) are usually accommodated. The ETL represents the gain in acquisition time of an ME sequence compared to an SE sequence.

Rapid acquisition relaxation enhancement imaging

Another spin-echo sequence, the rapid acquisition relaxation enhancement (RARE) method, is presented in figure 1-4. The RARE sequence was introduced by Hennig et al. (Hennig *et al.*, 1986). Each echo is phase-encoded differently and contributes to one image. As observed on the pulse diagram, all echoes are acquired at a different echo time. The echo time at which data with minimal phase encoding is acquired characterizes the image contrast and is called TE effective (TE_{eff}). Similarly to the ME, the echo train length is the number of echoes collected in one TR (or the number of 180° pulses) and represents the acquisition time gain of a RARE versus a SE sequence. RARE is sometimes called fast spin-echo on clinical scanners.

Echo planar imaging

Techniques acquiring multiple lines of k-space in one TR were introduced by Mansfield (1984). These are currently possible with improvements in gradient hardware. The most famous is the known echo planar imaging (EPI). EPI uses rapid switching of gradients and requires special hardware with rise times as fast as 200 μs and amplitudes as high as 2 and 20 $G.cm^{-1}$ on a clinical and research systems respectively. With such a scheme, an image can be acquired within 100 ms in a "single shot" (i.e., in one TR). Figure 1-5 displays the EPI pulse sequence and k-space trajectory.

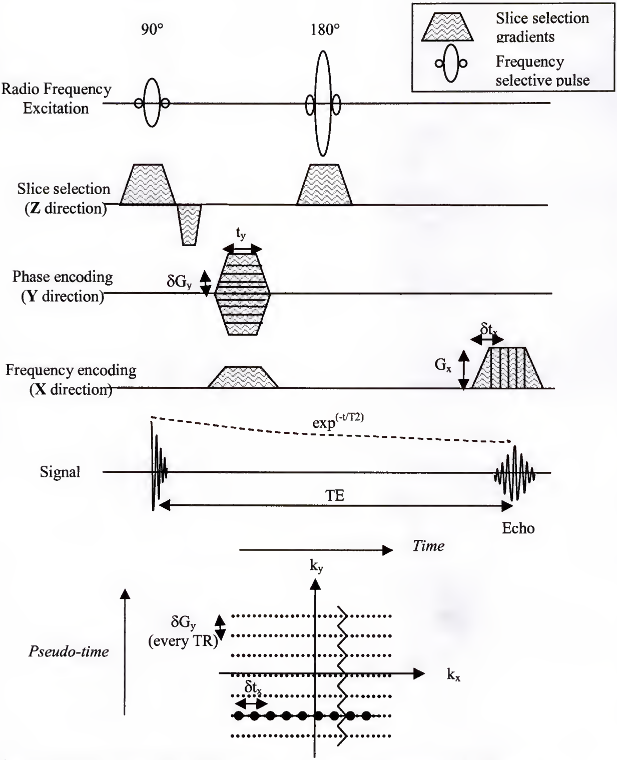

90°
180°
Slice selection gradients
Frequency selective pulse
Radio Frequency Excitation
Slice selection (Z direction)
t_y
Phase encoding (Y direction)
δG_y
δt_x
Frequency encoding (X direction)
G_x
$\exp^{(-t/T2)}$
Signal
TE
Echo
Time
k_y
δG_y (every TR)
Pseudo-time
k_x
δt_x

Figure 1-2: Timing diagram and k-space representation of a conventional spin-echo sequence.

A spin-echo is obtained by successive application of a 90° and a 180° radio-frequency pulses. The frequency-selective RF pulses together with the slice selection gradients excite spins in a defined **Z** plane. The phase encoding gradient codes the signal along the **Y** direction and the frequency along the **X**. This part of the sequence is repeated every repetition time. The free induction decay (FID) disappears rapidly and only the echo is collected.

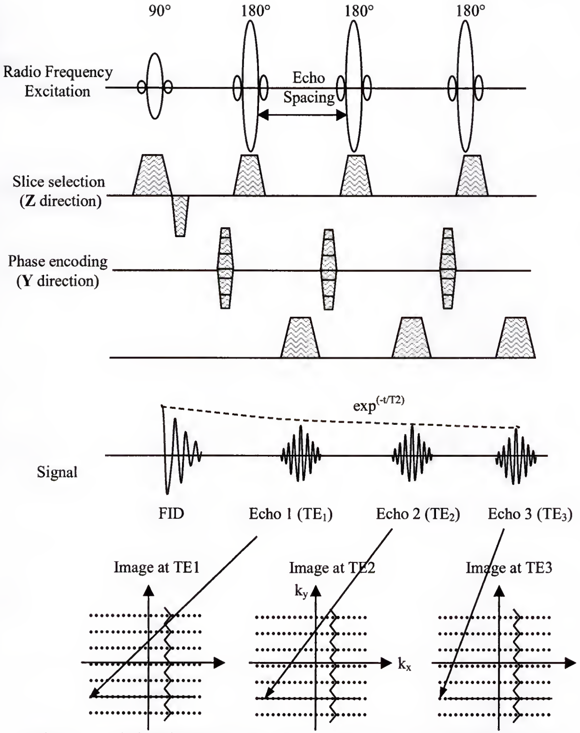

Figure 1-3: Timing diagram and k-space representation of the multi-echo sequence. Three echoes are refocused and each of them contributes to an individual image. Each image is collected at a different TE and therefore has a different amount of T_2 weighting.

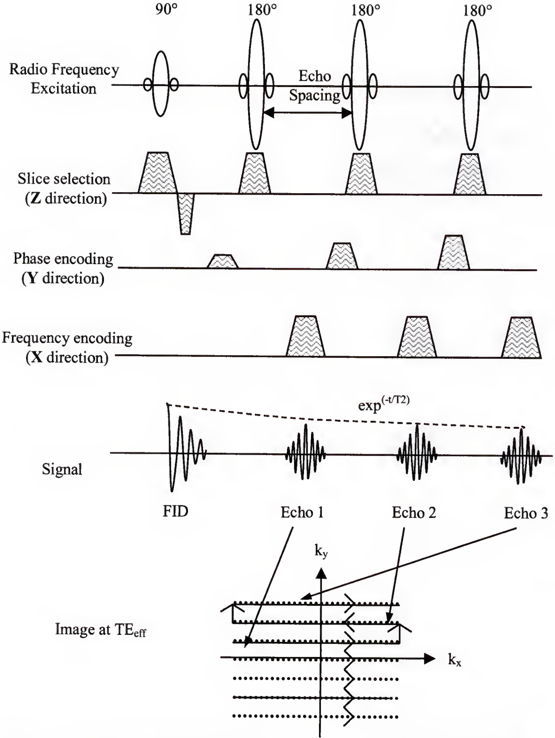
90°
180°
180°
180°
Radio Frequency Excitation
Echo Spacing
Slice selection (Z direction)
Phase encoding (Y direction)
Frequency encoding (X direction)
exp(-t/T2)
Signal
FID
Echo 1
Echo 2
Echo 3
Image at TEeff
ky
kx

Figure 1-4: Timing diagram and k-space representation of the RARE sequence. Similarly to the multi-echo sequence, RARE uses multiple echoes. However, these echoes are used to reconstruct only one image. This image is considered to be reconstructed at TE_{eff}, which is the echo time at which the center line of k-space was acquired.

Spiral imaging

A variation of EPI is spiral imaging where sinusoidal gradients are applied in the **X** and **Y** directions simultaneously. Because data points are not acquired in Cartesian coordinates, spiral imaging requires the use of a back-projection reconstruction algorithm.

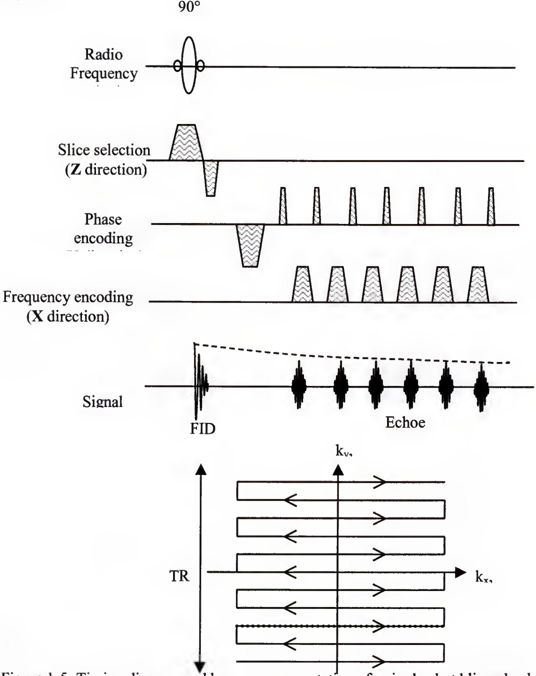
90°
Radio Frequency
Slice selection (Z direction)
Phase encoding
Frequency encoding (X direction)
Signal
FID
Echoe
k_y
TR
k_x

Figure 1-5: Timing diagram and k-space representation of a single-shot blipped-echo-planar imaging sequence.

Introduction to Functional Magnetic Resonance Imaging

Introduction

For a long time, knowledge about the brain was obtained from post-mortem examinations. Therefore, the gathered information dealt mainly with the anatomical structure. However, not only brain gross anatomy but also function is important to understand the basis of disease and disorders.

The term "functional brain imaging" refers to *in vivo* methods of brain activation image acquisition. These methods include electro-encephalography (EEG), magneto-encephalography (MEG), positron emission tomography (PET), and single photon computed tomography (SPECT), and the more recent functional MRI (fMRI). Before the advent of fMRI, PET and SPECT were predominantly used. These techniques rely on the use of radioactive tracers incorporated in the brain activation energetic cycle. During a neuronal event, gamma rays are emitted locally and an image of the pattern of activation can be collected.

At the beginning of the nineties, Ogawa *et al.* (1990, 1992) used the magnetic properties of oxygenated versus deoxygenated blood to investigate brain function. He labeled the image contrast obtained blood oxygenation level dependent (BOLD) contrast and his work started the era of functional MRI (fMRI).

Blood Oxygenation Dependent Imaging

The BOLD technique uses endogenous biological processes as the source of contrast. The contrast is based on the magnetic properties of hemoglobin which depend on its oxygenation state (Pauling, 1977). Oxygenated hemoglobin (oxyhemoglobin) is diamagnetic. It is carried in the blood and provides tissues with the necessary oxygen for normal brain function. Once the oxygen is delivered, the resulting deoxygenated hemoglobin molecule (deoxyhemoglobin) becomes paramagnetic. Upon brain activation, oxygen demand increases. In response, regional cerebral blood flow (CBF) increases and more oxy-hemoglobin is present in the tissue. Oxygen consumption increases but the overall relative amount of oxy- to deoxyhemoglobin (i.e., diamagnetic to paramagnetic molecules) increases. This causes a T_2* increase and therefore the signal in T_2* weighted images increases.

BOLD Contrast and Brain Activation

The characteristics of the BOLD signal are related to several physiological parameters: the CBF, presented earlier, but also the cerebral rate of oxygen consumption ($CMRO_2$), the cerebral blood volume (CBV), and vessel size. In addition, it is also dependent on measurement parameters such as pulse sequence, echo time and field strength. Despite several years of research, the BOLD signal exhibits a large intra- and inter-subject variability and its biological origins are still not well understood.

However, it is believed that the time-course of the signal can be decomposed in three phases. At 1 to 2 s after the onset of the stimulus, a small signal decrease of about 1% is detected. This "early response" is associated with a phenomenon observed using intrinsic optical imaging: as CBF is still at its resting level and the $CMRO_2$ consumption increases, the relative amount of deoxyhemoglobin increases. Within a variable hemodynamic delay of 4 to 8 s, local blood flow increases bringing an excess of oxy-hemoglobin, that is not used by the brain. At this time and during the rest of the stimulation period, the signal exhibits a "steady state" signal increase of 1 to 10%, (depending on the field strength and the stimulation type). The observed signal reflects the combined effects of increased CBV, $CMRO_2$, and predominantly CBF. Upon cessation of the stimulation, the BOLD signal does not directly return to baseline but displays a 1 to 5% "undershoot" that lasts 10 to 25 s. The mechanism of the undershoot is attributed to the influence of the CBV, which is delayed compared to CBF when returning to its baseline level. Figure 1-6 summarizes the influence of CBF, CBV and $CMRO_2$ on the time course of the BOLD signal upon activation.

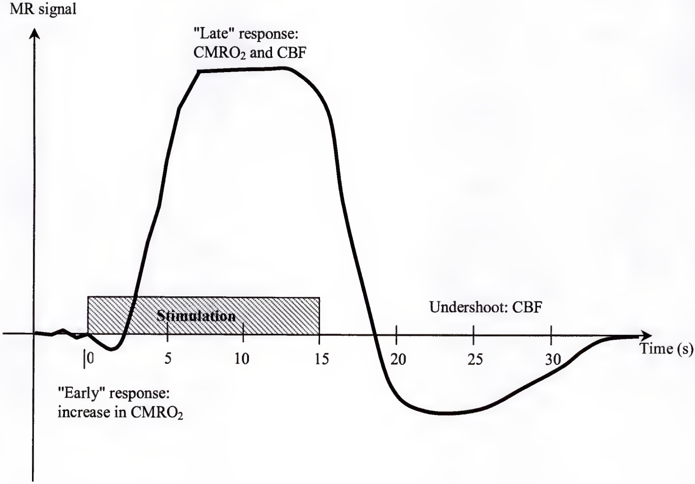

Figure 1-6: Time course of the blood oxygenation level dependent MR signal.
Upon the presentation stimulation, the BOLD signal exhibits a small decrease of 0.5 to 1% which is attributed to the increased in CMRO2. Six to 8 s later, the CBF increases and the signal reaches its maximum of 2 to 10%. Upon cessation of the stimulation, the signal takes approximately 20 s to return to baseline.

Functional Magnetic Resonance Imaging Experiments

During a fMRI experiment, the brain is imaged into two states, generally performing a task and at rest. To acquire a dynamic time series of images, fast acquisition technique such as fast low angle snapshot imaging (FLASH) (Haase *et al.*, 1989; Haase, 1990), spiral or EP imaging are used. Because of signal to noise ratio (SNR) constraints, functional images are generally low resolution (typically 5 x 2 x 2 mm^3).

The difference in image intensity enables the localization of active brain tissue. Because the signal change is quite small and the scanner not stable, difference images are unreliable in detecting activation and a more advanced processing strategy needs to be adopted. One of these strategies was introduced by Bandettini *et al* (1993). A task is performed in a repetitive manner, for example for 3 cycles composed of 30 s during which the subject has to perform a task and 30 s during which the subject is at rest. A time series of the data is acquired during this "block design" stimulation and each pixel time course is cross-correlated with the reference waveform depicting stimulus presentation. More recently fMRI stimulation protocols are based on stimulation of the brain during one neuronal event: this is called "single event" fMRI. In both cases of block design and single event studies, extensive post-processing manipulations are required to ensure reliable localization of activation.

One critical step in all the fMRI approaches is that the subject stays still in the magnet so that the MR signal in the same pixel can be investigated over time. This is performed by immobilizing the patient head with foams and/or bite bars. In addition, visual inspection for motion artifact and image registration are done prior to any further analysis. The next steps include defining a strategy and obtaining a statistical map that represents the probability of an area being active during the task.

In addition to the sequence used for functional image acquisition, high-resolution MR images are collected and the activation map is superimposed on top of these. Finally, angiograms are obtained to identify the location of large vessels.

Principles of T_2 Mapping

Introduction

Since T_2-weighted images have been successful in differentiating normal tissue from pathology, there has been considerable interest in mapping the water spin-spin relaxation time, T_2. T_2 mapping has generally been a poor diagnostic indicator (Bottomley *et al.*, 1987), mainly due to the lack of standardized and accurate method of data acquisition. However, it has already proven to be a successful pathological index for late onset examinations of ischemic brain injuries (Horikawa *et al.*, 1986; Barnes *et al.*, 1986; Ebisu *et al.*, 1993; Rumpel *et al.*, 1995; Fu *et al.*, 1990) and shows promise in the evaluation of other disorders or diseases.

Mapping Principles

The maximum amplitude of the NMR signal in a spin-echo sequence decays exponentially as a function of the echo time TE. This decay is governed by the transverse relaxation time T_2. Therefore, images at different echo times are acquired. Then, for each pixel, the signals at the various TEs are fitted to a mono-exponential decay scheme and T_2 values can be extracted. T_2 values are finally represented on a pixel-by-pixel basis and coded on a gray scale to form a T_2 map.

Typically, all parameters except TE are kept identical during data acquisition. Long TRs are selected so that differential T_1 attenuation effects do not occur. Using this approach, T_2 can be calculated from two spin-echo image signal intensities $S(TE_1)$ and $S(TE_2)$ acquired at TE_1 and TE_2:

$$T_2 = (TE_2 - TE_1) \cdot \ln\left(\frac{S(TE_1)}{S(TE_2)}\right) \qquad [1\text{-}9]$$

Although it is possible to calculate T_2 values from only two echo times, estimates based on two data points are susceptible to large errors. Typically, at least four echo times are acquired to reduce the error that arises from fitting the data. The necessity for data acquisition at several TEs can be prohibitively time-consuming. Therefore rapid but accurate imaging schemes have been investigated.

Mono- and Biexponential Models

When a sample is homogeneous, it is characterized by one T_2 and the MR signal decays exponentially as a function of echo time. However, *in vivo*, a pixel contains water molecules with different relaxation properties, "bound" and "free" NMR visible water. Bound water corresponds to water molecules that interact with macromolecules, such as proteins and lipids. NMR visible "bound" water has a short T_2, for example less than 10 ms for water in myelin. Free water has a longer T_2 of ~ 900 ms, which is about 1/3 of T_2 of pure water. A further complication is introduced by the fact that molecules in bound and free water compartments are in exchange. Figure 1-7 represents a schematic T_2 representation of biological tissue.

The contribution of the bound water fraction dominates the observed T_2 in both intracellular and extracellular space (ICS and ECS) (Hsu *et al.*, 1996). It is postulated that, since the bound water fraction is higher in the "crowded" ICS than in the ECS, the observed intracellular T_2 might be in the range of 30 ms (Shoeniger *et al.,* 1994), shorter than the extracellular T_2, which is in the range of 80 ms. In the macroscopic NMR voxel, the measured T_2 is an average of the intra- and extracellular T_2. However, in certain cases such as voxels containing myelin or cerebrospinal fluid (CSF) (characterized by a short or very long T_2 respectively), then the MR signal is a superposition of the longer and shorter T_2 populations weighed by their respective fractions (w and (1-w)).

$$S = S_0 \cdot \left(w \cdot \exp - \left(\frac{TE}{T_{2long}}\right) + (1-w) \cdot \exp - \left(\frac{TE}{T_{2short}}\right)\right) \qquad [1\text{-}10]$$

Figure 1-8 shows how this type of compartmentation causes a deviation from a mono- to a biexponential decay. As pointed out, the signal is dominated by the bound water fraction and biexponential behavior can only be observed when data at long echo times are acquired.

Considerations on the Use of Multiple Echoes Sequences

To obtain T_2 maps, it is necessary to acquire images at multiple echo times. As presented earlier, multiple echo sequences allow collecting images faster than spin-echo sequences. However, this gain in time has to be weighed against the drawbacks of employing sequences with multiple pulses.

When multiple pulses are applied successively, imperfections in 180° RF pulses can greatly affect the image quality and consequently the estimation of T_2 (Majumdar *et al.*, 1986; Poon & Henkelman, 1992). These imperfections lead to signal loss through the creation of stimulated echoes (figure 1-9). These echoes show as an image artifact (i.e., ghost) and introduce some T_1 dependence in the amplitude of the echo (Williams *et al.*, 1996), which in turn leads to an underestimation of T_2 values. In practice, imaging gradients dephase the signal and the gradients are reversed to "rewind" the NMR signal phase before the application of the refocusing pulses.

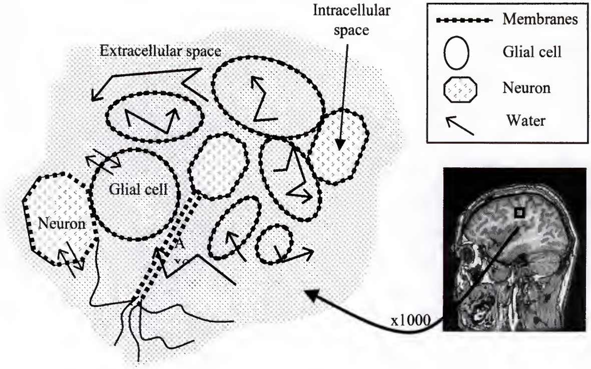

Figure 1-7: Representation of water molecules in an in vivo sample.
Water molecules are bound or free. The bound water fraction tends to be located in the ICS where there are many macromolecules. The free water fraction is found in the ECS. Both compartments are in exchange as water travels from one to the other.

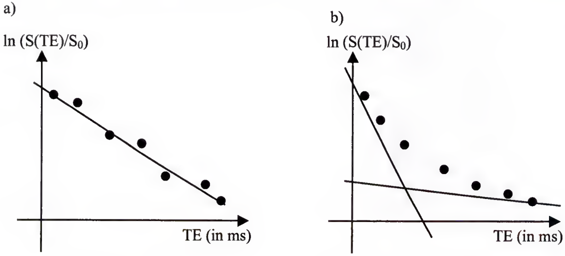

$$S(TE) = S_0 \cdot e^{-TE/T_2}$$

$$S(TE) = S_0 \cdot \left(w \cdot e^{-TE/T_{2long}} + (1-w) \cdot e^{-TE/T_{2short}} \right)$$

Figure 1-8: a) Monoexponential and b) biexponential decay curves.

The stimulated echoes are encoded similarly to the spin echoes and both signals are combined. This method reduces the ghost artifact but introduces the previously mentioned T_1 dependence that can lead to inaccurate T_2 estimates. The mechanism of the creation of a stimulated echo is shown on figure 1-9. The diagram shows how a combination of three 90° pulses creates a stimulated echo. The mixing time TM, introduces a T_1 dependence in the amplitude of the echo. However, any combination of three imperfect 180° pulses results in a creation of the stimulated echo.

Phase rewinding is typically incorporated in multiple-pulse sequences available on clinical scanners. An alternative to phase-rewinding employs balanced spoiler gradients (Poon, & Henkelman, 1992; Majumdar & Gore, 1987). These gradients are placed symmetrically on each side of all refocusing pulses and their amplitude is optimized to provide efficient suppression of stimulated echoes. In addition to the creation of stimulation echoes, the contrast in multi-echo sequences is influenced by several factors not observed in the CSE sequence (see reviews by Constable *et al.* (1992) and by Williams *et al.* (1996)). These factors include magnetization transfer effects, diffusion effects, J-coupling, and differential attenuation due to the acquisition of the data at different TEs in the case of the FSE sequence.

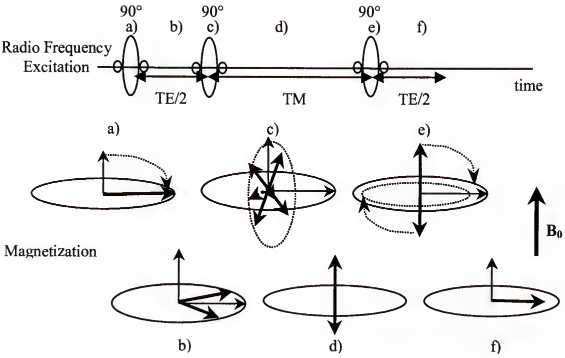

Figure 1-9: Mechanisms of the stimulated echo.

Principles of Diffusion Mapping

Diffusion Processes in Biological Tissues

Diffusion is the translational molecular motion caused by Brownian motion as well as biological processes. Brownian motion is due to thermal fluctuations, which cause random molecular collisions. Biological processes include any exchange of water protons such as diffusion across membranes for osmotic regulation. Diffusion can occur at different rates in several "compartments" such as blood vessels, intracellular and extracellular spaces. In the ICS, protons encounter many boundaries and therefore the diffusion coefficient is lower than in the ECS where protons move more freely. As a pixel contains many types of tissue, and DW images are sensitized to diffusion in only one direction, the diffusion measurement represents an averaged value of diffusion of water molecules. For this reason, it is called the apparent diffusion coefficient (ADC).

As stated above, the term diffusion combines both an intra and extravascular component. Although the intravascular water is only ~ 2% to 5% of the total brain water, diffusion-weighted (DW) images are influenced by both intra- and extravascular signal. The study of the pure intravascular diffusion signal is called perfusion imaging and will not be discussed.

Apparent Diffusion Coefficient Mapping Sequence and Parameters

Figure 1-11 represents a schematic diagram of a diffusion spin-echo sequence, which was initially introduced by Stejskal and Tanner (1965). Parameters that characterize the sequence are the duration δ, the amplitude G and the time Δ between the onset of the diffusion gradients. For stationary protons, the dephasing due to the first diffusion gradient is compensated by application of the second gradient. On the other hand, after application of the second diffusing gradient, diffusing spins exhibit a residual dephasing. The signal attenuation in DW images has been shown to take the following form (Stejskal & Tanner, 1965):

$$\begin{aligned} &S(b) = S_0 \cdot e^{-b \cdot ADC} \\ &\text{where } b = \gamma^2 \cdot G^2 \cdot \delta^2 \cdot \left(\Delta - \frac{\delta}{3}\right) \end{aligned} \qquad [1\text{-}11]$$

The ADC is the Apparent Diffusion Coefficient in units of $mm^2.s^{-1}$ and represents the average surface per unit time that a group of diffusing water molecules would cross (see figure 1-12). It should be noted that ADC is a diffusion value obtained by sensitizing the measurements to a particular orientation and is highly dependent on that direction in anisotropic media. The b-value (in $s.mm^{-2}$) characterizes the amount of diffusion weighting and is dependent on the duration δ, amplitude G and Δ, the relative timing of the gradients. From these parameters, the diffusion time τ can be calculated:

$$\tau=\Delta-\delta/3 \qquad [1\text{-}12]$$

If G, Δ or δ is increased, the dephasing is also increased and the sequence is made more sensitive to water motion. Therefore, a larger b-value characterizes a greater sensitivity to diffusion.

Limits of the Monoexponential Model

Equation [1-11] represents the ideal case where the signal is acquired from a homogeneous tissue sample. However, as introduced earlier, water molecules in biological tissues belong to several compartments, which are in exchange and this heterogeneity shows up as deviation from equation [1-11] at b-values above 2000 $s.mm^{-2}$.

Influence of the characteristic exchange time constant between intra- and extracellular compartments

If the diffusion time is long compared to the characteristic time constant of exchange between slow and fast diffusing compartments, then water is fully exchanged between the two and the observed ADC is a weighted average of the ADCs. In this case, the signal is given by the following equation

$$S = S_0 \cdot \exp\left(-b \cdot \left(w \cdot ADC_{fast} + (1-w) \cdot ADC_{slow}\right)\right) \qquad [1\text{-}13]$$

If diffusion in the tissue is observed over a time scale much shorter than the exchange rate, then the signal S is a superposition of fast and slow-diffusing compartment signals:

$$S = S_0 \cdot \left(w \cdot \exp(-b \cdot ADC_{fast}) + (1-w) \cdot \exp(-b \cdot ADC_{slow})\right) \qquad [1\text{-}14]$$

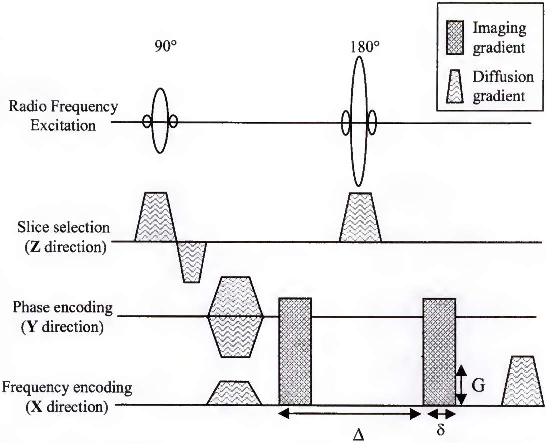
90°
180°
Imaging gradient
Diffusion gradient
Radio Frequency Excitation
Slice selection (**Z** direction)
Phase encoding (**Y** direction)
Frequency encoding (**X** direction)
G
Δ
δ

Figure 1-10: Timing diagram of the spin-echo diffusion sequence introduced by Steksjal and Tanner (Stejskal & Tanner, 1965).
A standard spin echo sequence is combined with two diffusion gradients of equal amplitude G and duration δ applied symmetrically before and after the 180° pulse. The onset of the gradients is separated by a duration Δ. The measurement is sensitized to diffusion along the **X** (or frequency encoding) direction.

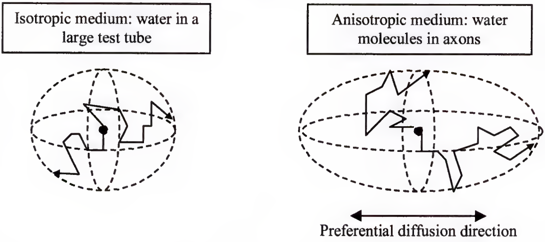
Isotropic medium: water in a large test tube
Anisotropic medium: water molecules in axons
Preferential diffusion direction

Figure 1-11: Schematic representation of isotropic and anisotropic diffusion
Water molecules are initially located at a center point and are allowed to diffuse. An example path and the net diffusion surface is represented (adapted from Neil (1997)).

Therefore, if the sample is characterized by two compartments with different ADCs, the data should be fitted to a biexponential model (Szafer *et al.*, 1995; Niendorf *et al.*, 1996; Buckley *et al.,* 1998). Using the biexponential model, signal attenuation at low b-values is influenced by both fast and slow diffusing components. At large b-values (above 4000 s.mm^{-2}), the signal is dominated by the slow diffusing water molecules fraction. The biexponential model has been successful in explaining the dramatic ADC drop in acute ischemia (Moseley *et al.*, 1990). In fact, during ischemia, edema occurs and water redistributes itself between intra- and extracellular compartments. However, there are no changes in the ADC of each compartment (Hsu *et al.*, 1997).

In addition to compartmentation, other factors such as membrane permeability, temperature and tortuosity in the ECS influence the ADC.

Membrane permeability

The permeability P is the ratio of the diffusion coefficient through a membrane to its total surface area. If the slow and fast diffusing compartments are assigned to intra- and extracellular compartments, membrane permeability P affects the fraction of slow and fast protons. However, P has not been shown to contribute significantly to diffusion coefficient changes relative to the other factors presented here.

Temperature

Temperature affects greatly diffusion measurements. Le Bihan *et al* (1989) showed that a change of 1°C induces a 2.4% reduction in the ADC. This factor is not negligible since in ischemia, the reduction in blood flow induces reduction in temperature. Although local changes in temperature contribute to variations in the ADC, the effect is usually not pronounced enough to account for the bulk of the variations (Moseley *et al.*, 1990; Benveniste *et al.*, 1992; Ebisu *et al.*, 1993).

Increased tortuosity in extracellular space

Tortuosity is a measure of the changes in direction of molecules being reflected against boundaries. Although this concept is defined for molecules, which stay exclusively, in the ECS and for the water that enters the cell, water tortuosity is used to explain part of the changes in ADC, such as those occurring during cell swelling or also called cytotoxic edema. Cytotoxic edema triggers an increase in cell volume and a parallel reduction in ECS. As cells swell, this decrease causes extracellular water to encounter boundaries more often, resulting in an increased tortuosity. Effectively, this is equivalent to restricting diffusion in the ECS (i.e., reducing ADC_{fast}) (Norris *et al.*, 1995).

Protocol Selection for ADC Mapping

Time- versus amplitude-constant diffusion measurements

The importance of the time scale of water exchange in biological systems leads to the concept of time-dependent or amplitude-dependent experiments. In the time-dependent experiment, Δ, δ or τ are varied while the amplitude G of the gradient is kept constant. In such experiments, at short Δ, equation [1-11] describes the system. If there is a barrier in one dimension, the ADC drops. At larger t, the signal reaches an asymptotic value dictated by the permeability of the membranes (Szafer *et al.*, 1995). If the system is not restricted, the ADC does not depend on Δ. In the amplitude-dependent experiment, gradient timing is kept constant and G is varied. This is the most common approach as it allows keeping TE and therefore T_2 relaxation effects constant. In this method, the diffusion time τ determines the regime, fast or slow exchange, under which the measurements are obtained.

Types of diffusion measurement

As some components of the brain such as sheaths of myelin are clearly anisotropic, diffusion is only fully represented by a tensor D: each element of the tensor indicates the ADC along one direction. Diffusion tensor imaging (DTI) (Pierpaoli *et al.*, 1996) requires the application of diffusion gradients in at least six gradient axes. If axial symmetry is assumed, then measurements in four diffusion directions at different b-values are needed. Although DTI is the most complete method of obtaining diffusion information, data acquisition is time consuming. Consequently, alternative methods have been proposed. A directionally averaged ADC, the trace of D, or tr(ADC), can be measured through the application of diffusion gradients along only three orthogonal directions. tr(D) is a convenient measurement as it is rotationally invariant, i.e., its value is independent of the orientation of the sample in the magnet. From measurements along two orthogonal orientations, the fractional anisotropy can also be reported. Fractional anisotropy is the ratio of the ADC along one direction to the ADC along another perpendicular direction. A fractional anisotropy coefficient close to 1 indicates that diffusion properties of the sample are similar in the two directions. If it differs greatly from 1, then the tissue is anisotropic due to the presence of oriented structures such as axons or fiber tracts.

The mechanisms causing changes in the ADC are not fully understood. Nevertheless, diffusion-weighted (DW) imaging has proven effective in the diagnosis of stroke and trauma, as well as monitoring normal brain maturation.

Conclusion

Several approaches allow obtaining quantitative MRI measurements. With a well-designed acquisition and post-processing protocol, MRI can be a reliable method for the study of brain function and to obtain indications of the tissue microstructure.

In this work, new methods to study brain functionality in both the human and the rat will be presented. The emphasis of this dissertation will be placed on the optimization of the imaging protocol and the post-processing techniques in order to extract reliable quantitative MR data.

First, chapter 2 will demonstrate the feasibility of functional MRI using auditory stimulation. This new method will be applied to investigate the dependence of the MRI signal on speech intensity in humans. Chapters 3 to 5 will discuss the development and optimization of a quantitative imaging protocol applied to brain maturation and monitoring of shunting in neonatal hydrocephalic rats. Chapter 3 will present monoexponential T_2 and diffusion measurements obtained at 3 post-natal ages. Chapter 4 will present similar measurements following shunt-treatment, sham-operation and fluid-deprivation from 8 until 21-days-old rats. Finally, chapter 5 will introduce a new approach using biexponential fitting models to investigate diffusion and T_2 properties of the tissue during maturation of normal and hydrocephalic rat brain. Finally, chapter 6 will summarize the contribution of this work to the field of MRI and present directions for future studies. Appendix C lists the scientific publications stemming out this work.

CHAPTER 2
INLUENCE OF SPEECH INTENSITY ON THE ACTIVATION OF THE AUDITORY CORTEX DETECTED BY MRI

Introduction

As introduced in Chapter 1, brain activity is characterized by local changes in physiological parameters such as regional cerebral glucose metabolism (rCMRgl), oxygen consumption (rCMRO$_2$), cerebral blood flow (rCBF) and cerebral blood volume (rCBV). These changes affect the signal in Magnetic Resonance (MR) images (Ogawa *et al.*, 1993; DeYoe *et al.*, 1994; Buxton *et al.*, 1998) and neuronal activation can be detected on T$_2$*-W MR images. These discoveries have lead to the development of a non-invasive neuroimaging tool called functional Magnetic Resonance Imaging (fMRI). In this chapter, a study of auditory fMRI will be presented. Particular emphasis will be put on the advanced processing strategies needed to obtain reliable measurements (Mohr *et al.*, 1999).

Although there have been many fMRI studies of oral language and auditory processing, the effects of simple auditory stimulus manipulations such as intensity, frequency and rate have been largely ignored. In view that the origins of the fMRI signal change are poorly understood, it seems important to characterize the influence of auditory stimulus presentation if it is to be used for cognitive and language experiments. Of the few studies which have addressed basic stimulus parameter issues, several have investigated the influence of presentation rate on the fMRI response (Binder *et al.*, 1994;

Dhankhar *et al.*, 1997). Increase in stimulus presentation rate had been shown to increase rCBF using Positron Emission Tomography (PET) (Price *et al.,* 1992). When this parameter was varied in a fMRI experiment, the percent signal change of activated areas increased with increasing rate (Binder *et al.*, 1994). Similarly, sound intensity was shown to increase rCMRgl in central auditory structures in animals (Abrams *et al.*, 1989). Nevertheless, the dependence of the fMRI signal on stimulus intensity has not been described except for two studies by Millen and Strainer (Millen *et al.*, 1995; Strainer *et al.*, 1997). Both studies used two levels of sound intensity and a limited number of subjects (n=8 and n=10 respectively). Millen *et al.* found no influence of speech intensity on the volume of fMRI activation (i.e., the number of voxels satisfying the statistically significant activation criteria). Strainer *et al.* presented pure tone stimuli and showed an increased volume of activation at higher sound intensity when imaging the primary auditory cortex.

In this study, to address the issue of optimal stimulus presentation in language studies, intensity was varied and intelligibility (i.e. the understanding of the words) was monitored during the experiment to assess its effect on the fMRI response. Speech stimuli were presented at five Intensity Levels (IL) to 18 subject. A reliable measure of activation volume was defined and right versus left hemisphere differences were investigated. In addition, the relative percent signal change was measured at each IL to establish the influence of the stimulation manipulation on the fMRI signal change. Finally, reproducibility of the activation was measured for one subject and the influence of IL on the percent signal change in fMRI data was assessed.

Materials and Methods

Subjects

Eighteen volunteers (17 males- 1 female; 21-40 years old) participated in a one-hour scanning session. Handedness was assessed in 16 of the 18 subjects with the Edinburgh handedness inventory (Briggs & Nebes, 1975). Eight of these subjects were classified as dextral and eight as adextral (scores < 0.75). Participants were recruited on a voluntary basis and signed an informed consent form that had been approved by the University of Florida Institutional Review Board.

Selection of Stimuli and Sound Delivery Set-up

The speech stimuli used in this experiment were monosyllabic English words taken from the Northwestern University word lists (NU-6) (Abrams *et al.*, 1989). The NU-6 lists were chosen because they contain a large number of words (200), have high inter-test reliability and are in widespread clinical use as a measure of word discrimination ability. The word lists were digitally filtered with a finite impulse response function to ensure spectral stability and then recorded on magnetic tape for playback to the subjects. The rate of presentation was kept constant at 30 words per minute.

Auditory stimuli were delivered binaurally through a sound delivery system built by Dr. Wayne King. The audio system consisted of an amplifier coupled to a 6 m-length of 1.2 cm-diameter rigid plastic tubing. A 0.6 cm thick foam insulated the tube from sound impinging on its outside. At the chest of the subject the tube split into 2 smaller 0.2 cm- diameter tubes, which ended in tightly occluding foam inserts for the ears. A vent was placed at the tubing fork to attenuate low frequencies, which dominate an acoustic stimulus at the distal end of a tube. The subjects were also fitted with protective headphones (average noise reduction rating: 20 dB) to provide additional attenuation of scanner noise. Figure 2-1 illustrates the experimental set-up. The output of the sound delivery system was verified by measuring the output of the inserts in a 2 cm^3 coupler and verified on one volunteer by placing a probe-tube microphone in the ear canal approximately 5 mm away from the tympanic membrane. All sound levels were measured on a C-weighted scale and ranged from 65 to 110 dB.

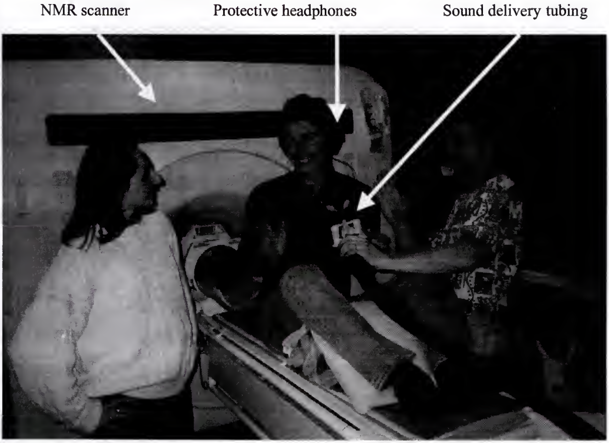

Figure 2-1: Auditory fMRI setup.

Selection of Intensity Levels and Experimental fMRI Design

Prior to the experiment, the stimulus intensities were individually determined to cover a range from low to perfect intelligibility for each subject. The subject listened to the tape while a dummy scan replicated the true fMRI experiment noise conditions.

Initially, the tape was played at 70 dB and 100 dB (C-weighted scale). The subject was instructed to repeat out loud the word he or she heard. The answers were recorded by an observer who calculated the percentage of correctly identified versus total number of words presented. Three additional sound levels were then chosen so as to cover a range of subject performance from poor (0 to 20% correct) to perfect (100% correct). The sound levels used for individual subjects ranged on a C-weighted scale from 65 to 70 dB at IL 1, 70 to 80 dB at IL 2, 80 to 90 dB at IL 3, 90 to 95 dB at IL 4 and 100 dB to 110 dB at the fifth IL.

In experiment 1, the five individualized intensity levels (IL) were then presented in a randomized order for each of the 18 subjects. To evaluate intrasubject variability of fMRI signal (i.e. reproducibility within a subject in the absence of intensity changes) a second experiment was conducted with 1 individual, in which the stimulus was presented five times at a constant IL (90 dB on a C-weighted scale) (experiment 2).

Each of the five functional trials lasted 4 min, alternating 30 s of stimulus on and off. During functional scanning, subjects were instructed to mentally rehearse the words and to lie still. Additionally, to measure intelligibility (i.e., the ability to understand the significance of speech as opposed to the volume or loudness of any) and to ensure the subjects' attention, they were instructed to indicate with a push button whenever they heard one of two target words. The target words were the same for all subjects and each of them occurred four times during the 2 min of stimulus presentation. Subject response was monitored to evaluate the true positive fraction (i.e. fraction of target words accurately detected to the total of target words) and false positive fraction (i.e. fraction of non-target words detected to the total number or words).

Imaging Protocol

All subjects were imaged on a 1.5T GE Signa scanner (General Electric Medical Systems, Milwaukee, WI) using the standard GE birdcage head coil. To restrict motion, subjects' heads were stabilized with foam padding. Functional images were acquired using a multislice spiral scan (Noll *et al.* 1995) technique (TR/TE/FA = 750 ms/40 ms/45°, 4 interleaves, 128x128 matrix, voxel size = 1.4 x 1.4 x 5 mm^3, 1.5 mm gap) resulting in a temporal resolution of 3 s. Five oblique slices covering Heschl's gyrus (HG), the planum temporale (PT) and the posterior superior temporal sulcus (STS) were selected from a sagittal view in the left hemisphere (figure 2-2 top left hand corner). For each functional trial, this acquisition protocol yielded 80 time-point images at each slice location. High-resolution anatomical images were obtained using a 3D-SPGR sequence (TR/TE/FA = 27 ms/7 ms/45°, 256x256x128 , voxel size = 0.94 x 0.94 x 1.3 mm^3).

Data Processing

Functional images were reconstructed and corrected for in-plane motion by aligning them to the last image of the functional run using the AFNI package (Medical College of Wisconsin, USA) (Cox, 1996). The AFNI package is a software containing a set of tools for display and analysis of functional activation data.

Using AFNI, each voxel signal intensity time course was correlated to a square reference waveform phase shifted by 6 s to create a map of correlation coefficients. The phase shift simulated an average delay in activation after stimulus onset, caused by the hemodynamic response time of the brain (Belliveau *et al.*, 1992; DeYoe *et al.*, 1994; Kim *et al.*, 1997). Voxel percent signal change ΔS between on and off periods were also calculated.

Correlation coefficients and percent signal change (ΔS) maps were overlaid onto the anatomic 3D data set, transformed to the standardized Talairach coordinates (Talairach *et al.*, 1967) and interpolated to 3x3x3 mm^3 (or 27 μl) voxels using AFNI (Cox, 1996). Voxels were defined as active when their correlation coefficient was greater than 0.5. This threshold ensured that the response of the voxel was related to the stimulus with a statistical significance of $p<0.001$ (Bandettini *et al.*, 1993).

Additionally, voxels with a ΔS greater than 20% were eliminated to exclude voxels representing large blood vessels and voxels at the edge of the brain where slight motion can create large signal changes. Using the 3-dimensional visualization tools of AFNI, three different regions of auditory cortex, HG (which contains primary auditory cortex), and secondary auditory cortex which includes PT and the STS, were identified on a sagittal view. The number of subjects with activation in these areas was recorded.

Additionally, two large regions of interest (ROI) that encompassed left and right primary and association auditory cortices were selected. Each ROI extended laterally beginning at 30 mm lateral to the midline, and ranged in the anterior/posterior direction from 10 mm anterior to the anterior commissure (AC) (Penhune *et al.*, 1996; Leonard *et al.*, 1998) to the occipital pole. This region of interest is illustrated on the 5 functional slices on figures 2-2a to 2-2e.

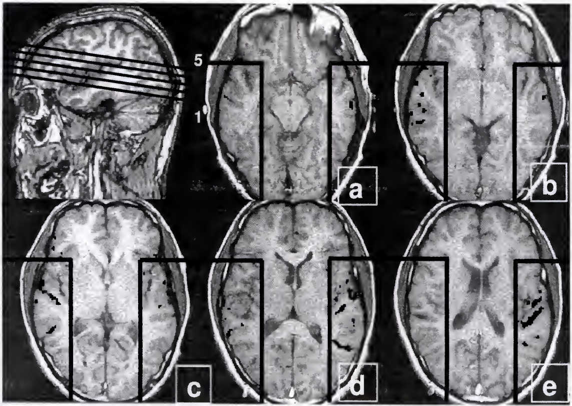

Figure 2-2: Localization of the 5 functional slices and a typical pattern of activation overlaid on top of anatomical gray scale images.
The two large regions of interest used for data analysis are indicated. Activation is represented by the overlaid dark pixels.

Data Analysis

Using data from experiment 1, the total volume of activation in this region and the mean percent signal change in that area (V_i and ΔS_i; $i = 1 - 5$) was measured as well as V_{3rep}, V_{4rep}, V_{5rep}, the volume of brain tissue activated at least 3, 4 or 5 times of the 5 presented IL. Two methods were adopted to analyze these data.

First, voxels activated at 3 or more stimulus intensity levels were combined and analyzed as "repeated voxels". Their percent signal change, ΔS_{3rep}, was calculated at each IL and their Talairach coordinates were recorded. To assess the influence of stimulus intensity on the signal change ΔS_{3rep}, the highest and the lowest stimulus IL

(IL_{max} and IL_{min}) at which each voxel was activated were identified. The change in response ΔR was calculated by subtracting the ΔS at the lowest stimulus intensity (ΔS_{3rep} @ IL_{min}) from that at the highest stimulus intensity (ΔS_{3rep} @ IL_{max}). Positive ΔR indicates an increase in percent signal change between lowest and highest stimulus intensity, while negative ΔR indicates a decrease in percent signal change as stimulus intensity increased. The hypothesis that ΔR was significantly different from zero was tested using a paired-sample t-test. Secondly, voxels activated at all 5 presentations of the stimulus were counted (V_{5rep}). Then, influence of intensity on their percent signal change, ΔS_{5rep}, was investigated using a 5-factor repeated measures ANOVA.

Using data from experiment 2, activated voxels at each of the 5 trials (v_i where i=1-5) and voxels activated in all the trials (V_{5rep}) were counted. The ratio of V_{5rep} to V_i was calculated for each trial as a measure of the intrasubject stability of the fMRI volume of activation. In addition $\Delta S_{5rep,i}$, the percent signal change at each trial i, of V_{5rep} was measured and compared to assess its stability.

Results

Intensity Level and Intelligibility

Figure 2-3 displays the mean true positive fraction (TPF) versus the mean false positive fraction (FPF) obtained at each intensity level during the fMRI experiments. Intelligibility is characterized by a high TPF and a low FPF. Performance became progressively better in going from IL 1 to IL 2 and IL 3, as reflected by decreased FPF and increased TPF. Two subjects performed worse at IL 4 than at IL 3, and the remaining increased their performance. Four did worse at IL 5 than at IL 4, while all others performed equally well. On the average, intelligibility increased from IL 1 to IL 4 and then slightly decreased at IL 5.

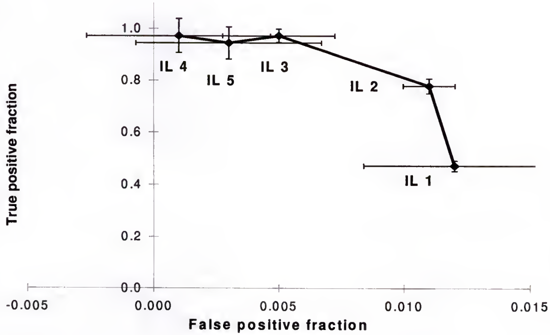

Figure 2-3: Subject response curve to the detection task at the 5 different intensity levels.

Reproducibility

Table 2-1 shows results of experiment 2 when stimulus intensity was not varied but kept at a constant level (90 dB-C, or the average IL 4). The volume of activation V_i at each trial i, the ratio (V_{5rep} / V_i) as well as the percent signal change of 5 times repeated voxels (ΔS_{5rep}) are presented. V_i can quadruple from one trial to another (range: 1701 μl to 7992 μl; mean: 4185 μl; standard deviation: 2538 μl or coefficient of variation (COV) 61%). The 594 μl activated in all the trials (V_{5rep}), represented only 7% of the largest total activation (in trial 2), to about 33% of the smallest activation volume (in trials 1 and 5). Despite this variability, visual inspection showed that the locus of activation was similar for each trial. The average ΔS_{5rep} ranged from 3.8% to 5.3%. The mean ΔS_{5rep} over the 5 trials was 4.4% (standard deviation: 0.6% or COV 13.4%).

Table 2-1: Reproducibility of activation.

	Trial 1 ***i=1***	***Trial 2*** ***i=2***	***Trial 3*** ***i=3***	***Trial 4*** ***i=4***	***Trial 5*** ***i=5***
V_i (in μl)	1917	7992	4590	4725	1701
V_{5rep}/V_i	0.31	0.07	0.13	0.13	0.35
$\Delta S_{5rep,i}$	4.2%	5.3%	4.6%	3.8%	4.1%

In the two worst cases, activation inside the ROI represented 35% to 50% of the total activation. This occurred for the 2 subjects with the lowest number of voxels activated (2 and 6 respectively). For the remaining subjects, activation in the combined ROIs represented on the average 86% of the total activation.

Activation Pattern

Figures 2-2a to 2-2e illustrate the typical pattern of activation. More voxels are activated in the left than in the right hemisphere and the location of the activation corresponds to auditory cortex in the superior temporal gyrus. Figure 2-4 shows the MR signal intensity time course for 16 contiguous voxels for one subject at IL 4. Activated voxels exhibit a regular pattern that follows the 4-minute stimulation cycles of alternating periods of 30 s off and 30 s on.

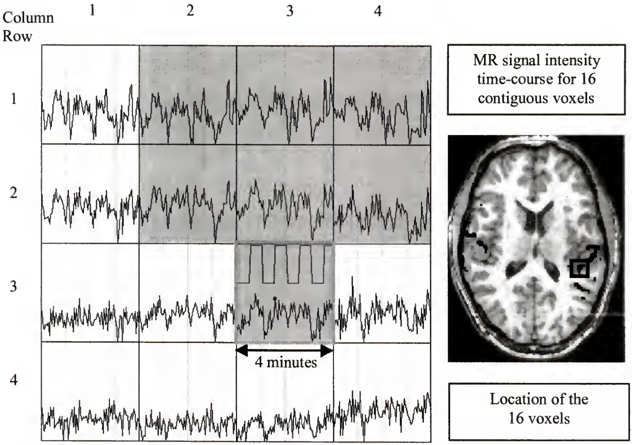
Column
1
2
3
4
Row
1
2
3
4
4 minutes
MR signal intensity time-course for 16 contiguous voxels
Location of the 16 voxels

Figure 2-4: MR signal time course of 16 auditory cortex voxels.
The location of the 16 voxels is represented on the MR image and corresponds to Heschl's gyrus. The reference waveform representing the stimulus presentation is represented in the voxel (3,3). Activated voxels show a MR signal time course similar to the reference waveform and are shaded for identification

Most of the subjects demonstrated activation in auditory cortex, namely the planum temporale (PT), Heschl's gyrus (HG) and the superior temporal sulcus (STS). Table 2-2 displays the number of subjects with "repeated" activation in the right and left PT, STS and HG.

Table 2-2: Number of subjects demonstrating activation in the superior temporal sulcus (STS), the planum temporale (PT) and Heschl's gyrus (HG) per hemisphere.

Anatomical region	***Right hemisphere***	***Left hemisphere***
Planum Temporale (PT)	17/18	15/18
Heschl's gyrus (HG)	8/18	11/18
Superior Temporal Sulcus (STS)	14/18	14/18

Figure 2-5 shows V_{3rep} for each subject in both left and right hemispheres. V_{3rep} varied considerably among subjects: 4 subjects had very small repeated volumes of activation (less than 405 μl), 9 subjects had activation volumes between 540 and 2700 μl and 5 subjects had activation volumes greater than 2700 μl. These differences could not be attributed to obvious characteristics such as age or dextrality. All 18 subjects activated voxels in the left hemisphere and 16 activated in the right. V_{3rep} was greater in the left than in the right hemisphere for 12 subjects, smaller in the left than in the right for 5 and the same in both hemispheres for the remaining subject. V_{3rep} was significantly greater in the left than in the right hemisphere (paired sample t-test, df=17: p=0.046).

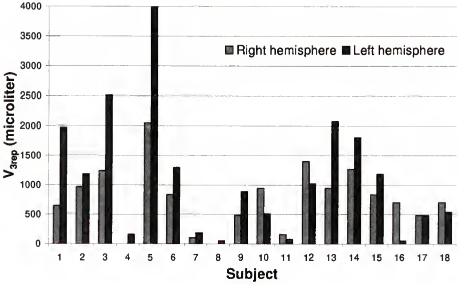

Figure 2-5: Individual volumes of repeated activation in the right and left hemispheres.

Effect of Intensity Level

Table 2-3 presents the mean and standard deviation of ΔS_{3rep} @ IL_{min}, ΔS_{3rep} @ IL_{max} and the resulting ΔR (ΔS_{3rep} @ IL_{max} - ΔS_{3rep} @ IL_{min}) for each hemisphere Table 2-4 presents the same quantities for each individual subject.. Since subjects exhibited a great difference in V_{3rep}, the mean ΔR for all 18 subjects was calculated by weighting each individual ΔR by the corresponding V_{3rep}. In the right hemisphere, 16 subjects had repeated activation. ΔR is positive for all of these subjects (range: +0.33% - +2.41%) and significant for 15 of them ($p<0.05$). In the left hemisphere, all subjects showed repeated activation and ΔR ranged from -0.11 to +4.70%. For 2 subjects, the small number of voxels did not allow calculation of a p-value. Of the remaining 16, 12 showed a significant positive ΔR. The mean weighted ΔR was 1.11% (standard deviation: 0.64%) in the right and 0.85% (standard deviation: 0.80%) in the left hemisphere. Despite the large standard deviations of these measurements, the mean ΔR was significant and positive in both hemispheres (paired-sample t-test, df=17: $p<0.001$ in the right and the left hemispheres).

Figure 2-6 shows the mean ΔS_{5rep} weighted by V_{5rep}, the individual repeated volume of activation, versus intensity level in both hemispheres. These data were obtained for the 9 and 8 subjects having voxels activated 5 times in the left and right hemisphere respectively. With an initial value of 5% at IL 1, ΔS_{5rep} increases to 6.5% at IL 4 and then decreases to 6% at IL 5. Stimulus intensity has an effect on ΔS_{5rep} in both hemispheres (repeated measures, ANOVA: right hemisphere $p=0.039$, left hemisphere $p=0.049$). No significant difference between right and left hemisphere was observed.

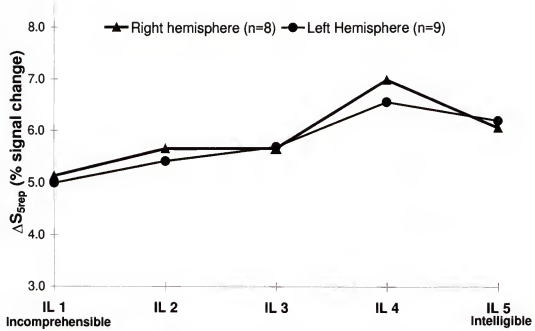

Figure 2-6: The repeated percent signal change, ΔS_{5rep}, as a function of intelligibility level.

Table 2-3: Weighted mean ΔS_{3rep}@IL_{min}, ΔS_{3rep}@IL_{max}, ΔR and respective weighed standard deviation over the 18 subjects. Each mean value was weighted for each subject by V_{3rep}, the volume of repeated activation. The p-value was obtained by testing the hypothesis that ΔR was significantly different than zero.

	Right hemisphere				***Left hemisphere***			
	ΔS_{3rep} @IL_{min}	ΔS_{3rep} @IL_{max}	ΔR	p-value	ΔS_{3rep} @IL_{min}	ΔS_{3rep} @IL_{max}	ΔR	p-value
Weighed mean	4.50	5.61	1.11	0.001	4.35	5.20	0.85	0.001
(std deviation)	(0.88)	(1.10	(0.64)		(0.74)	(0.82)	(0.80)	

Table 2-4: Average percent signal change for "repeated" voxels at the lowest stimulus intensity (ΔS_{3rep} $@IL_{min}$) and at the highest stimulus intensity (ΔS_{3rep} $@IL_{max}$) per hemisphere and per subject. ΔR, the change in response, is the difference between ΔS_{3rep} $@IL_{max}$ and ΔS_{3rep} $@IL_{min}$. P-values are obtained by doing a paired sample t-test on ΔS_{3rep} $@IL_{min}$ and ΔS_{3rep} $@IL_{max}$ for all "repeated" voxels of each subject. Significant p-values at the 0.050 level are highlighted. "NA" (non-applicable) applies either when no voxels are activated or when there are not enough voxels to do a paired-sample t-test.

Subject	***Right hemisphere***				***Left hemisphere***			
	ΔS_{3rep} $@IL_{min}$	ΔS_{3rep} $@IL_{max}$	*ΔR*	*p-value*	ΔS_{3rep} $@IL_{min}$	ΔS_{3rep} $@IL_{max}$	*ΔR*	*p-value*
1	6.17	7.14	**0.97**	**0.002**	4.93	5.36	**0.43**	**0.012**
2	3.95	4.28	**0.33**	0.054	5.05	5.74	**0.69**	**0.050**
3	5.34	6.01	**0.67**	**0.001**	4.94	5.69	**0.75**	**0.001**
4	NA	NA	**NA**	NA	3.87	8.57	**4.70**	**0.005**
5	5.58	6.18	**0.60**	**0.001**	4.83	5.37	**0.54**	**0.003**
6	4.72	5.84	**1.12**	**0.008**	4.31	4.20	**-0.11**	0.351
7	2.93	3.28	**0.35**	**0.027**	4.01	4.21	**0.20**	0.558
8	NA	NA	**NA**	NA	7.40	10.90	**3.50**	NA
9	3.27	3.92	**0.65**	**0.022**	2.85	3.70	**0.85**	**0.001**
10	3.54	4.03	**0.49**	**0.020**	4.86	5.19	**0.33**	**0.030**
11	6.10	8.40	**2.30**	**0.020**	3.43	4.60	**1.17**	0.115
12	4.82	6.57	**1.75**	**0.001**	4.85	5.87	**1.02**	**0.001**
13	4.54	6.95	**2.41**	**0.001**	4.70	6.61	**1.91**	**0.001**
14	3.87	5.62	**1.75**	**0.001**	3.34	3.91	**0.57**	**0.001**
15	3.30	4.35	**1.05**	**0.001**	2.89	5.86	**2.97**	**0.001**
16	4.37	6.30	**1.93**	**0.001**	2.50	3.00	**0.50**	NA
17	3.86	5.16	**1.30**	**0.001**	3.32	4.44	**1.12**	**0.001**
18	3.29	3.78	**0.49**	**0.005**	4.04	4.50	**0.46**	0.215

Discussion

Intelligibility and Sound Intensity

Performance increased significantly from IL 1 to IL 4: intelligibility increasing with increasing sound intensity. A relatively insensitive measure was used (detection of 8 words out of 60) and there was no clear distinction between IL 4 and IL 5. Still 4 subjects showed a decrease in TPF at IL 5 versus IL 4. These results suggest a decrease in intelligibility between IL 4 and IL 5 although sound intensity was increased.

Intra- and Intersubject Variability

From experiment 2, three quantitative conclusions on reproducibility can be drawn. First, up to four-fold variations in activated volumes can occur from one experiment to another within the same individual. Secondly, only 7 to 35 % of the volume of activation for one experiment will also be activated in all replicate experiments. Lastly, for voxels activated in 2 identical experiments, the percent signal change will be within 15% of the mean value in 68% of the time. These results were obtained at near optimal intensity conditions and considered the effects of speech stimuli on only 1 individual. Therefore these values might not be representative of a whole population and with stimuli of different type and intensity. However the reported intrasubject variability estimates agree with the results of a fMRI experiment on visual cortex published by Moser *et al.* (1996). Our data confirm their conclusion that percent signal change ΔS is a more stable measure of activity than volume of activation.

Intrasubject reproducibility in fMRI has been the topic of many papers (Moser *et al.,* 1996, Yetkin *et al.*, 1996). Recent statistical models (Genovese *et al*, 1997, Noll *et al.*, 1997) have presented an experimental method for estimating the specificity and sensitivity of a fMRI protocol. This method requires repeating each experiment 2 to 4 times and could not be implemented retrospectively in this study. Such an approach in future fMRI experiments will allow estimating better margins of errors.

Consistent with other studies (Moser *et al.,* 1996), large inter-subject variations were observed. How much of this variation is attributable to the low intrasubject reproducibility of the activated volume, and how much is due to individual physiological differences is unknown. None of the information gathered from the subjects correlated with the observed variations. Attention has been shown to increase activity in auditory cortex (Binder *et al.*, 1996) and could have contributed to the variability of the results. The level of concentration addressed to identifying the target words varied with IL and probably among the subjects.

Lateralization of Activation

Language is lateralized to the left hemisphere for the majority of right-handers. In this study, the data showed a slight but significant ($p=0.046$) asymmetry in the activation volume towards the left hemisphere, which confirmed the expected asymmetry. However, this result was not significant at the 0.001 level. A mismatch negativity study (Shtyrov *et al.*, 1998) demonstrated that if speech stimuli were presented with a noisy background, the left / right activation asymmetry decreased. Therefore, our weak lateralization could be due to the noisy MR scanner environment, as well as the variability of handedness in the subject population.

The right auditory cortex is shifted slightly anterior relative to the left. It is possible that the choice of ROI might have excluded a small part of the right auditory cortex and resulted in an artifactual predominant activation in the left hemisphere. This would corroborate the many previous functional imaging studies (Strainer *et al.*, 1997. Mazziotta *et al.*, 1982, Petersen *et al.*, 1988, Wise *et al.*, 1991, Zatorre *et al.*, 1992, Binder *et al.*, 1994), which did not find significant lateralization in speech processing induced activation.

Influence of Stimulus Intensity and Intelligibility

Two previous studies investigated the influence of sound intensity on the fMRI response (Millen *et al.*, 1995; Strainer *et al.*, 1997). Meaningful speech stimuli in (Millen *et al.*, 1995) and pure tones in (Strainer *et al.*, 1997) were presented at 2 sound intensities, 20 and 50 dB sensation level. The volume of activation in primary auditory cortex was greater when pure tones stimuli were presented at higher sound levels. With speech stimuli, activation volume in several brain regions did not differ in the two conditions. As stated previously, volume of activation is a more variable quantity than percent signal change. In our study, ΔR, the percent signal change between lowest and highest intensity levels, was chosen as a preferable measure.

Results show an increase in ΔR with increasing IL, which suggests an increase in neuronal activity in auditory cortex between low and high intensity levels. Other factors than can modulate brain response are a) sound intensity, b) the level of attention and c) speech intelligibility. a) Increasing sound intensity has been shown to increase glucose metabolism in central auditory structures (Abrams *et al.*, 1989) and could explain the observed increase in fMRI signal change. Additional support for the importance of sound intensity as a determinant of brain activity comes from the increase of ΔS_{5rep} with increasing IL. The percent signal change of around 5% at IL 1 also supports the effects of intensity on fMRI activation since intelligibility is close to zero at this intensity level. If our data reflect the effects of sound intensity rather than intelligibility, auditory stimuli should be presented at high amplitude to produce optimum activation of the brain. b) As intensity and intelligibility increase, attention and effort are expected to decrease. If our results reflected attention level, a response decrease with increasing IL would have been expected. Our data did not confirm this hypothesis. c) Intelligible stimuli could produce increased activation, which would be expected to occur in association cortex. To distinguish effects of intensity and intelligibility, a separate analysis of primary and association cortex might be useful. It is expected that intensity of any auditory stimulus would affect primary auditory cortex, which processes any auditory input. However, intelligibility, which is the ability to understand the meaning of speech, is expected to affect mainly association cortex where neuronal networks are more specialized compared to primary auditory cortex and where intelligible or meaningful speech is expected to elicit a strong response. Our analysis did not distinguish between these areas, as primary auditory cortex is small considering the fMRI spatial resolution. The small decrease of percent signal change between IL 4 and IL 5 may suggest an effect of intelligibility, which should be confirmed through further investigation. Such a decrease could also reflect habituation or "saturation". An effect of habituation is unlikely since the presentation order was randomized for all subjects. Saturation can be defined as leveling off of brain performance and brain response: as sound intensity increases with IL, the brain could reach the limits of its dynamic capabilities. As the stimuli were played at a reasonably loud intensity, saturation of the auditory system seems unlikely, although background scanning noise has been shown to reduce the dynamic range of the auditory system (Talavage *et al.*, 1998). Saturation effects have been observed in other fMRI auditory experiments investigating the influence of word presentation rate (Binder *et al.*, 1994; Rees *et al.*, 1997), and were also reported while studying the influence of luminance on activation in the visual cortex (Goodyear *et al.*, 1997). If there is truly saturation, auditory stimuli should be presented at an intermediate sound level.

This data do not permit a definite conclusion about the relative contribution of intensity and intelligibility, and it is likely that both affected the fMRI signal as intensity changes caused intelligibility changes.

Conclusion

In summary, intelligibility levels were varied by changing the stimulus intensity. Increased brain activation was observed when intensity level was increased. In both hemispheres a significant positive change in the response ΔR, between lowest and highest IL was noted. Sound intensity influenced the baseline of the fMRI signal. Intensity level influenced the percent signal change of voxels activated at all 5 ILs, which reached its maximum value at IL 4. Intelligibility varied in a similar pattern. Intrasubject variability in volumes of activation and patterns of asymmetry was large. Areas of repeated activation were located in auditory cortex and were significantly greater in the left hemisphere than in the right. In designing fMRI studies, special care should be taken in controlling possible sources of variability such as attention. Functional trials should also be repeated at least twice in order to determine the specificity and sensitivity of the implemented protocol.

Future fMRI studies of auditory cortex need to address the contribution of intelligibility and intensity. Intelligibility could be varied by changing a background noise while keeping sound intensity constant. Experiments with a better spatial resolution are needed in order to distinguish primary and association areas, along with a separate analysis of these areas. Combined with these results, such experiments will guide the optimal presentation for future auditory and language fMRI studies.

CHAPTER 3
MONOEXPONENTIAL T_2 AND ADC MAPPING DURING BRAIN MATURATION OF NORMAL AND HYDROCEPHALIC H-TX RATS

Introduction

What is Hydrocephalus?

Hydrocephalus (HC) is caused by either over-production of cerebrospinal fluid (CSF) by the choroid plexus, under-absorption of CSF in the arachnoid villi or in most cases, obstruction of the CSF flow pathway. It occurs in infants with a frequency of 0.5 to 1.5 per 1000 births. In humans, ventriculomegaly can be diagnosed *in utero* as early as 20 weeks using high-resolution ultrasound. Surgical treatment to drain the excess CSF alleviates the condition and is performed postnatally.

Acute hydrocephalus causes enlargement of the ventricles and interstitial edema, which mostly affects periventricular white matter. CSF crosses the ventricular lining, enters the brain and increases tissue water content (Del Bigio *et al.*, 1994; Jones, Andersohn, 1998). The high hydrostatic pressure causes a decrease in myelin lipids in mature brain and delays myelination in the neonatal brain (Chumas *et al.*, 1994; Hanlo *et al.*, 1997). In addition, it causes a reduction in cerebral blood flow (da Silva *et al.*, 1995) and impairs energy metabolism (da Silva *et al.*, 1994; Harris *et al.*, 1996) Although white matter damage is the main effect observed in adult brain, infantile hydrocephalus also demonstrates gray matter pathology (Boillat *et al.*, 1997). In summary, hydrocephalus combines aspects of ischemia, as cerebral perfusion and metabolism are reduced, and of brain trauma, as the ventricles dilate and stretch the developing brain tissue, or cause compression in the mature brain.

Animal Models for Hydrocephalus

Two rat models for HC are 1) kaolin-induced hydrocephalus; 2) the H-Tx rat with inherited hydrocephalus. In the first model, kaolin is injected into the cisterna magna of the rats, causing an obstruction and inflammation of the CSF flow pathway at the outlets of the fourth ventricle. The procedure is traumatic and animals demonstrate enlarged ventricles a few days post-injection. Kaolin-induced adult rat hydrocephalus has been investigated using diffusion MRI, ^{31}P and ^{1}H MRS (Braun *et al.*, 1997; Braun *et al.*, 1998; Braun *et al.*, 1999). On the other hand, H-Tx rats are born with inherited hydrocephalus associated with aqueduct stenosis (Kohn *et al.*, 1981). The H-Tx strain provides a unique model for naturally-occurring fetal-onset human hydrocephalus. It has been studied for metabolic changes using *in vitro* ^{1}H and ^{31}P MRS and with *in vivo* MRI to assess ventricular size (Jones *et al.*, 1995; Harris *et al.*, 1996; Harris *et al.*, 1997).

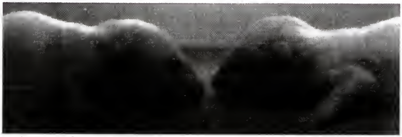

Figure 3-1: Picture of two 4-day-old H-Tx rats.

In the H-Tx rat, there is an increase in tissue water content in the cerebral cortex as early as 4 days after birth (P4, early hydrocephalus) (Jones & Andersohn, 1998). Intracranial pressure (ICP) is slightly elevated at 10 days (P10, intermediate hydrocephalus) and increases steeply between P10 and P21 (advanced-stage hydrocephalus) as the skull becomes fixed. The first two postnatal weeks in normal rats coincide with forebrain dendritic and axonal growth, followed by myelination in the third and to a lesser extent in the fourth week. Hydrocephalic H-Tx rats have abnormal cortical laminations and pyramidal cell structure that are evident in the second and third week (Boillat *et al.*, 1997) and a significant reduction in blood flow and glucose metabolism by P21 (Richards *et al.*, 1989; Jones *et al.*, 1993). The onset and duration of these hydrocephalus-induced phenomena, as well as a few normal developmental features are illustrated in figure 3-2.

Previous MR studies on Hydrocephalus

Most MR investigations not cited above have focused on metabolism using NMR spectroscopy or diffusion changes using MRI.

Bluml *et al.* (1997) used proton MRS in shunted hydrocephalic patients. Patients had normal spectra, and normal concentration of brain water and metabolites. Bluml interpreted these results as a global shrinkage of both intracellular space (i.e., cells) and extracellular space with a proportional loss of osmolytes. In another ^{1}H MRS study, Ra *et al.* (2000) showed that some metabolite levels were depressed suggesting active demyelination but that the neuronal marker NAA was constant, indicating no neuronal loss. These results contradict the changes observed in the H-Tx rat model (Harris *et al.*, 1997; Jones *et al.*, 1997) which show a reduction of the neuronal marker NAA and other metabolites, indicating neuronal atrophy or dysfunction. These results raise the possibility of cell swelling in the H-Tx rat model of hydrocephalus. Overall, MRS studies give contradictory results that seem to be dependent on the severity, acuteness and type of hydrocephalus.

An increase in apparent diffusion coefficient (ADC) has been often reported in the periventricular region of hydrocephalic or shunted humans and animals (Gideon *et al.*, 1994; Braun *et al* ,1997; Ulug *et al.*, 1999; Corkill *et al.*, 2000; Chun *et al.*, 2000; Chang *et al.*, 2000). However, no gray matter edema was observed. Massicotte *et al.* (1999) studied kaolin-induced hydrocephalus in adult rats. They demonstrated a T_2 increase and a transient ADC decrease followed by a large increase consistent with most other studies. However, in the gray matter, T_2 and the ADC decreased. This finding supports the hypothesis of gray matter compression, that may reduce its total water content, while white matter is at first compressed before edema starts developing. The same group showed (Shoesmith *et al.*, 2000) that extracellular fluid movement was different in the cortex of hydrocephalic 4-week-old rats compared to controls. Contrast agent preferentially accumulated in the white matter in hydrocephalic animals and in cortical gray matter in control animals.

Diffusion MRI studies are no clearer than spectroscopy in indicating whether gray matter is affected in hydrocephalus. Because the H-TX rat model is unique in its slowly developing form, the mechanism of tissue damage is not known. There are indications that cell swelling occurs in the advanced stages of the disease and this should lead to an ADC increase. In addition, there is a slight increase in water content of the cortex which may be detected as a T_2 increase. These changes in tissue water content in infantile hydrocephalus are small and take place concurrently with decreases in total water content due to maturation. This occurs not only in gray matter (Johanson *et al.*, 1976; Lehmenkuhler *et al.*, 1993) but also in white matter with the onset of myelination.

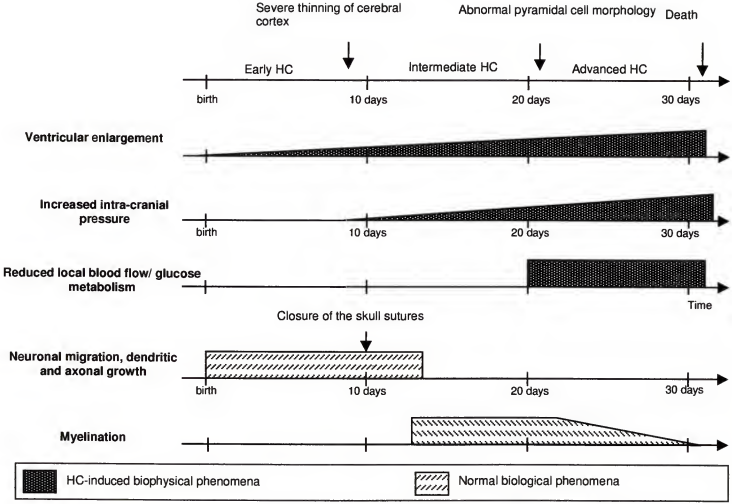
Severe thinning of cerebral cortex
Abnormal pyramidal cell morphology
Death
Early HC
Intermediate HC
Advanced HC
birth
10 days
20 days
30 days
Ventricular enlargement
Increased intra-cranial pressure
Reduced local blood flow/ glucose metabolism
Time
Closure of the skull sutures
Neuronal migration, dendritic and axonal growth
Myelination
HC-induced biophysical phenomena
Normal biological phenomena

Figure 3-2: Sequence of pathological changes in hydrocephalic H-Tx rats in relation to normal maturational events.

Thus sensitive and quantitative *in vivo* techniques are required for evaluation of brain maturation, tissue composition and hydrocephalus pathology. In this chapter, the potential of quantitative magnetic resonance (MR) methodology for diagnostic and prognostic evaluation of early-onset hydrocephalus is reported. Specifically, this study aimed to document the normal values for T_2 relaxation time and apparent diffusion coefficients (ADC) in four brain regions at different maturational stages and to address the differences in quantitative T_2 and ADC between control and hydrocephalic animals in relation to ventricular dilatation. The hypotheses tested were that hydrocephalus would be associated with an increase in T_2 relaxation time in the hydrocephalic brain compared to normal brain, and that maturation effects observed by T_2 and ADC would be less pronounced in the hydrocephalic brain.

Materials and Methods

Animals

Control (C) and hydrocephalic (HC) H-Tx rats were obtained from the breeding colony maintained at the University of Florida. They were studied at three ages, four days after birth (P4) and equivalent to a third trimester human fetus (C, n=7; HC, n=8), 11 days (P11) and equivalent to a newborn human infant (C, n=7; HC, n=8) and 21 days (P21) (C, n=7; HC, n=6). Whenever possible the same animals were examined at all three ages. Due to logistical reasons, however, it was only possible to image 8 of the initial 16 rats at P21 and an additional 5 new animals were scanned at that age.

Imaging Protocol

Animals were anesthetized using halothane (P4 and P11: 0.75%-1%, P21: 1%-1.5%) vaporized in oxygen and nitrous oxide (O_2:N_2O 1:2). A gel warming pad maintained the animal body temperature at a physiological level. All data was acquired at 4.7T on an Oxford magnet equipped with a Bruker (Etlingen, Germany) console and a small gradient insert. A home-built loop-gap coil was used for excitation and detection at P4 and P11. A large pre-tuned quadrature volume coil built by Barbara Beck was used for studies at P21. Six-2 mm thick coronal slices with a 0.5 mm gap were prescribed (FOV 4 cm, matrix: 128x128). Four sets of T_2-weighted (T_2W) and diffusion-weighted (DW) images were acquired using respectively, a RARE sequence (Hennig *et al.*, 1986) (TR/TE 6000/20 ms, ETL 8, effective TE: 11, 54, 96 and 130 ms) and a spin-echo diffusion sequence (Stejskal & Tanner, 1965) (TR/TE 1000/30.3 ms, constant Δ/δ 20/5 ms, 4 b-values: 3, 163, 625, and 1365 s/mm^2, 2 diffusion gradient orientations: right/left, $ADC_{ri/le}$, inferior/ superior, $ADC_{inf/sup}$). Total imaging time was approximately 1 hour.

Anatomical measurements on the 6-2 mm thick images separated by a 0.5 mm gap were compared to others obtained on 1 mm contiguous images acquired with the RARE sequence as described above.

Data Analysis

T_2 and ADC maps were calculated from the T_2W and DW images. A set of T_2W and DW images of a hydrocephalic rat are presented in figures 3-3 and 3-4. In each voxel, signal intensity was fitted to a monoexponential decay function using a non-linear Levenberg-Marquardt algorithm (Marquardt *et al.*, 1963). Four ROIs were manually outlined on the parametric map: the striatum or basal ganglia (BG), the thalamus (TH), cerebral cortex on the most anterior (AC) and posterior (PC) slices, as illustrated on figure 3-5. In the HC group where the cortex is thin, particular care was taken to avoid CSF contamination in the selected ROIs.

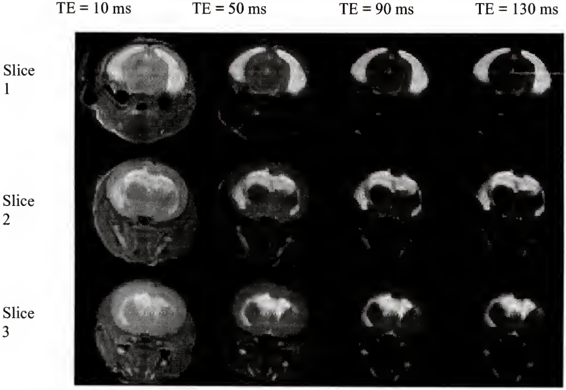

Figure 3-3: T$_2$-weighted dataset of a hydrocephalic rat.

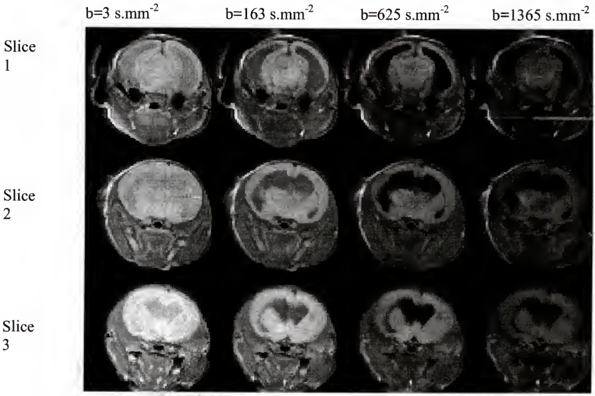

Figure 3-4: Diffusion-weighted dataset of a hydrocephalic rat.

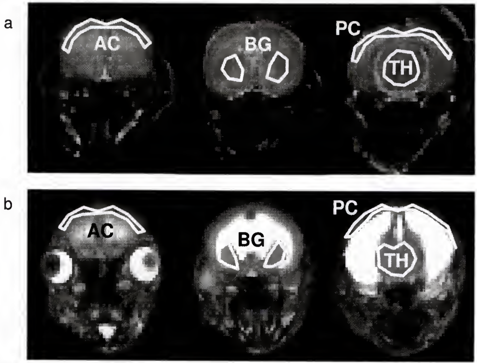

Figure 3-5: Illustration of the ROI location

The accuracy of the ADC and T_2 measurements was investigated by calculating the group coefficient of variation (COV) defined as the standard deviation divided by the group mean and expressed in %. The COV was compared to the group and age changes to assess if measurements were precise enough to extract possible maturation or hydrocephalus-related differences. Because ADC measurements had a large COV, further analysis was performed on T_2 data only. The influence of age, ROI and group on T_2 was assessed using unpaired and paired sample t-tests. The significance level was chosen as $p<0.05$ or $p<0.01$ for all statistical tests.

The rate of change in T_2 (ΔT_2) between P4 and P11, between P11 and P21 and, for rats scanned at all three time-points between P4 and P21, was calculated by linear regression. Unpaired and paired t-tests were used to determine if ΔT_2 (4-21) was different between the C and the HC group and between different ROIs. For each group, paired sample t-tests were used to compare ΔT_2 (4-11) and ΔT_2 (11-21).

Ventricular and total cranial (ventricle + brain) volumes were measured on all slices containing cerebral cortex and subcortical structures. All manually traced areas were multiplied by the slice thickness and summed. When applicable, a linear interpolation scheme accounted for the gap between slices. The percent difference between the higher versus the lower resolution anatomical measurements (i.e., 25-1 mm contiguous slices versus 6-2 mm slice separated by a 0.5 mm gap) was calculated.

The average T_2, ventricular and brain volumes were tabulated as a function of age (P4, P11 and P21), group (C, HC) and ROI. A correlation analysis was carried out to evaluate the influence of ventricular volume on T_2. All data were expressed as a mean ± the standard error of the mean (SEM) unless otherwise specified.

Finally, on 4 animals, ROIs were traced twice at 6 weeks intervals by the same operator and the average T_2 values were compared. The relative percent difference was calculated to estimate the reliability of the parametric measurements.

Results

General Observations

Out of the 3 control animals scanned at all ages, one which had no visible ventricles at P4, showed slightly enlarged ventricles at P11 and more enlargement by P21. Another rat scanned at only P21 and identified as control by outward inspection, had small but identifiable ventricles. Hence these two rats had a less-severe late-onset type of hydrocephalus and were included in the HC group at P21. From the six HC animals scanned at P21, one had extremely severe HC with very little cortex and only data from the thalamus and the basal ganglia could be obtained. Apart from the greatly enlarged ventricles, visual inspection of the image particularly in the periventricular region, did not reveal any obvious differences in signal intensity between control and hydrocephalic animals.

ADC Measurements

The group means and the coefficient of variation of the ADC in both directions (right/left and inferior/superior) are displayed in tables 3-1 and 3-2. Diffusion measurements showed great variability. The coefficient of variation (percentage of standard deviation divided by the mean) of $ADC_{inf/sup}$ was as high as 20% at P21. Changes with age and between groups were in the same order of magnitude or smaller than changes within groups. Therefore, no significant changes with age or groups were observed.

Table 3-1: Mean (in 10^{-3} $mm^2.s^{-1}$) (± COV) $ADC_{inf/sup}$ in all ROIs at the 3 ages.

Group	Age	TH	PC	AC	BG
C	4	1.08 ± 19.1%	1.16 ± 27.0%	1.02 ± 14.8%	0.96 ± 14.0%
HC	4	1.06 ± 12.5%	0.97 ± 21.9%	1.00 ± 14.7%	1.03 ± 14.1%
C	11	1.10 ± 11.1%	0.94 ± 9.8%	0.94 ± 7.2%	0.97 ± 7.7%
HC	11	1.10 ± 14.2%	1.01 ± 12.4%	1.04 ± 14.0%	1.05 ± 10.0%
C	21	1.05 ± 19.7%	1.07 ± 19.2%	1.00 ± 21.5%	0.92 ± 22.0%
HC	21	0.92 ± 34.1%	0.98 ± 21.9%	0.92 ± 8.8%	0.77 ± 20.1%

Table 3-2: Mean (in 10^{-3} $mm^2.s^{-1}$) (± COV) $ADC_{ri/le}$ in all ROIs at the 3 ages.

Group	Age	TH	PC	AC	BG
C	4	1.09 ± 10.9%	1.04 ± 10.3%	1.02 ± 13.7%	0.94 ± 10.4%
HC	4	0.98 ± 11.3%	1.15 ± 20.1%	1.15 ± 17.6%	1.01 ± 13.4%
C	11	1.13 ± 12.9%	0.94 ± 18.1%	1.02 ± 19.7%	0.95 ± 13.8%
HC	11	1.15 ± 7.8%	1.09 ± 24.6%	1.09 ± 22.1%	1.04 ± 10.7%
C	21	1.15 ± 28.1%	1.04 ± 17.8%	0.98 ± 14.9%	0.95 ± 16.7%
HC	21	1.05 ± 19.3%	1.05 ± 17.7%	0.94 ± 14.2%	0.72 ± 17.3%

T_2 Measurements

T_2 measurements for each region and animal group are presented in a tabulated form in appendix A.

Control rats

Regional variations: Significant regional differences occurred in T_2 at P4: T_2 was significantly longer in the PC and AC compared to either TH or BG ($p<0.01$). T_2 in the TH was significantly longer than in the BG ($p<0.05$). T_2 was not significantly different between any region of interest at P11, but was significantly longer in the PC when compared to the AC at P21 ($p<0.05$). These results are illustrated in figure 3-6: *a* indicates a significant difference between both the PC and the AC ($p<0.01$), *b* is significantly different from BG, $p<0.05$, and *c* is significantly different from AC, $p<0.05$, all at the same age. Data are means ± SEM.

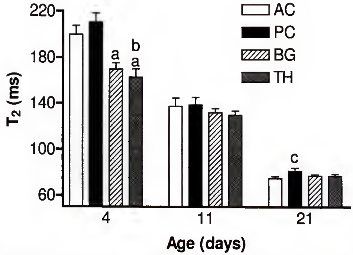

Figure 3-6: Regional comparisons of T_2 in control rat pups at three postnatal ages.

Maturational changes: For C rats, T_2 decreased linearly from P4 to P21 in all ROIs (figures. 3-7a to 3-7d). ΔT_2 (4-21) was significantly different from zero in all ROIs and was, –8.4 ±1.4, –8.9 ±1.0, –5.2 ±0.4 and –4.4 ±0.5 ms /day in the AC, PC, BG and TH, respectively. ΔT_2 (4-21) was significantly larger in the cortex (both PC and AC) compared to the BG or TH ($p<0.05$).

Hydrocephalic rats

Regional variations: At P4 and P21, regional differences were similar to those in the C group. In particular, T_2 was significantly longer in the PC and AC compared to either BG or TH at P4 ($p<0.01$), and in the BG compared to the TH ($p<0.05$). At P21, T_2 in the PC was significantly longer than in the AC ($p<0.05$). In P11 HC rats, T_2 in the PC was significantly longer than in the AC ($p<0.05$). Finally, T_2 in the BG was significantly longer than in the TH ($p<0.01$).

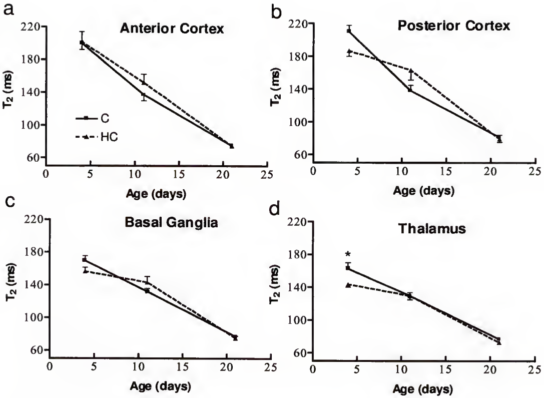

Figure 3-7: Change in T_2 with age in control and hydrocephalic rats in 4 ROIs.

Figure 3-7 presents regional T_2 changes at P4, P11 and P21. * indicates significantly different from HC at the same age, $p < 0.05$. All regions show a significant decrease in T_2 with increasing age. All data show group means ± SEM.

When compared to C rats, the only significant difference was a shorter T_2 in the TH at P4 (early hydrocephalus) ($p<0.05$, figures 3-7a to 3-7d). The same trend was also seen in the PC and BG, although this was not significant.

Maturational changes: ΔT_2 (4-21) for HC rats was: –8.9 ±2.1, –5.6 ±1.6, –3.1 ±1.6, and –3.0 ±1.2 ms /day in the AC, PC, BG, and TH, respectively (figure 4-4). ΔT_2 (4-21) was significantly greater in the cortex compared to the BG or TH and in the PC compared to the AC ($P<0.05$). ΔT_2 (4-21) was never significantly different between HC and C groups.

In contrast to the C group, T_2 changes for HC rats appeared to be less linear over the age range investigated, in that the rate of change between P4 and P11 was smaller in all regions than for C rats. There was a significant difference between ΔT_2 (4-11) and ΔT_2 (11-21) in the HC group in the TH region ($p<0.05$).

Anatomical Measurements

The volume of the forebrain was calculated from the total cranial volume after subtraction of the ventricular volume for HC animals and plotted, together with ventricular volume, as a function of age (figure 3-8). In the control rats, ventricles were too small to be measured and cranial volume was equal to brain volume. The mean cranial (or brain) volume for controls was 538 ± 30 mm^3 at P4, 907 ± 47 mm^3 at P11, and 1157 ± 81 mm^3 at P21. The mean cranial volume for HC rats was 694 ± 51 mm^3 at P4, 1347 ± 85 mm^3 at P11, and 1825 ± 250 mm^3 at P21. Total cranial volume was significantly larger in the HC compared to the C group at all ages ($p<0.05$). The mean ventricular volume for HC animals was 283 ± 26 mm^3 at P4, 719 ± 96mm^3 P11, and 622 ± 301 mm^3 at P21. Brain volume (cranial minus ventricular volume) was significantly smaller in the HC group compared to the C group at P4 and P11 ($p<0.05$) but not at P21. The average increase in ventricular volume in HC rats was 56 mm^3 / day.

Figure 3-8 shows anatomical measurements versus age for control rats (◆) and for hydrocephalic rats (■). For HC rats (▲), brain volume was calculated from ventricular volume (shaded area). At P4 and P11 the brain tissue was significantly reduced in HC rats ($p < 0.05$). Because of the large variation in ventricle size at P21, the difference was not significant but the same trend was present. Data are means ± SEM.

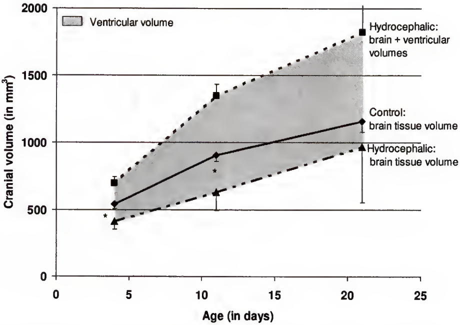

Figure 3-8: Graph of volume (cortical + sub-cortical structures) versus age.

Verification of Anatomical Measurements

Table 3-3 presents the influence of high- versus low-resolution data acquisition parameters on the measurement of the volume of brain or ventricles in 4 rats. In all cases, the relative difference in anatomical measurement was less than 10%.

Reproducibility of T_2 Measurements

Table 3-4 presents reproducibility measurements on 4 rats at P4 and P11. When measured by the same person, all T_2 values in each ROI were reproducible within 10% and most of them within 5%.

Table 3-3: Accuracy of anatomical measurements.
The volume measured using 6-2 mm slices with a 0.5 mm gap, the volume measured with 25-1 mm contiguous slices, and the relative percentage difference is presented.

Rat	Age (in days)	ROI	Volume (in mm^3) 2 mm + 0.5 mm gap	Volume (in mm^3) 1 mm contiguous	% difference
1	22	Brain	3199	2936	8.6
2	22	Brain	2165	2162	0.1
3	22	Brain	1471	1533	-4.1
4	8	Brain	1729	1810	-4.6
1	22	Ventricles	2416	2488	-2.9
2	22	Ventricles	982	941	4.3

Table 3-4: Reproducibility of T_2 measurements in the 4 ROIs.
Reproducibility was calculated as the difference in the 2 measurements divided by the mean of the 2 measurements. It is expressed in relative percentage. Four rats were used, 2 controls (C1 and C2) and 2 hydrocephalic (H1 and H2) at 2 ages (P4 and P11).

Rat	Age	Thalamus	Posterior cortex	Anterior cortex	Basal ganglia
C1	P4	5.6%	-1.6%	-2.2%	-2.1%
C2	P4	-6.9%	-3.5%	-3.0%	-3.7%
H1	P4	-0.6%	-3.5%	3.0%	-6.1%
H2	P4	-1.2%	0.7%	2.0%	-5.0%
C1	P11	-2.5%	3.7%	-3.2%	-0.3%
C2	P11	-1.2%	-2.1%	-1.4%	-0.3%
H1	P11	-2.2%	-4.2%	-3.2%	1.2%
H2	P11	-1.5%	-5.6%	6.0%	3.0%

Discussion

Anatomical Measurements

The data shows that in hydrocephalic rats, ventricular volume at specific postnatal ages and the rate of increase with age (56 mm^3/day) were similar to values previously reported (Harris *et al.*, 1992; Jones *et al.*, 1995). The cranial volume of hydrocephalic rats has not been previously reported and, as anticipated, it was significantly greater than cranial volume of age-matched control rats, due to the overall expansion of the skull. However, the brain tissue volume was smaller in HC rats compared to controls. This result did not reach statistical significance at P21 because of the extremely large range of values, which included the two rats with mild late-onset HC. Nevertheless, this suggests that although brain expansion occurs with maturation in parallel with that of control rats, HC animals do develop the same amount of brain tissue as control rats. This is supported by previous studies showing that the cerebral cortex of HC rats although longer than controls, does not achieve full thickness even in the early stages (Jones *et al.*, 1991; Harris *et al.*, 1992; Jones *et al.*, 1995) and that the development of deep cortical laminae is disturbed (Harris *et al.*, 1994; Miyan *et al.*, 1998). These measurements show that the disturbances of the cortical layer growth result in a macroscopic loss of tissue that is detectable with MRI.

Monoexponential Measurements of ADC

The diffusion measurements exhibited a large variability, which obscured potential changes with age or condition. Therefore, no conclusions could be drawn from our measurements. Variability can be attributed to the non-reproducible positioning of the animals. Given that ADC was measured along the right-left and inferior-superior directions, a rotation of the animal relative to these orientations would have affected the diffusion measurements. In addition, the gel-warming pad did not provide reliable heating and the ADC decreases by 2.4% per degree Celsius. (Le Bihan *et al.*, 1989). Several very cold young animals were taken out of the scanner after the imaging session. The temperature drop was less pronounced with increasing age, as around 8-days-old, rat pups start growing hair that protect them from the cold. Therefore to obtain reliable and accurate diffusion measurements, it is necessary to use a rotationally invariant quantity such as the diffusion trace (see chapter 1). The increased imaging time when the trace is acquired was not possible without an improved animal heating system. Therefore, a water blanket was designed for future experiments.

Monoexponential Measurements of T_2

Strategies to obtain fast and accurate relaxation parameter maps have been much debated. The two critical steps are the choice of 1) an adequate acquisition protocol and 2) the curve-fitting routine (Whittall *et al.*, 1997; Whittall *et al.*, 1999).

Acquisition protocol

In this study a long TR – 8-echo RARE sequence (ETL 8; 4 images per acquisition; 1 acquisition, TR = 6000 ms) was chosen. Therefore, two consecutive echoes during each repetition time were used to reconstruct each image. Consequently, the T_2-weighting of the images governed by the effective TE was close to the T_2-weighting obtained by repeating standard spin-echo acquisitions. However, the 4 images were collected in one acquisition and this allowed selection of a long TR (reducing the amount of T_1-weighting) while keeping the acquisition time reasonably short. Such an approach was suggested by the results of Liney *et al.* (1996) and a more detailed study of the optimum choices of RARE parameters for accurate T_2 mapping is presented in chapter 5.

The large spread of the chosen echo times (10 to 130 ms) was designed to give good sampling of the T_2 decay curve. However, due to the unexpectedly long T_2 observed at P4 (up to 230 ms), it is possible that T_2 values were overestimated especially at the earliest time point and therefore, a longer effective TE should be chosen in any future study.

Fitting routine

In a homogeneous sample, the ^{1}H MR signal intensity decreases monoexponentially as a function of echo time with the characteristic time-constant equal to the spin-spin relaxation time (T_2) of the sample water. Living tissue consists of several pools of water all of which contribute to the MRI signal. For example, human white matter MR signal can be characterized by two T_2 components, with the shortest representing water bound to myelin, a longer one representing extracellular and intracellular water (Whittall *et al.*, 1997). The same study showed that gray matter in the caudate, putamen and cortex were accurately represented by one T_2 component unless there was a bit of CSF contamination, represented by a very long T_2. In addition, Pfeuffer et al (1998) found only one T_2 component in adult rat brain. Finally, it is generally considered that in the brain, the different pools of water are in fast exchange. Consequently, an accurate T_2 characteristic can be obtained by fitting the signal intensity acquired at different echo times to a monoexponential decaying function.

However, in the case of volume averaging of tissues with substantially different T_2, such as CSF and gray matter, the monoexponential assumption is no longer valid. In the specific case of hydrocephalus, CSF (which has a very long T_2) contamination would cause an apparent T_2 increase. However, in this study, there is no such evidence because T_2 was shorter for HC rats than for C rats at P4. Thus it was anticipated that the monoexponential fitting routine would be accurate for the type of tissue and pathology investigated.

Brain T_2 Relaxation Time

T_2 values were reported to range from 45 ms to 90 ms in adult rat brain in a review from Akber et al. (Akber, 1996). In a more recent study, T_2 values of 63-66 ms were obtained at 4.7T, in both cortex and striatum of normal adult rats (Loubinoux *et al.*, 1997). These values are somewhat lower than the P21 values of 75-81ms obtained here. However, brain maturation continues after P21 in rats and further reductions in T_2 are to be expected between P21 and adult.

Using MRS at 4.7T, water content and T_2 were measured in freshly-excised cortical gray and white matter of normal neonatal rats up to 8 weeks old (Masumura, 1987). T_2 values of 101, 73 and 61 ms were recorded at P7, P14, and P21, respectively. This time is consistently shorter when compared to the results of this study, although the discrepancy was less at P21. However, since the acquisition protocol was not described, the experiments are hard to evaluate. In another study at one week of age, T_2 values of 73.5 ms were reported for rat brain *in vivo*, which is much shorter than the values found here (Tuor *et al.*, 1998). The data was obtained using a TR of 1.2s, which is short relative to the T_1 of the tissue and could have led to an underestimation of T_2.

Maturation-related T_2 Changes

A decrease in T_2 with age is consistent with studies on human (Holland *et al.*, 1986) and animal brains such as the kitten (Baratti *et al.*, 1999) dog and baboon (Miot-Noirault *et al.*, 1997). Although early T_2 values in the rat have not been reported previously, other altricious species have high T_2 values soon after birth, similar to the present study (Berenyi *et al.*, 1998; Baratti *et al.*, 1999). The reduction in spin-spin relaxation time during development can be related to several factors such as 1) a maturational decrease in brain water content, 2) onset of myelination (Miot-Noirault *et al.*, 1997), 3) increased macromolecular (particularly protein) content (Berenyi *et al.*, 1998) and 4) the associated reduction in extra-cellular space that restricts free water motion (Lehmenkuhler *et al.*, 1993).

The cortical water content as a percentage of the wet weight decreases from 89% at P4, to 86.5% at P11 and 81.5% at P21 in normal rats (Jones *et al.*, 1997). When T_2 is plotted as a function of water content in the posterior cortex, there is good correlation between the decrease in water content and T_2 changes during maturation ($r^2 = 0.99$). The average change in T_2 is 17 ms per 1 % decrease in water content for control rats (see Figure 3-9).

Berenyi *et al.* (1998) investigated developmental changes in normal and fluid-deprived rabbits from birth to P4. Neither T_2 nor water content decreased significantly in normal suckling animals. In contrast, the T_2 of fluid-deprived animals decreased significantly at a rate of 15 ms per 1% reduction in water content. Using a biexponential analysis, the reduction in T_2 in the fluid-deprived animals was interpreted as a decrease in bound water fraction, accompanied by a reorganization of brain water compartments to compensate for dehydration and maintain cell volume.

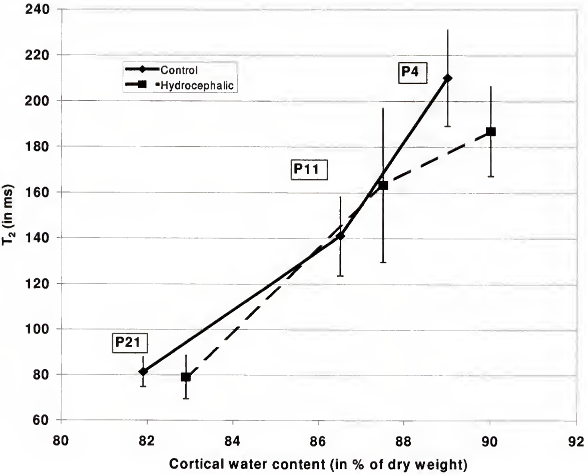

Figure 3-9: T_2 (in ms) versus cortical water content taken from (Jones *et al.*, 1997) (in % dry weight) in the posterior cortex.

The rat brain T_2 decrease with maturation observed on a 3 week time scale is probably due to 1) changes in the relative fractions and relaxation characteristics of the different water pools, such as those reported by Berenyi *et al.* (1998) and 2) the significant reduction in total water content. Interestingly, the *quantitative* changes in T_2 with water content in the brain following dehydration in the rabbit (–15 ms per 1 % decrease in water content) are similar to those reported in this study of rat brain maturation (–17 ms per 1 % decrease in water content), suggesting similar mechanisms are responsible for these two processes.

Regional Differences

In this study at P4 and to a lesser extent at P11, T_2 was higher in the cortex than in the basal ganglia or thalamus. Water content at P4 as a percentage of dry weight is significantly higher in the cortex compared to thalamus (H.C. Jones, unpublished observations). This is consistent with the regional variations in T_2 at P4 and P11 and confirms the correlation betweenT_2 and water content (ie. T_2 decreases with water content). The different regions develop at different rates and by 21 days, all have matured to the same level, as measured by T_2.

Hydrocephalus-related T_2 Changes

Overall, there were few differences in T_2 between control and H-Tx hydrocephalic rats. In this regard, the H-Tx model is similar to the kaolin-induced model where gray matter did not show signs of edema (Braun *et al.*, 1997; Braun *et al.*, 1998). However, studies on the adult kaolin-induced HC have reported areas of hyperintensity in the periventricular white matter. Because of the small size of the rat brains in this study, it was not possible to measure T_2 separately in the periventricular white matter, but it did not show any obvious change in signal intensity at any stage of hydrocephalus. The absence of periventricular white matter edema could possibly be attributed to the slow-developing form of HC in the H-Tx rat model, in contrast to the more traumatic kaolin-induced adult form.

T_2 is a recognized indicator of extracellular edema, either vasogenic or interstitial, and has been used to follow changes in ischemia and trauma. However, the sensitivity of T_2 to small changes in water content and delayed maturation, particularly in a more chronic pathology, has not been characterized. The only significant group difference was observed at P4 where T_2 was lower in the thalamus of hydrocephalic animals and since the same trend was also present in the posterior cortex and basal ganglia, this appears to be a general finding. One possible explanation is that maturation is retarded and the tissue is less differentiated than normal with a high cellular density, as found in the brains of preterm infants (Felderhoff-Mueser *et al.*, 1999). By P21, the T_2 values for all brain regions were the same as for control rats.

It was anticipated that any difference between control and hydrocephalic rats would be predominant in the posterior cortex, where the pathology is most severe and water content is increased by 1% (Jones *et al.*, 1997). Water content at P4 was also measured in a second study (H.C. Jones, unpublished observations), and was significantly higher than controls in the both the cortex and thalamus ($p<0.05$) and insignificantly increased in the basal ganglia. This study showed that the raised water content due to hydrocephalus was not accompanied by a ~17 ms increase in T_2 that was expected from maturation data. It appears that either the biological heterogeneity (see error bars) hides the T_2 changes due to hydrocephalus or that hydrocephalus-related changes in water content are different from the changes with maturation. In both cases, further investigation is needed for example using a biexponential analysis (Berenyi *et al.,* 1998), that will give an indication of the status of the bound and the free water. Such an analysis was not be performed as it required acquisition protocol changes.

Rate of Change of T_2

The rate of change of T_2 in the HC group was much lower between P4 and P11, compared to P11 and P21. Between P11 and P21, the skull bones fuse and ICP increases. Whereas, the cortical tissue was stretched previously, it now becomes compressed. The transition from early to advanced HC may affect the mechanisms of T_2 shortening in the brain of HC rats. For example, as the tissue is stretched in early HC, normal reduction in T_2 with maturation might take place in hydrocephalic rat brains. However, when the skull plates begin to fuse (i.e., after P11), in addition to the "normal" maturation changes that take place between P4 and P11, the density of macromolecules increases due to high ICP and the bound water fraction increases rapidly, causing a more rapid T_2 decrease after P11 in hydrocephalic brain.

Conclusion

In conclusion, T_2 and ADC values for different areas of the brain have been measured in neonatal rats as young as 4-days-old and during their first 3 weeks of life. The protocol needs to be improved to obtain accurate ADC measurements and these will be presented in chapter 5. The reduction in T_2 with age was highly significant and showed regional variations. Few differences were observed between H-Tx control and hydrocephalic animals, suggesting that brain regulatory systems are effective in this non-traumatic model of hydrocephalus. It is concluded that T_2 is sensitive to the changes in water content as low as 1% during normal maturation but not to the 1% change found in H-Tx hydrocephalus. This suggests that different water pools are responsible for the two processes. Therefore, to monitor the progression of neonatal hydrocephalus and the efficiency of shunt treatment, future work will aim to resolve the behavior of the different water pools through a combination of multiexponential T_2 and diffusion measurements (Gideon *et al.*, 1994).

Shunt-treatment causes a dramatic change in ICP as brain tissue which was compressed, is suddenly released. This traumatic event has been shown to change diffusion characteristics of the tissue (Ulug *et al.*, 1999; Gideon *et al.,* 1994) and is probably due to cell swelling and restoration of a normal ECS. However, monoexponential T_2 changes, particularly in the acute phase, were not previously investigated and will be presented in chapter 4.

CHAPTER 4
MONOEXPONENTIAL T_2 MAPPING FOR MONITORNG OF SHUNT TREATMENT OF NEONATAL HYDROCEPHALIC RATS

Introduction

In humans, ventriculomegaly (enlarged ventricles) can be diagnosed *in utero* as early as 20 weeks using high-resolution ultrasound. In the large majority of cases, the treatment consists of inserting a shunt device into the ventricles to drain out the excess fluid, usually into the peritoneal cavity: this "shunting" process is illustrated on figure 4-1. Shunting is not initiated *in utero*, but it can be performed either on a premature or term baby. Although the treatment alleviates the condition, it is not clear what factors are determinant for a good neuronal outcome. It is probable that the intervals between onset and diagnosis and subsequently between diagnosis and treatment are critical for limiting irreversible brain damage.

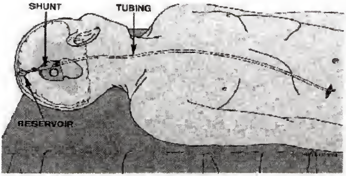

Shunt tubing in place

Figure 4-1: Placement of a peritoneal shunt.

Shunt treatment in the H-Tx rat model was investigated using various techniques. Using MRI, Jones *et al.* (1995) studied shunting at two post-natal ages, 3-6 or 8-12 days after birth. The study determined that the operation resulted in a significant decrease in ventricular volume. In addition, the time of shunting did not affect the reduction in ventricular and brain volumes. In another study, Jones *et al.* (2000) measured electrolytes, metabolites and studied the appearance of cortical cells in early and late-shunted rats 21-days-old. Hydrocephalus-impaired dendritic architecture was partially restored and interstitial edema was improved by early shunt. However, the intracellular K^+ was much lower than in controls, an indication of some irreversible damage. Finally, metabolite concentrations showed some irreversible changes in membrane composition but the reduction in energy metabolites due to hydrocephalus was prevented. In late shunted rats, dendritic architecture was more abnormal than in early-shunted pups. Interstitial edema was marginally better than in early shunted animals however, the decrease in K^+ was more severe. Finally, although membrane compounds were similar to early-shunt rats, energy metabolism was still impaired despite a late-shunt.

In another study, Del Bigio *et al.* (1997) studied shunt-treated rats using MRI for ventricular size assessment and behavioral tests for cognitive and motor impairments. Hydrocephalus was induced in 3-week-old rats using kaolin and shunting was performed 1 or 4 weeks later. MRI showed a periventricular edema. Behavioral dysfunction was prevented by early but not late shunt.

These results demonstrate the importance of the timing of shunt treatment. However, to measure efficacy and monitor tissue functionality in humans, it is crucial to develop *in vivo* quantitative indexes. Steps towards this goal will be presented in this chapter.

Chapter 3 presented brain ADC and T_2 measurements of a non-acute (genetic) model of hydrocephalus, the H-Tx rat model. Results showed that ADC measurements were not reliable without an improved set-up (which will be presented in chapter 5). T_2 measurements presented few differences between control and hydrocephalic H-Tx rats in this progressive model of HC, indicating regulated water distribution as the brain develops slowly. Shunting of the animal is, however, an acute event and T_2 is known to lengthen due to edema that follows brain trauma (Barnes *et al.*, 1986; Brant-Zawadzki *et al.*, 1984; Thatcher *et al.*, 1998) and hyponatremia (low concentration of sodium in the blood causing extracellular water accumulation) (Vadja *et al.*, 1999). In this chapter, the mechanisms of shunting were investigated with a monoexponential T_2 analysis. More specifically, the contribution of surgical trauma, anesthesia, and relief of intracranial pressure on T_2 changes was investigated. The goals were to determine if there was formation of edema due to the operation and if CSF infiltrated the brain tissue in shunt operated rats. Another hypothesis tested was that temporal T_2 changes and efficient CSF drainage would be correlated. Finally, the possibility of dehydration during operation and its effects on T_2 were investigated.

Materials and Methods

Animals

Neonatal H-Tx rats were selected and imaged at 8, 9, 10, 14 and 21 days after birth (P8, P9, P10, P14, P21 or pre-shunt, and 1, 2, 6 and 13 days post-shunt or post separation). Throughout the experiment, animals were anesthetized using 0.75 to 1%

inhaled halothane (2:1 O_2/N_2). Body temperature was maintained either with a heating gel pad or a specially designed heating blanket (see chapter 5). Six groups of animals were investigated (see table 4-1): hydrocephalic shunt-operated (HON: Hydrocephalic Operated No-fluid), control sham-operated (CON: Control Operated No-fluid), control separated from the mother without fluid supplements (CNN: Control Not-operated No-fluid) and controls separated from the mothers with fluid supplements (CNF: Control Not-operated with Fluid), hydrocephalic shunt-treated with fluid supplements and control sham-operated with fluid supplements (HOF: Hydrocephalic Operated with Fluid and COH: Control Operated with Fluid).

Eight hydrocephalic rats were shunted (HON: n=8) and 4 controls were sham-operated (CON: n=4) at P8, after the first scanning session (~ 6 hours after the 1st imaging session and 17 hours before the 2nd session). The surgical operation was performed under anesthesia. It consisted of inserting a sterile tubing that connected the ventricles to a subcutaneous compartment of the peritoneal cavity, therefore draining the CSF from the hydrocephalic rat brains. Six control animals were anesthetized after the first scanning session, to simulate anesthesia and separation from the mother during shunt-operation. Half of these animals were administered a dose of fluid to compensate for possible dehydration during anesthesia (CNF group, n=3) while the others were not (CNN group, n=3). The fluid supplementation protocol consisted of injecting subcutaneously before and after each anesthesia, a solution of 0.9% NaCl and 2.5% dextrose (does: rate: 3 ml/kg/hr). Of the eight HON rats, one died at P9 and one died at P14. One of the four CON rats died at P14. One of the CNN animals was separated from the mother after the first scanning session but not anesthetized and was therefore discarded from the analysis. Finally four additional hydrocephalic and four control rats were shunted and sham-operated respectively and were administered fluid supplements (HOF: n=4; COF: n=4).

Hydration was measured before each scanning session for both CNF and CNN groups. Blood was drawn from one of the major tail veins of the rats and collected in a 84.8 μl capillary tube. Blood was then centrifuged to separate plasma and red blood cells. Finally, plasma protein concentration (in mg per 100 ml of serum) was measured using a refractometer.

Imaging Protocol

Data were acquired on a 4.7T/33cm Bruker instrument equipped with a small gradient insert capable of 220 $mT.m^{-1}$ (Bruker, Etlingen, Germany). A home-built loop-gap (P8, P9, P10 and P14) and a pre-tuned quadrature volume (constructed by Barbara Beck) (P21) RF coil were used for excitation and reception. Six-2 mm thick coronal slices with a 0.5 mm gap were prescribed (FOV 4x4 cm^2 and 6x6 cm^2, matrix: 128x128). Four sets of T_2-weighted (T_2W) images were acquired using the previously presented RARE (TR/TE 6000/20 ms, ETL 8, effective TE: 11, 54, 96 and 130 ms). In the HON and CON rats, sets of DW images were also acquired with spin-echo diffusion sequences (TR/TE 1000/30.3 ms, constant Δ/δ 20/5 ms, 4 b-values: 3, 163, 625, and 1365 s/mm^2, 2 diffusion gradient orientations: right/left, $ADC_{ri/le}$, inferior/ superior, $ADC_{inf/sup}$). Because the measurements were very variable (see chapter 3), this method was abandoned for the CNN and CNF groups.

Data Analysis

Using a non-linear fitting Levenberg-Marquardt algorithm (Marquardt, 1963), T_2 maps were calculated using a mono-exponential decay model applied on a pixel-by-pixel basis. Four ROIs were manually outlined on the parametric maps: the basal ganglia (BG), the thalamus (TH), cortex on the most anterior (AC) and posterior (PC) slices. In the HON groups, ventricular volume was measured to evaluate the efficacy of shunt treatment.

Average T_2 was tabulated as a function of age, group (HON, CON, CNF, CNN, HOF, COF) and ROI. The rate of change of T_2, ΔT_2, was calculated between consecutive time points ($\Delta T_2(8\text{-}9)$, $\Delta T_2(9\text{-}10)$, $\Delta T_2(10\text{-}14)$, $\Delta T_2(14\text{-}21)$). Mean protein concentration was calculated for the CNF and CNN groups. All data was reported as mean (± SEM) unless otherwise specified.

Independent and paired sample t-tests were carried out (statistical significance: $p<0.05$ or $p<0.01$) to compare the 6 groups. In addition, control and hydrocephalic data presented in chapter 3 (P4, P11, P21) were extrapolated to time points used in this part of the study and compared to the newly acquired data.

CSF volumes in and peripheral to the ventricles were measured on all slices containing cerebral cortex and subcortical structures. All manually traced areas were multiplied by the slice thickness and summed. When applicable, a linear interpolation scheme accounted for the gap between slices. Two measures of shunt efficiency, the relative reductions in ventricular volume and in total amount of CSF, were calculated. A correlation analysis was carried out to investigate the dependence of the acute change in

T_2 versus shunt efficiency. Particular attention was given to the acute stage of brain decompression (changes between P8 and P9).

Results

Shunt efficiency

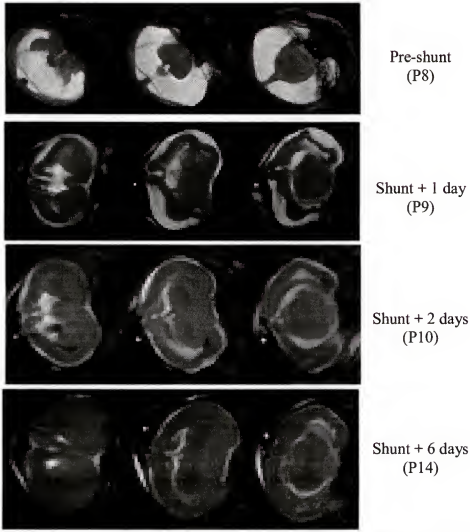

Figure 4-2: Three slices from a hydrocephalic rat pre-shunt, 1 day, 4 days and 6 days post shunt.

Figure 4-2 shows an example of successful shunt in that excess CSF has been drained and the tissue has expanded, giving a normal appearance to the brain by P14.

Figure 4-3 displays the reduction in ventricular volume for each rat. In one rat, the shunt became obstructed and CSF accumulated again. At P21, 5 of the 6 remaining HON rats showed good drainage of the CSF and the rat with clogged shunt was discarded from the analysis. In one rat of the HOF group, the shunt did not result in the reduction of the ventricles and the data was analyzed but not included in the HOF mean values.

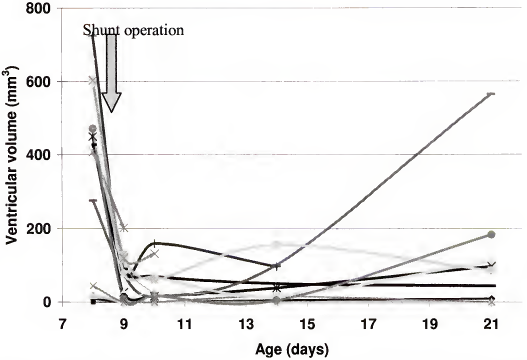

Figure 4-3: Temporal evolution of individual ventricular volume (in mm^3) after shunt treatment as a function of age.

General Observations

A few animals died, either due to the strenuous scanning conditions or because they were not fed properly by their mothers (see table 4-1). No attempt was made to increase the number of animals in the COF and HOF groups from P10 onwards, as previous data indicated that the major T_2 differences occurred in the acute stage and these data were acquired to support the hypotheses postulated from previous results.

Table 4-1: Number of animals included in each group for the T_2 analysis.

	P8	**P9**	**P10**	**P14**	**P21**
CON	4	4	4	4	3
HON	8	7	7	7	6
CNF	4	4	4	4	4
CNN	3	3	3	3	3
COF	3	3	2	2	1
HOF	3	3	3	1	1

Regional and Temporal Differences

Tables B-1 to B-4 and B-5 to B-8 of appendix B present the mean T_2 and mean rate of change of T_2 respectively, in the 4 ROIs for the 6 animal groups. In addition, extrapolated control values are presented. Figure 4-4 a) to d) present CON, HON, CNN and CNF results in the graphical form and indicate significant time and group differences.

Comparison of CON and HON

Temporal T_2 changes: At P8, T_2 was significantly longer in the PC than the AC or the BG and was the shortest in the TH. All rats showed significant shortening in T_2 in all ROIs between P8 and P9 and effects were predominant in the cortex: $\Delta T_2(8\text{-}9)$ was 29 and 35 ms in the TH and 80 and 53 ms in the PC of the CON and HON groups, respectively. Between P9 and P10, T_2 did not change significantly in any group, except in the AC of CON rats. Between P10 and P14, T_2 decreased significantly in all ROIs of both groups. $\Delta T_2(10\text{-}14)$ was -10, -11, -7 and -8 ms / day in the PC, AC, TH and BG of HON rats and -4, -4, -5 and -7 ms / day for CON rats. (significant in PC and AC). Finally, between P14 and P21, T_2 decreased significantly in all ROIs for both groups ($\Delta T_2(14\text{-}21)$ ~-2 to -5 ms / day).

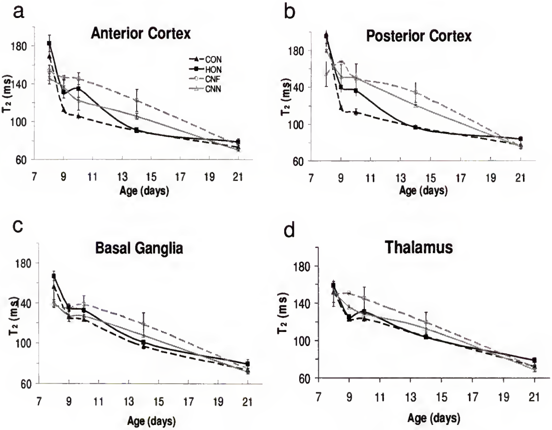

Figure 4-4: T_2 changes with age in a) anterior cortex, b) posterior cortex, c) basal ganglia and d) thalamus of the HON, CON, CNN and CNF groups.

T_2 CON-HON group comparisons: At P8, both groups had similar T_2s (~160-190 ms) in all ROIs. At P9 and P10, T_2 of HON pups was significantly longer than in CON rats in the PC, AC and BG and a similar trend was present in the TH. This difference in T_2 was greater in the cortex (~20 ms) compared to the BG (~10 ms). At P14 and P21, HON and CON rats had similar T_2s in all ROIs.

Comparison of CNF and CNN

Temporal T_2 changes: CNF rats showed no change in T_2 between P8 and P10. In fact, individual data even showed that T_2 increased in some rats. Between P8 and P9, T_2 of all CNN rats shortened in all ROIs. However, due to the small sample size and the variability in T_2 values at P8, the results were not significant. In CNN rats, the effect was predominant in the PC where $\Delta T_2(8\text{-}9)$ was -28 ms / day compared to -8, -13 and -17 ms / day in the AC, BG and TH respectively. Between P9 and P10, T_2 did not change in the CNN group. T_2 decreased between P10 and P14, in all ROIs. The effect was only significant in the BG of NR and CNN ($\Delta T_2(10\text{-}14) \sim -5$ ms /day) and the TH of CNF rats ($\Delta T_2(10\text{-}14) \sim -6$ ms /day). Between P14 and P21, T_2 decreased significantly in all ROIs of both groups and $\Delta T_2(14\text{-}21)$ was -5 to -7 ms / day in all ROIs.

T_2 CNF-CNN group comparisons: At P8, T_2 was significantly smaller in the PC of CNF rats (154 (±13) ms) compared to CNN (180 (±2) ms) rats. At P9 and P10, T_2 was smaller in CNN compared to the CNF groups in all ROIs. However, due to the small sample size, the effect was only significant at P9 in the TH and BG (136 (±1) ms and 127 (±2) ms for CNN rats versus 150 (±3) ms and 135 (±2) ms for CNN rats). T_2 was not different in the 2 groups from P14 until P21.

T_2 comparisons with C rats: T_2 in CNF rats was never different to age-matched control rats, except at P21 in the TH. In CNN rats, T_2 in the AC was always shorter than in C rats and this was significant at P10 as well as in the BG and PC at P21.

Comparisons of SH, SO, CNF and CNN groups

Posterior cortex: Pre-shunt (P8), T_2 in the CON and HON groups were significantly greater than in the CNF group. At P9, T_2 decreased in the SH, CON (significantly) and CNN (non-significantly) groups but not in the CNF group. The rate of decrease was significantly faster in CON compared to HON and CNN groups. At P9, T_2 decreased from the CNF/CNN group, to the HON group and to the CON group. No groups showed significant changes between P9 and P10. At P10, FR, CNN and HON rats had similar values of T_2 which was significantly greater than T_2 in S0 rats. At P14, T_2 in CON and HON had significantly decreased to 96 ms and were both significantly smaller than in CNF and CNN groups. At P21, T_2 had decreased significantly in all groups and this change was more rapid in CNF and CNN rats compared to HON and CON rats. Consequently, the resulting T_2 was similar for all groups.

Anterior cortex: Trends observed in the AC were similar to those reported in the PC. In addition, T_2 in CNF/CNN groups was significantly shorter than in HON/CON groups.

Thalamus: At P8, T_2 was similar in all 4 groups. T_2 shortened at P9 in all groups except the FR. This effect was greater in the HON and CON compared to the CNN. At P10 and P14, there were no significant group differences although CON and HON values tended to be shorter than the ones of CNF and CNN. Between P14 and P21, T_2 decreased significantly in all groups but the rate was faster in FR, compared to CNN/HON compared to CON rats. At P21, T_2 decreased significantly from the HON/CON group to the CNN and CNF groups.

Basal ganglia: The BG was the area that exhibited the least time and group differences. At P8, the HON group had a significantly longer T_2 than in the CNF/CNN groups. At P9, T_2 dropped in all groups except in the CNF and it was only significant in the HON group. At P10 at P14, similarly to P9 and to data in other ROIs, T_2 tended to be increasingly longer from SO, to HON to CNN, and to CNF rats and the difference was significant between CON and HON rats at P10 and between CNN and CON rats at P14. Between P14 and P21, T_2 decreased significantly in all groups but the rate tended to be faster in CNF/CNN compared to HON/CON rats. At P21, there was no significant difference between any of these groups.

Contribution of each Factor

Table 4-2 presents the residual mean T_2 change per day in all the ROIs for all groups. This table enables the effect of the three factors to be identified: fluid supplements (by comparing COF and CON, HOF and HON and CNF and CNN), surgical operation (by comparing CON and CNN, and COF and CNF) and hydrocephalus (by comparing HON and CON, and HOF and COF). A residual T_2 of 0 indicates that the factor has no influence on T_2.

The data summarize the results of the study. In the acute phase, fluid injection causes a global T_2 increase in all regions. Operation causes a sharp global decrease in all ROIS when there is no fluid injected. When fluid is injected, this decrease is reduced in the TH and PC and is reversed in the AC and BG. The effect of hydrocephalus (increased ICP and CSF) is apparent only in the acute phase in the posterior cortex. From P10 and on, fluid supplementation, operation and hydrocephalus do not influence the temporal evolution of T_2.

Table 4-2: Residual mean T_2 change (in ms) due to fluid supplements, surgical operation and hydrocephalus.

	Thalamus		**8-9d**	**9-10d**	**10-14d**	**14-21d**	
EFFECT OF FLUID	C	operated	21.4	-18.2	-0.9	0.8	COF-CON
increases T_2 acutely	HC	operated	31.5	-9.0	2.3	0.1	HOF-HON
	C	non-op	18.6	4.6	-1.7	-0.5	CNF-CNN
EFFECT OF OPERATION	C	no-fluid	-15.6	10.9	0.3	0.5	CON-CNN
decreases T_2 acutely	C	fluid	-12.9	-11.9	1.1	1.7	COF-CNF
EFFECT OF HC	Operated	no-fluid	-6.2	5.1	-2.0	0.8	HON-CON
	Operated	fluid	4.0	14.4	1.3	0.1	HOF-COF

	Posterior cortex		**8-9d**	**9-10d**	**10-14d**	**14-21d**	
EFFECT OF FLUID	C	operated	68.1	-15.9	-0.6	-0.1	COF-CON
increases T_2 acutely	HC	operated	69.9	-8.9	6.2	-1.9	HOF-HON
	C	non-op	27.3	-10.3	2.4	-1.8	CNF-CNN
EFFECT OF OPERATION	C	no-fluid	-56.1	1.7	3.3	1.9	CON-CNN
decreases T_2 acutely	C	fluid	-15.3	-3.9	0.3	3.6	COF-CNF
EFFECT OF HC	Operated	no-fluid	26.5	0.9	-5.9	2.1	HON-CON
increases T_2 acutely	operated	fluid	28.4	7.9	0.9	0.3	HOF-COF

Table 4-2 (continued):

	Anterior cortex		**8-9d**	**9-10d**	**10-14d**	**14-21d**	
EFFECT OF FLUID	C	operated	60.2	-12.6	-1.7	0.0	COF-CON
increases T_2 acutely	HC	operated	50.8	-9.6	3.3	-1.0	HOF-HON
	C	non-op	5.0	10.8	-0.9	-1.6	CNF-CNN
EFFECT OF OPERATION	C	no-fluid	-43.9	8.8	1.0	1.4	CON-CNN
	C	fluid	11.3	-14.6	0.2	3.0	COF-CNF
EFFECT OF HC	operated	no-fluid	5.8	10.2	-7.0	1.3	HON-CON
	operated	fluid	-3.7	13.2	-2.0	0.3	HOF-COF

	Basal ganglia		**8-9d**	**9-10d**	**10-14d**	**14-21d**	
EFFECT OF FLUID	C	operated	38.1	-18.0	-0.7	-0.5	COF-CON
increases T_2 acutely	HC	operated	26.6	-1.1	-2.2	0.1	HOF-HON
	C	non-op	15.7	8.4	-0.3	-1.0	CNF-CNN
EFFECT OF OPERATION	C	no-fluid	-14.4	4.5	-1.0	1.1	CON-CNN
	C	fluid	8.0	-21.9	-1.3	1.6	COF-CNF
EFFECT OF HC	operated	no-fluid	-1.1	-0.2	-1.4	0.8	HON-CON
decreases T_2 acutely	operated	fluid	-12.6	16.6	-3.0	1.4	HOF-COF

Hydration Level

Table 4-3 presents the measurements of protein concentration in the animals separated from their mothers with (FR) or without fluid supplements (CNN). There was never any significant difference between any of the groups. However, there was an increase in protein concentration in the CNF and CNN groups between P10 and P14 (non-significant) and between P14 and P21 (significant for CNF).

Table 4-3: Mean protein (±standard deviation) concentration (in mg per 100 ml of serum) and number of samples used for the calculation (n) in the CNF and CNN group.

Group	**P8**	**P9**	**P10**	**P14**	**P21**
CNF	4.00 (±NA) n = 1	3.75 (±0.07) n = 2	3.72 (±0.10) n = 3	4.13 (±0.32) n = 3	4.87 (±0.15) n = 3
CNN	4.50 (±NA) n = 1	3.75 (±0.35) n = 2	3.83 (±0.55) n = 3	4.30 (±0.20) n = 3	4.87 (±0.15) n = 3

Discussion

Animal Groups

Overall, the shunt procedure was successful except for one animal where it became non-patent after P14. Therefore, all hydrocephalic-shunted animals except that one at P21, were included in the HON group. Rats in the HON and CON group were anesthetized 1 hour and 20 minutes per scanning session and approximately 1 hour and 30 minutes during surgery between the 1st and 2nd scanning session. Animals in the CNF and CNN groups were anesthetized for the same duration as rats in the HON and CON groups. One obvious effect of anesthesia is that rat pups are not able to suckle and therefore become dehydrated. Fluid treatment was intended to prevent dehydration in the anesthetized rats.

We can identify a couple of phenomena occurring in each of the groups. In the CNN rats, repeated anesthesia causes dehydration and a decrease in T_2. In the CNF animals, potential dehydration due to anesthesia is treated with fluid supplements. In the CON rats, animals undergo anesthesia, and therefore dehydration, but also surgical trauma. The operation could cause further dehydration as the animal recovers more slowly than anesthesia alone and therefore is not able to suckle as early as CNF/CNN rats. In addition, loss of fluid could occur when the skull is opened up and the brain is exposed to ambient air. In HON rats, animals undergo the same phenomena as CON animals but in addition, ICP is released and excess CSF is drained out of the brain. Table 4-4 summarizes the potential source of T_2 change in the various groups.

Table 4-4: Potential sources of T_2 changes for each animal group. X indicates a probable influence while ? shows a potential effect on T_2.

Group		**Maturation**	**Anesthesia**		**Surgical trauma**		**Hydrocephalus**		**Fluid supplement**
			Dehydration	Other	Dehydration	Other	ICP release	CSF infiltration	
C		X							
CNF	**Non Operated**	X	X	?					X
CNN		X	X	?					
CON	**Operated**	X	X	?	X	?			
HON		X	X	?	X	?	X	X	
COF	**Operated**	X	X	?	X	?			X
HOF		X	X	?	X	?	X	X	X

Hydration Level

It was not possible to draw blood from all animals at the 3 consecutive time points due to hematomas in the tail vein. Due to the small number of animals ($n \leq 3$), protein concentration measurements did not show significant differences between animals with or without fluid-supplements. Measurement showed the effect of maturation but reached barely the significance level. Therefore, protein concentration measurements are not sensitive enough to detect the small changes caused by repetitive anesthesia and maturation.

Effect of Repetitive Anesthesia and Fluid Supplements

The fluid-replaced group contained only 2 animals and therefore non-significant trends were observed most of the time. Despite the small sample size, results showed that repetitive anesthesia for imaging and simulation of the shunt operation caused a global T_2 decrease that was resolved within 1 to 2 days. In the acute stage, this drop was compensated with fluid supplements as T_2 in CNF rats was never different from C rats, except at P21 in the AC. From these results, it is likely that the T_2 decrease was due to dehydration.

A shortening of T_2 following dehydration is consistent with results of Berenyi *et al.* (1999), where a significant T_2 decrease was found in neonatal rabbits deprived of suckling. However, Berenyi observed a significant 14 ms T_2 decrease after 72 hours of total suckling deprivation. In contrast, the present study reports a surprisingly large 10 to 50 ms T_2 decrease as soon as 24 hours after the first scanning session and approximately 12 hours post-operation or separation. This result was not predicted as the rats were returned to their mothers after the imaging and therefore were not totally deprived of suckling. Consequently dehydration should not have been as severe as in the Berenyi study (1999). In addition, it was expected that the P8 rats would be more mature than 1 to 4-day-old rabbits and would therefore be able to regulate water distribution better. This result points towards investigating T_2 multiexponential behavior of tissues. This would allow discriminating the bound and free pools of water and their behavior and should help explain the mechanisms of these changes.

During 10% body weight dehydration in rats (Nose *et al.*, 1983), water is lost from both intra and extracellular spaces. However, the tendency to lose water in the brain is relatively weak to that in other organs in adult rats. In the present study, dehydration is acute (over 24 hours) and occurs in an immature animal. Therefore, it is expected that extracellular water is primarily affected and that rat pups will have difficulties maintaining homeostasis. This loss of extracellular (i.e. free) water without an increase in intracellular water could cause the reported T_2 reduction. When fluid supplementation is provided to the animals, it goes into the subcutaneous tissue from which it gets into the blood and is distributed to other tissues to restore osmolarity. This phenomenon is very rapid and prevented the T_2 shortening. The compensation of T_2 shortening with fluid supplements supports the hypothesis that repetitive anesthesia causes an acute loss of free (probably extracellular) water.

In some animals fluid supplements caused a T_2 increase. Vadja *et al.* (1999) reported a similar phenomenon when causing hyponatremia (i.e. increased extracellular water in the brain). T_2 increased with increased severity of hyponatremia and the magnitude ranged from 10 to 15 ms. This quantitative change is similar to the effect of fluid supplementation, which reversed the T_2 changes due to repetitive anesthesia.

By P10, there were no differences attributable to fluid supplementation. This suggests that in 2 days, rat pups are able to re-establish homeostasis, probably through slightly increased suckling. The few differences at P21 are probably due to the small sample size and biological heterogeneity as it is unlikely that dehydration causes such long term effects.

Effect of the Surgical Operation

At P8, T_2 tended to be longer in HON and CON rats compared C rats, probably due to biological heterogeneity, but it was shorter at P9. Therefore, the acute ΔT_2 was much greater in operated than in controls and also in non-operated animals. This suggests that surgery causes T_2 shortening additional to that of anesthesia. ΔT_2 in sham-operated animals and non-fluid replaced animals were restricted to cortical areas. It is possible that the T_2 decrease observed in the basal ganglia and thalamus is due mainly to dehydration (similarly to CNN rats + additional dehydration due to surgery). Effects of surgery, other than dehydration, are only prominent in the cortex. This was expected as the shunt is inserted into the anterior and posterior cortical tissue. Dehydration and other effects due to surgery were apparent up to P14, 6 days after operation and were present in all brain regions. Thirteen days post surgery, T_2 had returned to control level. This demonstrates that trauma induces some global changes in the brain that are not attributable to dehydration and which take more than 6 days to resolve. Finally, T_2 shortening following shunt treatment differ from the often-reported T_2 lengthening that follows brain trauma (Thatcher *et al.*, 1998).

Effect of the Release of Intracranial Pressure

Shunt-operated animals demonstrated a significant acute T_2 shortening but that was less prominent than in sham-operated animals. In addition, HON T_2 was significantly longer in the posterior and anterior cortices of CON rats up to P10. Consequently, the release of intracranial pressure reduces the effect of operation and this is more apparent in the cortex. The magnitude of T_2 changes after shunting was comparable to that in not-fluid-replaced animals at both P9 and P10. From P14 and on, there were no differences in sham- and shunt-operated animals.

After shunting, CSF is present around the outside of the brain while the tissue has collapsed (see figure 4-2). It is probable that the CSF infiltrates the brain and particularly the cortex which was stretched pre-shunt. This increase in water content in the tissue would cause a T_2 increase, similar to that observed in hyponatremia in another study (Vadja *et al.*, 1999) and following fluid supplements (see previous paragraph).

Hydrocephalus in the H-Tx rat model causes gray matter edema and disruption of the cortical laminae. This is partially restored one week after shunting (Harris *et al*, 1994; Harris *et al.*, 1996).

In summary, surgery caused an acute and severe decrease in T_2 but this shortening was less pronounced in hydrocephalic animals. The difference between control and hydrocephalic operated animals was more apparent in the cortex, up to 2 days post-operation. Repeated anesthesia caused an acute T_2 change, which was observed throughout the brain but could be compensated by injecting fluid supplements. The magnitude of the T_2 changes due to anesthesia was smaller than those due to surgery.

Table 4-5 presents the absolute effects of each potential source of T_2 change, estimated from the data presented in the results section. Figure 4-5 displays the same results taking into account the timing of each event.

Table 4-5: Semi-quantitative effects on T_2 of the different phenomena for each animal group. – and + indicate a shortening and lengthening of T_2. (na: non-applicable)

Group	**Maturation**	**Anesthesia**		**Surgical trauma**		**Hydrocephalus**		**Fluid supplement**
		Dehydration	Other	Dehydration	Other	ICP release	CSF infiltration	
C	-	na	na	na	na	na	na	na
CNF	-	--	?	na	na	na	na	++
CNN	-	--	?	na	na	na	na	na
CON	-	--	?	-	-	na	na	na
HON	-	--	?	-	-	?	+	na
COF	-	--	?	-	-	na	na	++
HOF	-	--	?	-	-	?	+	++

The lower amplitude T_2 drop following shunt- versus sham-operation needs to be explored. It is anticipated that it is due to CSF infiltration. However, to get a better understanding of these T_2 changes as well as those due to dehydration, it is suggested to perform biexponential T_2 and diffusion measurements. These will give an estimate of the fractions of bound and free water as well as fast and slow-diffusing water. This would allow establishing the mechanisms of water redistribution due to anesthesia, surgery and ICP release.

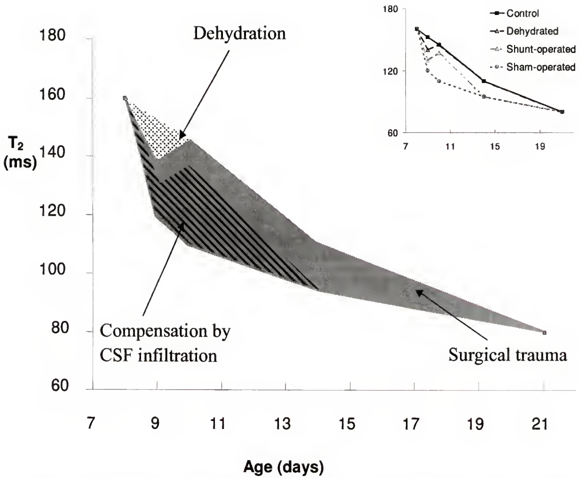

Figure 4-5: Schematic representation of T_2 changes during normal maturation (control), following dehydration, shunt-operation and sham-operation.

In future studies of shunt-treatment, these results should be combined with a measure of function. Traditionally, function has been measured using behavioral tests (Jones *et al.,* 1995) such as the water maze test. However, one can foresee that fMRI techniques presented in chapter 2 will be applicable in the near future. With such methods, the temporal evaluation of function following the operation will be evaluated and correlated with structural T_2 and diffusion measurements.

Conclusion

In conclusion, surgical shunting causes a global brain T_2 shortening up to 5 days post operation. In the acute phase (up to 2 days post-operation), dehydration contributes to the T_2 reduction and can be compensated by subcutaneous injection of fluid. Therefore, future studies should address T_2 changes in shunt- and sham-operated animals with fluid supplementation.

The mechanism of dehydration, surgical trauma and the release of intracranial pressure remains to be elucidated. The current hypothesis is that water in the extracellular space decreases due to dehydration. After surgery, additional dehydration may occur but other phenomena may contribute to the dramatic T_2 decrease. In shunt-treated hydrocephalic rats, it is postulated that CSF infiltrates the extracellular space and therefore compensates partially the effect of dehydration due to repetitive anesthesia. A multicompartmental approach combining both T_2 and ADC measurements will allow testing this hypothesis.

Chapter 5 will present multiexponential T_2 and ADC during brain maturation as the logical extension of chapter 3 and 4 monoexponential studies. This will pave the way for multiexponential studies of shunt treatment.-

CHAPTER 5

T_2 AND BIEXPONENTIAL APPARENT DIFFUSION COEFFICIENT MEASUREMENTS DURING BRAIN MATURATION OF H-TX RATS

Introduction

Chapter 3 showed that T_2 is very sensitive to maturation in the neonatal H-Tx rat brain. However, few differences between normal and hydrocephalic animals were shown. In addition, diffusion measurements were very unreliable. In this chapter, the potential of biexponential measurements to detect the small water content changes of the H-Tx rat model of hydrocephalus was investigated.

Multiexponential T_2 Studies

Whithall *et al.* (1999) reported that 96% of white matter and 78% of gray matter in human brain has multiexponential T_2. In another study, the same group (Whithall *et al.*, 1997) investigated the distribution of T_2 in normal human brain. At most, three peaks were identified: the first with a T_2 of 15 ms, assigned to myelin, the second with T_2s encompassing the 50 to 600 ms range, associated with intra- and extracellular water, and a last population of spins with T_2 greater than 1 s associated with CSF. In all gray matter regions, the 2nd compartment had a mean T_2 between 60 and 80 ms and represented at least 66% of the total spin population. In white matter, the mean T_2 of the second compartment was approximately the same but its volume fraction varied greatly from structure to structure.

Beaulieu *et al.* (1999) used localized proton spectroscopy to investigate multiexponential behavior in myelinated and non-myelinated nerve. They found 3 primary components. The shortest (30-50 ms) one was observed only when myelin was present. These studies imply that multiexponential analysis charaterize true biological water compartments but the behavior of these have to be characterized to understand the relationship between the different water fractions in biological populations.

Berenyi *et al.* (1998) used a biexponential and triexponential approach to investigate the changes in neonatal rabbit brain T_2 following acute dehydration. In normal suckling rabbits, the bound water fraction and its T_2 decreased significantly from 1 to 4 days after birth. The triexponential analysis showed that in the same period of time, the loosely-bound water fraction increased dramatically with no significant change in the other T_2 water populations. Similar T_2 changes were observed 4 days after birth in the suckling-deprived rabbits and could be explained by relative water fraction changes. The brain compensation mechanism in response to dehydration may be that free water is released from its bound state through enzymatic processes, causing an increase in free water fraction. Simultaneously, an increase in macromolecular content may have given rise to the T_2 decrease

Using the same methodology, another group determined total water content and T_2 changes following hyponatremia (water loading) in adult rabbits (Vajda *et al.*, 1999). No water changes measured with the desiccation method were seen after 48 hours of treatment causing hyponatremia. Despite a stable total water content, changes in bound and free water fractions and their T_2s were observed. A transient increase in free water was reported and it was concluded that it could be due to the increase in water in the interstitial space known to occur in hyponatremia.

The results of Vajda and Berenyi are interesting as they show that the biexponential approach may detect changes in water T_2 even though there may not be any change in the total amount of water. However, their analysis is not quite convincing. In both studies, no raw decay curves are shown and it is not evident that the biexponential fit distinguishes 2 distinct relaxation components. Normal mean and SEM of the fast and slow T_2 were 190 (±12) and 180 (±13) ms respectively at birth (Berenyi *et al.*, 1999) and 37 (±20) and 102 (±8) ms respectively in adult rabbits (Vajda *et al.*, 1999). The large SEM shows that amore rigorous analysis including a measure of goodness of fit of the mono- and biexponential models and demonstrating the improvement of the bi- versus the monoexponential analysis.

In summary, monoexponential T_2 measurements are related to total water content and provide, in a first approximation, a good description of tissue MR characteristics. However, most tissues show a multiexponential T_2 decay pattern. Ideally, a continuous T_2 distribution, similar to that measured by Beaulieu *et al.* (1998) or Whithall *et al* (1997) describes a biological system completely. Since this study investigates primarily gray matter and is performed *in vivo* (i.e., time constraint), a biexponential model, one component being the CSF with its T_2 constrained to 900 ms (Ernst *et al.*, 1993) should determine the presence of a significant CSF component in the tissue.

Multiexponential Diffusion Studies

A series of human and animal studies showed that diffusion was not monoexponential in brain tissue when MR signal was collected at large b-values (Assaf

& Cohen, 1998). As a first approximation, a biexponential model was used, representing two water compartments, a slow and a fast diffusing population which would not be in exchange. Such a biexponential diffusion model successfully explained the reduction in ADC following ischemia (Norris *et al.,* 1995; Pfeuffer *et al.*, 1999; Mulkern *et al.*, 1999; Blackband *et al.*, 1997; Buckley *et al.*, 1999). In an attempt to probe brain structure, similar studies have investigated and reported a multiexponential diffusion of NAA and other major intracellular metabolites in both adult (Assaf & Cohen, 1998; Assaf & Cohen, 1999) and neonatal rat brain (Dijkuizen *et al.*, 1999). Although a biexponential fit has successfully described diffusion in the brain, it is not known what physiological compartments, if any, correspond to the fast and slow diffusion fractions.

Niendorf *et al* (1996) measured diffusion in 9-day-old and adult rats. They found a difference in the relative fractions of slow and fast diffusing compartments between neonatal and adult rats. In addition, their respective ADCs were greater in immature brain. Table 5-1 shows the fast and slow diffusing population diffusion coefficients and their relative fractions, as well as the known intra- and extracellular volume fraction.

Table 5-1: Biexponential analysis for *in vivo* adult and 9-day-old rat brain (taken from Niendorf *et al.*, 1996). ADCs are in 10^{-3} $mm^2.s^{-1}$.

	ADC_{fast}	ADC_{slow}	f_{fast}	f_{slow}	$f_{extracellular}$	$f_{intracellular}$
Adult rat	0.82	0.17	0.80	0.17	0.20	0.80
Immature rat (P9)	0.94	0.21	0.90	0.11	0.25-0.30	0.70-0.75

Although these compartments did not correspond to intra- and extracellular volume fractions, they showed a similar relationship with maturation: the rapidly decaying component fraction like the extracellular compartment, was greater in immature rat than in adult rat. In addition, changes in slow and fast diffusing components following ischemia paralleled extracellular space reduction measured by electrical impedance.

Szafer *et al.* (1995) designed an analytical model of diffusion in tissue that predicted multiexponential behavior. Simulations showed that volume fractions and intra- and extracellular volume fractions affected membrane permeability but had little influence on the ADC. Pfeuffer *et al.* (1999) also predicted that relative volume fractions and extracellular tortuosity are the main factors on the measured ADC, while exchange time and intracellular diffusion constant have little influence. Van der Toorn *et al.* (1996) studied tortuosity and extracellular fractions of neonatal rat brain following ischemia. She showed that cell swelling and the associated reduced volume fraction was an important cause of the ADC decrease. This study together with the one of Latour *et al.* (1994) on red blood cells, did not discard the possible influence of extracellular tortuosity on ADC changes. However, water molecules are very mobile compared to the large macromolecules used in iontopheresis measurements, which is the technique employed to measure extracellular tortuosity. Therefore the influence of changes in extracellular tortuosity on the water molecule diffusion pathway is expected to be minor compared to that of extracellular fraction changes.

Biexponential analysis on hippocampal brain slices were carried out following osmotic (hyper- or hypoosmolar environment), ouabain (Buckley *et al.*, 1998) and NMDA (Bui *et al.*, 1999) perturbations, which cause cell swelling or shrinking. Results showed that the fast and slow diffusing coefficients stayed the same while the relative fractions of each component changed in response to these perturbations. Finally perturbations on isolated neurons (Hsu *et al.*, 1996) showed that cell swelling did not change the intracellular coefficient while T_2 increased. All these studies support the hypothesis that only the relative fractions of fast and slow ADCs change while the diffusion coefficients of the compartments stays constant.

Finally, several studies have shown that the biexponential approach is incomplete. Blackband *et al.* (2000) showed that the nucleus of a single cell is not monoexponential. Therefore, it is important to keep in mind that the biexponential approach is first, a simplified model of tissue used as a tool to get a better understanding of complex biological systems and secondly the only feasible multiexponential approach with the scanning time constraints that have to be considered for *in vivo* studies.

Rationale and Aims of Biexponential Studies of H-Tx Brain Maturation

The first aim of this study was to document the normal changes in biexponential T_2 and ADC with maturation. The hypothesis was that the fast diffusing fraction, ADC_{fast} and ADC_{slow}, would decrease with development similarly to the results of Niendorf *et al.* (1996). The second goal was to characterize the status of brain water in slowly developing hydrocephalus. The overall hypothesis was that development would be impaired at all ages compared to normal rats. In the advanced stages, cell swelling and CSF infiltration was expected.

In the next sections, the improved experimental set-up and the protocol for biexponential T_2 and diffusion will be presented. Then, *in vivo* ADC and T_2 mono and biexponential results on P4, P11 and P21 rats will be reported and discussed.

Materials and Methods

Animals

P4, P11 and P21 control (C) and hydrocephalic (HC) H-Tx rats were obtained from the breeding colony maintained at the University of Florida (P4: C, n=7; HC,n=5, P11: C n = 8; HC, n=9; P21: C, n=7; HC, n=8). Rats from 4 litters were examined and 2 of those litters were tentatively examined at all 3 time points. Out of these rats, 3 C died (2 at P4 and 2 at P21), and 2 H died (1 at P11, 1 at P21).

Animals were anesthetized using halothane (P4 and P11: 0.75-1.5%, P21: 1%-1.75%) vaporized in oxygen and nitrous oxide (O_2:N_2O 1:2). Animals were placed in holders and a water heating blanket was laid on top of them (see next sections). No fluid replacement was used as imaging was performed at one week or longer intervals.

Temperature Control

A thermal bath (VWR Scientific, model 1131) with constant flow was set to a constant temperature of 85°C. Water was transported from the bath located behind the magnet passive shielding to the heated blanket at the center of the magnet (4 meters away). The length of the tubing caused a temperature drop of 48°C, heating the water blanket to ~36-37 °C. The blanket consisted of 4 mm diameter tubing placed in a concentric fashion and was molded to provide heating to the whole body of the small rat pups. The efficacy of the water blanket was tested by measuring body surface temperature immediately before and after scanning.

Immobilization Device

Increasing b-values not only increases sensitivity to diffusion but also to motion. In addition, the SNR is greatly reduced with heavy diffusion weighting. For this reason, it was important to restrain the animal as much as possible. Previous experiments showed that problems were due to abdominal breathing motion transmitted to the head and that it was more problematic in the older P21 rats.

Several trials were carried out to investigate the effect of different set-ups on motion. Rats were successively placed prone and supine with different kind of padding. Respiratory gating was not tried since the small body size of rat pups, particularly for P11 and younger ages, prohibits placing both a sensor and a heating blanket on the pup. It was rapidly seen that placing rats supine allowed isolation of the head from body motion. The set-up was improved by using a neck "cradle", a fan-shaped plastic holder. The neck of the holder supported the shoulders down and let the head hang. When the neck cradle was in place the animal was laid into a Plexiglas insert. The Plexiglas insert allowed sliding the rat in and out of the coil without perturbing the placement of the animal in the neck cradle. In addition, a bite bar was inserted into the superior front tooth. With this set up, the body was stretched to ease the breathing but not transmit the thoracic motion. Finally, the Plexiglas insert and the water blanket were taped down to the coil.

Sequence Selection

Biexponential T_2 mapping

Phantom experiments: A series of measurements was performed on gadolinium-doped copper sulfate ($CuSO_4$) saline solutions. Four tubes of 2, 5, 10 and 15 mM concentrations were used. The goal was to determine the fastest and most accurate way to evaluate T_2 using different combinations of RARE factors and number of echo images. T_1 effects were limited by selecting a long TR of 20 s. A variable number of echo-images collected per TR (1-16), echo spacing (7.7 [minimum]- 50 ms) and rare factor (number of lines of k-space per image per TR) (1-16) were investigated. When only 1 echo image was acquired per TR, the sequence was repeated to obtain the desired number of echo images. In that case, the total acquisition time was the number of echo images multiplied by the time to acquire one image. All experiments were conducted on the 4.7T Oxford magnet equipped with the console and small gradient insert from Bruker (Etlingen, Germany). In addition, the small Bruker birdcage coil was used for excitation and detection.

Using Excel (Microsoft, Redmont, Washington, USA), a monoexponential fit was applied to each curve and the T_2 was reported. The gold standard was chosen as the 1 echo image and a RARE factor of 1 (conventional spin-echo sequence).

Rat experiments: From the phantom experiments the choice of 16 echo images with a RARE factor of 2 was selected (ETL = 2 x 16 = 32). An echo spacing (ES) of 14 ms was selected so that TEs up to 427 ms were sampled (effective TEs of the 16 images: 7, 35, 63, 91. 119, 147, 175, 203, 231, 259, 287, 315, 343, 371, 399 and 427 ms). Rat brain T_1 at 4.7T is close to 1800 ms (Akber, 1996). Given that value, a long TR of 10 s (approximately 5 x T_1) was selected to achieve full relaxation of the spins before the next excitation. T_2W images were acquired with the same parameters as DW images. With this protocol, the set of T_2W images was collected in 11 minutes.

Biexponential diffusion mapping

Sequence timing: To obtain a rotationally invariant measure of diffusion, measurements were performed in 3 orthogonal directions using a spin-echo diffusion sequence. In order to reach b-values as high as 4000 $s.mm^{-2}$, it is necessary to increase Δ, δ or G, (see chapter 1). Because it is better to be in the slow exchange regime (no exchange between slow and fast diffusing compartments), the diffusion time, $\tau = \Delta - \delta/3$, was kept as short as possible. This was achieved by orienting diffusion gradients in the XY (read-phase), XZ (read-slice) and YZ (phase-slice) directions as opposed to X, Y and Z directions. This procedure increased the available gradient amplitude by a factor of $\sqrt{2}$. Given this orientation, b-values up to 4050 s.mm^{-2} were achieved with a Δ of14 ms and a δ of 7.5 ms, resulting in a relatively short τ of 11.4 ms. This value is comparable to τ at which slow exchange was observed (Buckley *et al.*, 1999) and much smaller than the 135 ms reported by Pfeuffer *et al.* (1999). To reduce differential T_2-weighting that could occur between compartments, the minimum TE (26.9 ms) was chosen. A 1 s TR was selected. Finally, the frequency encoding direction was chosen to propagate any motion artifact along the right-left direction relative to the head of the animal.

SNR and geometrical parameters: In the biexponential model, four unknowns are estimated: signal intensity without diffusion or T_2 weighting, ADC_{fast}, ADC_{slow} and their relative fractions f_{fast} and $(1-f_{fast})$. Therefore, it is necessary to obtain sufficient data to evaluate these parameters. Eight sets of images with different diffusion weighting were acquired by increasing the gradient amplitude (constant time experiment: G = 20, 50, 85, 130, 180, 220, 255, 290 mT.m^{-1}, or b ~ 25, 132, 363, 555, 1000, 2000, 3000, 4000). DW pre-scan was acquired prior to further measurements. Depending on the degree of motion artifact of that scout, the eight sets of DW images were acquired in one or more (up to 8) acquisitions.

If the relative SNR of brain tissue MR signal is 100 with no diffusion weighting, it drops approximately to 1 at a b-value of 4018 s.mm^{-2}. For this reason, the SNR was increased by reducing spatial resolution. Specifically, the following geometrical parameters were selected: FOV = 6x6 (P4), 7x7 (P11) and 8x8 cm^2 (P21), 128x128 matrix, 3 mm slices with a 0.6 mm gap. For each diffusion direction, imaging took 17 minutes and 4 s, resulting in a total time of 51 minutes to acquire the diffusion trace data. T_2W and DW images were acquired at the same location using the same geometrical parameters.

All imaging data was acquired at 4.7T on an Oxford magnet equipped with a Bruker (Etlingen, Germany) console and a small gradient insert capable of 220 $mT.m^{-1}$ in each direction. A 2.5 cm diameter home-built loop-gap coil was used for excitation and detection at P4. At P11, coils with diameters greater than those used in Chapter 3 were used to accommodate the animal holding device. These were a specifically-built 3.1 mm diameter loop-gap coil and a 3.5 cm diameter non-tunable quadrature volume coil (B.B.). This second coil was also used at P21.

In vivo Data Analysis

Because of the low SNR, a region of interest biexponential fit was performed. The 4 ROIs, thalamus (TH), striatum or basal ganglia (BG), posterior and anterior cortices (PC, AC) described in chapter 3 were used.

Data were examined for motion contamination and SNR. First, raw decay curves were plotted in Excel (Microsoft, Redmond, Washington, USA) and visually inspected as a second check. In addition, a noise-test was incorporated in the fitting algorithm: the program checked recursively if the signal was above the noise level at the largest b-value. If it was not, it did the same check at the next lowest b-value, and so on. With this procedure, the model was fitted only to data points above the noise level. In addition, the program kept track of motion contamination.

From the DW images, the following biexponential analysis parameters were extracted: f_{fast}, the fast diffusing fraction and its ADC, ADC_{fast}, and the slowly diffusing population ADC, ADC_{slow}. In addition, a monoexponential analysis was carried out. When the data had been collected in all 3 diffusion orientations and was of good quality, the trace of the ADC, tr(ADC), was calculated by doing a geometrical average of the 3 ADCs.

A monoexponential T_2 analysis was run on the T_2W data. When the analysis of CSF was run, the fit was performed by discarding the first 2 echo times to exclude the signal increase due to stimulated echoes. Using the average estimate of the CSF T_2, the biexponential fit was constrained to a model with a long T_2 (CSF) and a shorter T_2 (tissue) fraction.

Results

Animal Set-up

Surface body temperature ranged between 32.6 and 37.2°C and 30.8 and 37.8°C immediately before and after the scans. This variability was due to the placement of the water blanket on the animal and to the difficulty of the measurement when the rat pups were waking up. Despite this inaccuracy, all but 3 animals were warm at the end of the 1 hour and a half experiment when taken out of the scanner.

Anesthesia was varied between the animals to take into account physiological variability. With this approach, it was possible to obtain the trace of the diffusion tensor for 8/12, 9/17 and 11/15 animals at P4, P11 and P21 respectively.

Figure 5-1 shows one slice for a P11 control (top row) and a P11 hydrocephalic (bottom row) at the eight b-values used in this study. The image contrast is set to show the background. Little motion artifact is apparent with the new set-up, except at the base of the brain where the trachea and major arteries run. With the choice of frequency direction, the inevitable motion in these structures did not contaminate brain tissue signal. The supine placement of the rat shows as the up-side down appearance of the images.

In three cases, the rats were not significantly anesthetized before being set in the cradle. When that happened, the self-righting reflex of the animal could occur. This was observed as a progressive rotation of the images. When it happened, rats were taken out of the magnet and anesthetized more deeply before being placed again in the scanner and repeating the entire protocol.

Phantom T_2 Measurements

Figure 5-2 shows the effect of increasing the rare factor: at high rare factors, a distinct blurring occurs in the phase encoding direction. Table 5-2 shows the acquisition parameters of the selection of pulse sequences: the number of images acquired in one TR, the rare factor (or number of echoes acquired per image per TR), the echo train length (# of images * rare factor), the range of TEs and the acquisition time for a 128x64 matrix slices. A large number of T_2W images is required to perform a biexponential T_2 analysis and it was decided to acquire 16 images. The study showed that the T_2 of the CuSO4 solutions was very close to the gold standard with a RARE factor of 1 or 2 when 16 images were reconstructed. The rare factor of 2 was chosen as it allowed halving the acquisition time while still minimizing the blurring observed with increased rare factor. The echo spacing is the only parameter that the user can select. A short echo spacing of 14 ms was chosen to minimize a differential T_2-weighting between the 2 lines of k-space of each of the 16 images while sampling the decay curve up to a long TE of 430 ms.

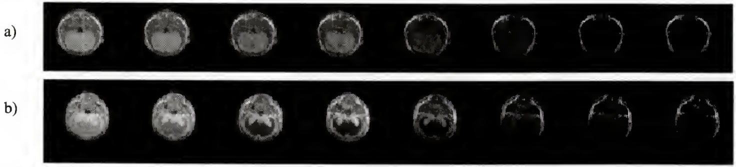

Figure 5-1: Images with increasing diffusion b-weighting on P11 a) control and b) hydrocephalic rats with the improved set-up. The b-values are those used in the study (from 30 up to 4000 s.mm^{-2}).

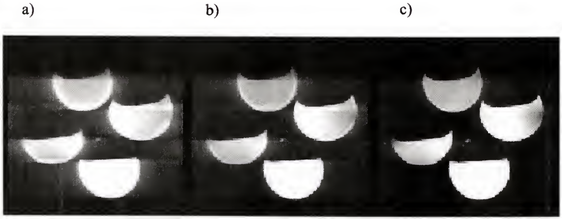

Figure 5-2: Images of $CuSO_4$ tubes acquired with a TE_{eff} of 10 ms and a decreasing rare factor a) RARE = 16, b) RARE = 8, c) RARE =4. The stimulated echo phase artifact decreases with decreasing RARE factor.

Table 5-2: Acquisition protocol (number of images acquired per TR, rare factor or number of lines of k-space acquired for each image, echo train length i.e. product of number of images and the RARE factor) and estimated T_2 (in ms) for the 4 solutions of $CuSO_4$ (TR = 20 s). TE is in ms and the acquisition time in min and seconds.

# img.	**RARE factor**	**ETL**	**Selected TE**	**Range of TEs**	**Acq. time**	**T_2 2 mM**	**T_2 5 mM**	**T_2 10 mM**	**T_2 15 mM**
16	1	16	40	40-640	21:59	225	116	81	63
16	2	32	20	10-610	11:00	219	112	82	61
16	4	64	10	6-605	5:30	218	111	86	65
16	8	128	7.7	3-843	2:47	336	171	132	94
8	1	8	50	50-400	21:44	234	116	78	60
8	2	16	25	12-362	11:00	220	110	75	59
8	4	32	12.5	6-356	5:26	218	109	84	64
1	8	64	7.7	3-395	2:43	213	108	83	64
1	1	1	10-600	10-600	21:30*#TE	222	105	74	70

in vivo T_2 Measurements

Table 5-3 shows the mean and standard deviation for control and hydrocephalic rats at P4, P11 and P21 in all rats. T_2 decreased significantly with age in both animal groups in all ROIs with no significant group differences.

Table 5-3: Mean T_2 (standard deviation) in ms for both groups, in each ROI and at each age.

		P4	**P11**	**P21**
TH	C	146 (15)	130 (6)	81 (3)
	H	146 (11)	137 (14)	88 (8)
PC	C	163 (29)	130 (12)	83 (4)
	H	147 (23)	146 (20)	96 (14)
AC	C	138 (12)	122 (12)	82 (5)
	H	137 (15)	131 (20)	93 (18)
BG	C	142 (13)	131 (9)	84 (6)
	H	168 (10)	144 (17)	96 (9)
CSF		658 (85)	957 (76)	834 (242)

Figure 5-3 shows the signal decay in the 4 ROIs and the CSF of a P11 hydrocephalic rat. The linear plot graph shows the slight signal enhancement at the second echo time due to the stimulated echo formed by the large amplitude CSF signal. The logarithmic plot demonstrates a linear decrease of the signal with TE and shows the monoexponential nature of the T_2 decay. In fact, the constrained biexponential fit of the data was either not possible or gave no physiologically relevant answers.

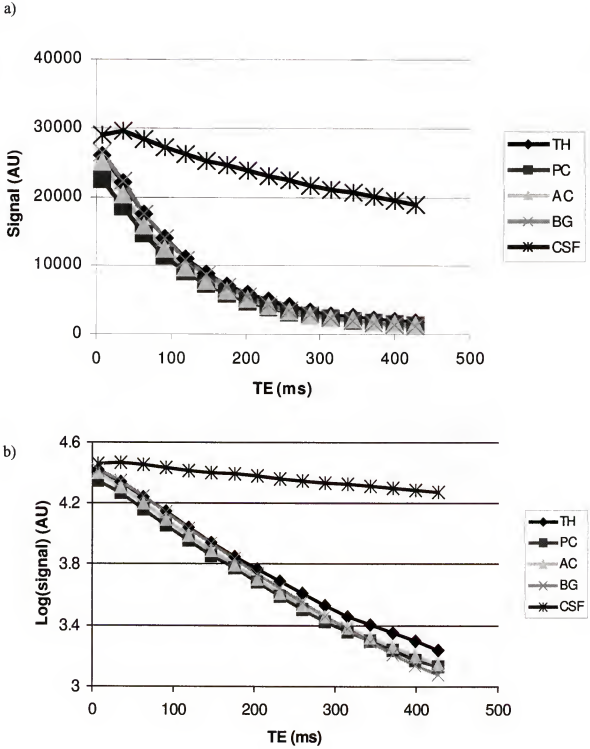

Figure 5-3: MR signal decay (in arbitrary units) as a function of TE on a) a linear and b) a logarithmic plot for a P11 H rat.

Diffusion Measurements

Effect of multiple acquisitions

When diffusion data were acquired in several acquisitions, care was taken to keep all parameters constant (in particular the scanner receiver gain) and only the diffusion weighting was changed. However, decay curves showed irregularities that were correlated with the number of acquisitions (see figure 5-4a). In fact, the scanner software scales the signal intensity by a factor kept in the reconstruction parameter file (RECO_map_slope). Therefore, these factors were recorded and a correction was applied to all individual curves (figure 5-4b).

Monoexponential tr(ADC) measurements

Tables C-1 to C-3 in appendix C display the mean tr(ADC) in the RP, RS, and PS diffusion orientations based on a monoexponential fit on the eight b-values. Tables 5-4 and 5-5 show the regional average tr(ADC) and individual ROI tr(ADC) for both animal groups. Regional changes with age in both control and hydrocephalic animals showed great variability but significant changes were only found when all ROIs were combined.

In both the C and H group, the tr(ADC) decreased significantly from P11 to P21 as well as from P4 to P21 (C group: 0.92, 0.95, and 0.89 10^{-3} $mm^2.s^{-1}$ at P4, P11 and P21 respectively; H group: 0.95, 1.04, and 0.86 10^{-3} $mm^2.s^{-1}$ at P4, P11 and P21 respectively) ($p<0.005$). However, there was a non-significant increase in the tr(ADC) between P4 and P11. There were no significant group differences at any age.

a)

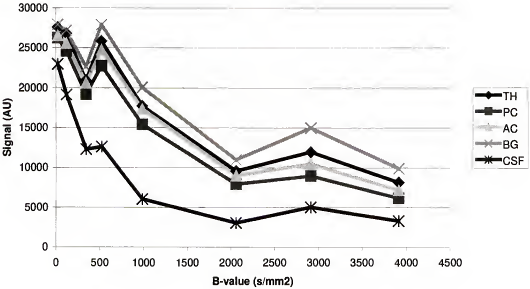

b)

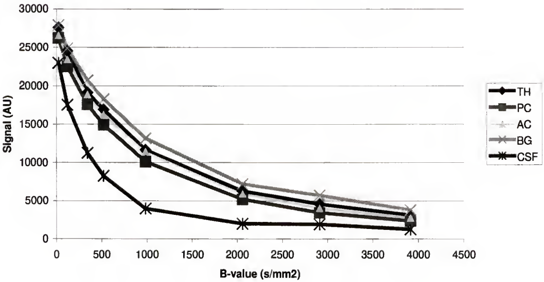

Figure 5- 4: a) Original and b) corrected decay curve of a P21 H rat with increasing diffusion weighting. Data were collected in 4 acquisitions (1st b-value, 2 next b-values, 3 next b-values, 2 last b-values). The raw decay curves show the effect of the automatically changing reconstruction factor.

Table 5-4: Mean (standard deviation) tr(ADC) in 10^{-3} $mm^2.s^{-1}$ in both groups at all ages averaged over all ROIs. The symbols $*$, $^{\#}$, $^{\$}$ indicate a significant different between P4 and P21, P4 and P11 and P11 and P21 respectively.

	P4	**P11**	**P21**
C	0.92 (0.04)	0.95 (0.04)	0.89 (0.04) $^{\$*}$
H	0.95 (0.04)	1.04 (0.07)$^{\#}$	0.86 (0.05)$^{\$*}$

Table 5-5: Mean (standard deviation) tr(ADC) in 10^{-3} $mm^2.s^{-1}$ in both groups at all ages in each ROI.

		P4	**P11**	**P21**
TH	C	0.89 (0.07)	1.04 (0.11)	0.87 (0.08)
	H	0.93 (0.05)	1.06 (0.17)	0.81 (0.09)
PC	C	0.90 (0.09)	1.00 (0.05)	0.93 (0.10)
	H	0.92 (0.09)	1.10 (0.13)	0.95 (0.11)
AC	C	0.96 (0.09)	0.86 (0.05)	0.92 (0.05)
	H	0.95 (0.05)	1.04 (0.16)	0.87 (0.12)
BG	C	0.94 (0.10)	0.92 (0.07)	0.85 (0.06)
	H	0.98 (0.10)	0.96 (0.13)	0.81 (0.09)

Biexponential tr(ADC) measurements

Tables C-4 to C-6 of appendix C present the mean and standard deviation of the biexponential tr(ADC) measurements in the RP, RS, and PS diffusion for all ROIs. Table 5-6 shows the mean and standard deviation of the fast diffusing volume fraction (f_{fast}), its diffusion coefficient tr(ADC_{fast}) and the slow diffusing coefficient, tr(ADC_{slow}) for all ROIs combined and table 5-7 presents the regional value of these quantities. The slow diffusing volume fraction is simply 1-f_{fast}.

In the C group, the volume of the fast-diffusing spins, f_{fast}, decreased significantly from P4 (71%) to P21 (60%) when all ROIs were combined (p=0.022). tr(ADC_{fast}) and tr(ADC_{slow}) did not change significantly with an average value of 1.78 10^{-3} mm^2.s^{-1} and 0.35 10^{-3} mm^2.s^{-1} respectively. In H rats, f_{fast}, and tr(ADC_{slow}) for all ROIs combined increased and decreased significantly between P4 (69%; 0.35 10^{-3} mm^2.s^{-1}) to P21 (55%, - 0.40 10^{-3} mm^2.s^{-1}) and P11 (76%; 0.22 10^{-3} mm^2.s^{-1} - 0.40 10^{-3} mm^2.s^{-1}) to P21 (55%, - 0.40 10^{-3} mm^2.s^{-1}) ($p<0.01$). From P11 to P21, f_{fast} and tr(ADC_{slow}) increased and decreased significantly in all ROIs of H rats ($p<0.001$). f_{fast} and tr(ADC_{slow}) were respectively smaller and greater in C compared to H rats at P11 ($p<0.05$).

Table 5-6: Mean (standard deviation) fast volume fraction f_{fast} in %, tr(ADC_{fast}) and tr(ADC_{slow}) in 10^{-3} mm^2.s^{-1} in both groups at all ages averaged over all ROIs. The symbols *, $^{\#}$, $^{\$}$ indicate a significant different between P4 and P21, P4 and P11 and P11 and P21 respectively, while @ indicate a significant group difference.

	P4			**P11**			**P21**		
	f_{fast}	**ADC_{fast}**	**ADC_{low}**	**f_{fast}**	**ADC_{fast}**	**ADC_{low}**	**f_{fast}**	**ADC_{fast}**	**ADC_{low}**
C	71	1.73	0.29	66	1.77	0.38	60*	1.83	0.41
	(5)	(0.22)	(0.05)	(6)	(0.18)	(0.06)	(7)	(0.26)	(0.06)
H	69	1.74	0.35	$76^{\#@}$	1.73	$0.22^{\#@}$	$55^{\$}$*	1.90	$0.40^{\$}$*
	(4)	(0.12)	(0.05)	(5)	(0.18)	(0.06)	(6)	(0.20)	(0.05)

Table 5-7: Mean (standard deviation) f_{fast} in %, tr(ADC_{fast})and tr(ADC_{slow}) in 10^{-3} $mm^2.s^{-1}$ in both groups at all ages in all ROIs.

		P4			**P11**			**P21**		
		f_{fast}	**ADC_{fast}**	**ADC_{slow}**	**f_{fast}**	**ADC_{fast}**	**ADC_{slow}**	**f_{fast}**	**ADC_{fast}**	**ADC_{slow}**
T H	C	73 (12)	1.62 (0.32)	0.28 (0.11)	63 (10)	2.12 (0.39)	0.46 (0.11)	61 (12)	1.70 (0.32)	0.35 (0.12)
	H	73 (9)	1.50 (0.20)	0.34 (0.10)	83 (8)	1.47 (0.24)	0.34 (0.10)	57 (9)	1.79 (0.24)	0.37 (0.07)
P C	C	68 (7)	1.90 (0.30)	0.30 (0.08)	67 (11)	1.89 (0.40)	0.37 (0.12)	56 (16)	2.12 (0.76)	0.44 (0.14)
	H	68 (9)	1.78 (0.17)	0.33 (0.08)	76 (9)	1.81 (0.30)	0.21 (0.11)	58 (10)	2.06 (0.37)	0.43 (0.09)
A C	C	70 (6)	1.75 (0.28)	0.32 (0.08)	65 (14)	1.53 (0.29)	0.36 (0.13)	60 (15)	1.86 (0.47)	0.42 (0.14)
	H	64 (7)	1.88 (0.25)	0.39 (0.08)	76 (10)	1.68 (0.35)	0.24 (0.11)	53 (13)	1.83 (0.36)	0.44 (0.12)
B G	C	73 (6)	1.66 (0.29)	0.26 (0.09)	68 (12)	1.56 (0.32)	0.35 (0.11)	64 (10)	1.63 (0.45)	0.41 (0.10)
	H	69 (10)	1.81 (0.30)	0.34 (0.14)	69 (13)	1.97 (0.47)	0.28 (0.12)	54 (14)	1.92 (0.57)	0.38 (0.12)

Discussion

Animal Set-up

The temperature control worked well and reduced variability in the diffusion measurements. The animal holder helped reduce breathing motion. However, given the long imaging protocol, a large percentage of the data was still not usable. A better restraint system and a modified acquisition protocol should be implemented to provide the additional stability needed for this kind of study. A solution may lie in performing respiratory gating or intubating and ventilating the rat pups. Another approach consists in using a less motion-sensitive pulse sequence, using for example a projection reconstruction strategy (Lauterbur, 1973).

A fast-imaging strategy could also reduce motion artifact. For example, spin-echo DW-EPI single or multi-shot, or U-FLARE (Norris *et al.*, 1992). The line scan technique developed by Finsterbusch and Frahm (1999) is fast and insensitive to tissue susceptibility differences which occur in all echo-planar techniques. Because of the reduced SNR concomitant with fast acquisitions, several acquisitions would need to be averaged. Finally, when directional information is not desired, single-shot diffusion trace imaging can be used (Mori & Van Zijl, 1996). This sequence acquires data weighted by the equivalent of three orthogonal diffusion weighted gradients, therefore reducing the acquisition time by a factor of 3.

T_2 Measurements

Age-related changes were similar to that reported in chapter 3. Namely, T_2 decreased significantly with age in all ROIs although the effect was greater in the cortical areas. No significant differences were observed between control and hydrocephalic animals.

The constrained biexponential T_2 analysis was unable to pick out a CSF component in any ROI. In fact, the logarithmic plot of the signal decay with TE was a straight line, unlike the plot of the signal decay versus b-value. The monoexponential model appears to provide an adequate fit for the brain ROIs of the neonatal H-Tx rat.

The non-multiexponential nature of the T_2 curves is inconsistent with the findings of Berenyi *et al.* (1998). However, as introduced in the review section of this chapter, Berenyi did not demonstrate convincingly the adequacy of their fitting models to describe brain tissue. In addition, during the first 48 hours of life, the authors report that the long and short T_2 components were "nearly identical". This questions the rationale for a multiexponential T_2 analysis.

Data for this study were obtained from the cortex, basal ganglia and thalamus of rat pups, which are primarily gray matter. In Whithall *et al.* (1997), a short T_2 component was detected whose amplitude was representative of the myelin content, which was not expected to be present in the studied ROIs. A long T_2 component assigned to CSF was being modeled in the constrained biexponential fit. The maximum echo time of 430 ms made it possible to sample the slowly decaying CSF component. However, this two-compartment model is not adequate for neonatal rat brain tissue. This indicates that CSF infiltration and subsequent enlargement of the extracellular space, are unlikely, masked by maturation changes, or too subtle to be detected with the current T_2 protocol.

If indeed CSF infiltration does not occur, this supports the findings of Shoesmith *et al.* (2000) who found impaired extracellular fluid marker movement in gray matter of immature hydrocephalic rats, demonstrating compression rather than infiltration of the tissue. Given the appearance of brain tissue in the acute post-shunt phase (see chapter 4), it is possible that ventricular expansion compresses the brain, forcing water out of the tissue.

Monoexponential tr(ADC) Measurements

Control data

Monoexponential measurements gave ADCs of 0.95 10^{-3} $mm^2.s^{-1}$ at P11, which are in agreement with reported literature values of 0.92 10^{-3} $mm^2.s^{-1}$ in 8-day-old rats (van der Toorn *et al.*, 1996, Dijkuizen *et al.*, 1999). Data showed great variability. This was due to biological heterogeneity and motion artifact that had been reduced but not eliminated. In addition, the large slice thickness of 3 mm compared to the size of the brain may have lead to volume averaging adding to the hetereogeneity of the measurements.

The tr(ADC) was seen to decrease overall with age, as expected from the observations of Baratti *et al.* (1999), Sakuma *et al.* (1991), and others. This decrease with age is attributed to the reduction of extracellular space with maturation and the formation of macromolecules. The data showed no change from P4 to P11 and this is consistent with the constant tr(ADC) over the first 2 weeks of life that was reported in white matter of kittens (Baratti *et al.*, 1999). This phase may represent a regional maturation difference that should be investigated using more time points.

Hydrocephalic data

In hydrocephalic rats, there was an increase in tr(ADC)s between P4 and P11. Between P11 and P21, there was a rapid decrease of the tr(ADC) whose magnitude was greater than that in control rats. Around P13, the skull plates start fusing. From then on, intracranial pressure rises quickly and this could lead to an accelerated reduction of the extracellular space which would cause a rapid decrease in tr(ADC). If this were to be true, it would support the hypothesis of Shoesmith *et al.* (2000), that extracellular space is reduced.

Most diffusion studies in hydrocephalus have observed a diffusion increase in the periventricular white matter but not in gray matter (Braun *et al.*, 1998, Ulug *et al.*, 1999, Chun *et al.*, 2000, Chang *et al.*, 2000). This is consistent with the results that there is no difference in tr(ADC) between control and hydrocephalic in the studied brain regions.

Biexponential tr(ADC) Measurements

Control data

The fast volume fractions, f_{fast}, (66% at P11 and 60% at P21) is different from Niendorf in vivo published values (90% in P9 rat brain, (Niendorf *et al.*, 1996)) but similar to Buckley's (53% in rat brain slices, (Buckley *et al.*, 1998)). However the ADC_{slow} (0.38 10^{-3} $mm^2.s^{-1}$ at P11 and 0.41 10^{-3} $mm^2.s^{-1}$ at P21) is also in agreement with Niendorf's results (0.21 10^{-3} $mm^2.s^{-1}$ in P9 rat) but not with those of Buckley *et al.* (0.086 10^{-3} $mm^2.s^{-1}$in brain slices, 1998). The ADC_{fast} was found to be 1.77 10^{-3} $mm^2.s^{-1}$ at P11 and 1.83 10^{-3} $mm^2.s^{-1}$ at P21, which is elevated compared to the value of 0.94 10^{-3} $mm^2.s^{-1}$ (Niendorf *et al.*, 1996) and 1.01 10^{-3} $mm^2.s^{-1}$ in brain slices (Buckley *et al.*, 1998). The present data showed a lot of variability that was related to motion. Motion will cause an artificial signal loss. At low b-values, this will be reflected by a greater fast diffusion coefficient.

In controls, there was a significant decrease of the fast volume fraction with age. However, no significant changes in the $tr(ADC_{slow})$ or $tr(ADC_{fast})$ were observed. Therefore, the overall tr(ADC) age-related changes are explained by a redistribution of the fast and slow diffusing components, rather than a change in their diffusion characteristics. The extracellular space volume fractions are 34% at P4, 26% at P11 and 22% at P21 (Lehmenkuhler *et al.*, 1993). These fractions are quite different to the 71%, 66% and 60% fast diffusing volume fractions obtained in this study. As discussed in the introduction, 1) the diffusion time and 2) the echo time will affect the measurements. 1) The diffusion time was short (11 ms) in this study and the assumption of no exchange between fast and slow diffusing compartments is probably valid. 2) TE was 26.8 ms. Although it is relatively short, differential attenuation of the signal in the two compartments could occur. Buckley *et al.* (1999) found similar discrepancies with a TE of 30 ms and a short diffusion time. However, if the fast and the slow components are assigned to the intra- and extracellular space, then one needs to take into account the longer extracellular space T_2. The cytoplasmic T_2 of a Aplysia neuron is 29 ms (Schoenieger *et al.*, 1994) and Buckley found that it was short enough to explain the discrepancy between the fast-diffusing volume fraction and extracellular volume fraction. Both T_2 and extracellular volume fraction are higher in the neonatal brain and a detailed analysis of the influence of intra- and extracellular T_2 should be carried out to investigate this issue.

Niendorf *et al.* (1996) saw that not only the fast diffusing fraction but also both diffusion constants were reduced with maturation between 9 days and adulthood. The difference between these results and those presented here may be due to 1) the different ages, 2) regions of interest investigated and 3) experimental technique. 1)The brain still undergoes changes after 3 weeks, which was the maximum age studied here. It is conceivable that the extracellular space reduction causes the reduction in the fast volume fraction and that it is the main effect up to 21 days after birth. Changes in the diffusing properties of both components may occur simultaneously but may not be of a magnitude observable on a 2-week scale. 2) Niendorf investigated cortical tissue that may contained white matter (myelin). If this is the case, the formation of myelin is expected to reduce the diffusion coefficient as the relatively impermeable sheath impairs water motion.3) Finally, experimental conditions, namely the long echo time and long diffusion time used by Niendorf, added some T_2 weighting and partial exchange between the compartments that would lead to a biased estimate of ADC_{fast} and ADC_{slow}.

If indeed ADC_{fast} and ADC_{slow} do not change with maturation, this would support the results of Hsu *et al.* (1996), Buckley *et al.* (1998) and Bui *et al.* (1999). These studies found that following several types of perturbations, the diffusion characteristics of the tissue do not change but rather the relative sizes of the compartments vary, causing an increase or decrease of the monoexponential tr(ADC).

Hydrocephalic data

In hydrocephalus, the fast volume fraction and the ADC_{slow} increased and decreased respectively from P4 to P11, while opposite trends were observed in the control group. The increased f_{fast} at P11 indicates enlarged extracellular space (where diffusion is more free). This may indicate CSF infiltration in the early stage of hydrocephalus. This contradicts the negative finding of a CSF compartment in the biexponential T_2 study, unless this effect was masked by maturation changes. After P11, there is a dramatic reduction in the fast volume fraction. This supports the idea that following skull fixation (around P13), the intracranial pressure forces water out of the brain and the extracellular space is reduced (Shoesmith *et al.*, 2000).

The biexponential analysis shows that the apparent constant monoexponential tr(ADC) in hydrocephalic rats between P4 and P11 is the result of two phenomena with opposite effects on the monoexponential tr(ADC). In fact, the f_{fast} increases and ADC_{slow} decreases. Therefore, biexponential analysis proved useful in the explanation of the underlying biological phenomena.

Conclusion

T_2 changes with maturation were apparent in both control and hydrocephalic rats but no differences were observed between the two groups.

tr(ADC) was measured in individual ROIs and showed a reduction with age that was significant when all ROIs were combined. The biexponential study suggested that the reduction in tr(ADC) was caused by a reduction in the fast diffusing volume fraction without changes in the diffusion characteristics of the two compartments. Similar results were observed in hydrocephalus, but the time course of diffusion was different from normal maturation both between P4 to P11 and between P11 to P21. It is suggested that the skull fixation causes a change in the diffusion properties of the tissue of hydrocephalic rat brains.

Future studies should focus on further reducing the motion using either fast-imaging or projection reconstruction techniques. In addition, a single-scan diffusion trace sequence should be employed. The subsequent gain in time could be used to increase the SNR by increasing the number of averages, and improving the spatial resolution, therefore limiting partial volume averaging as much as possible. To confirm the hypothesis that fast and slow diffusing volume fractions can be assigned to intra- and extracellular space, measurements using iontophoresis techniques could be performed.

With a new protocol, it is suggested that temporal changes in the diffusion properties of hydrocephalic brain tissue should be studied at more time points. The increased temporal resolution will allow characterization of the impact of skull fixation on the MR properties of the tissue. Corkill *et al.* (2000) suggested that an elevated ADC in the periventricular white matter was correlated with poor shunt-surgery outcome. Therefore, a study with more time points might allow identification of a critical time at which irreversible brain damage occurs.

CHAPTER 6
SUMMARY AND CONCLUSIONS

Summary

The mysteries of the brain still have to be uncovered. Magnetic resonance imaging is now able to not only capture a gross anatomic picture of the brain but also collect measurements that can be related to the cellular architecture and functionality of the tissue. This dissertation was aimed at developing and advancing these MRI techniques through human and animal studies to establish a link between gross anatomy, microscopic structure and function.

Auditory Functional MRI

In chapter 2, the feasibility of auditory fMRI was demonstrated in humans. Using advanced post-processing techniques, the variability of auditory fMRI measurements was reduced and fMRI signal changes were shown to increase with increasing sound intensity of speech.

Auditory fMRI has made tremendous advances over the last few years and it is now possible to use specifically designed imaging sequences so that the acoustic noise does not interfere with stimulus-induced activation. In addition, single-event auditory experiments are replacing block-design paradigms. These advances should improve the robustness of the auditory fMRI signal changes and will hopefully make fMRI a reliable tool for the study of auditory and speech processing deficits in individual patients.

Brain Maturation

In chapters 3 and 5, changes in the mono- and biexponential tr(ADC) and T_2 were characterized during brain maturation of normal and hydrocephalic H-Tx rats between 4 and 21 days after birth. For the first time, *in vivo* T_2 was measured at ages as early as 4 days after birth. Results showed a dramatic T_2 decrease with age. Cortical regions showed the greatest T_2 shortening, indicating the immaturity of that tissue at birth. Few differences between control and hydrocephalic rat T_2 were seen, indicating the absence of vasogenic edema in the gray matter.

The ADC decreased significantly with maturation in both control and hydrocephalic rats between 4 and 21 days after birth. A two-compartment model, consisting of slow and fast diffusing water populations, was applied to identify the source of these changes. This approach showed that the monoexponential ADC decrease was due to a reduction in the size of the fast diffusing water compartment while the diffusion coefficients of both compartments remained unchanged. Extracellular space is known to reduce significantly with brain maturation and the results of this study support the hypothesis that the fast diffusing water compartment is tightly related to the extracellular space.

In hydrocephalic rats, the monoexponential ADC decreased by 21 days after birth but the data showed a transient increase at 11 days. This increase is postulated to arise from an enlargement of the extracellular space combined with a decrease in the intracellular ADC. This suggests a complicated pattern of microscopic changes that could be related to the transition from an expanding to a fixed skull, or the onset of increased intracranial pressure in hydrocephalic animals.

In the future, the imaging protocol could be changed to a sequence less sensitive to motion. In addition, the biexponential model needs to be validated. Further inquiries could for example link the biexponential MR parameters to iontopheresis measurements of extracellular space. Finally, an *in vitro* approach to maturation changes could consist of performing the same measurements in perfused brain slices obtained from normal and hydrocephalic H-Tx rats.

Monitoring of Shunt Treatment

Chapter 4 described brain T_2 changes before and after shunt-treatment. It was shown that dehydration due to the repetitive anesthesia caused a transient global brain T_2 decrease that was compensated with fluid supplementation. Surgery also caused a T_2 shortening that was resolved 13 days after the operation. In hydrocephalic rats, shunting reduced significantly the ventricular size and cortical tissue expanded rapidly in the brain cavity. The T_2 decrease was of smaller magnitude in hydrocephalic compared to control rats and correlated with the acute reduction in ventricular size. This effect lasted up to 6 days post-surgery and was predominant in the cortex, which suggested CSF infiltration in the tissue as the intracranial pressure was released.

Future studies will aim at measuring the temporal changes of the trace of the apparent diffusion coefficient following shunt-surgery. With the biexponential approach presented in chapter 5, it will be possible to monitor the dynamics of extra- and intracellular space. As ventricular size does not predict effective brain damage prevention, surgical efficacy should be estimated using behavioral measures. In addition, intracranial pressure could be monitored. Both ICP and surgery efficacy data should be correlated with the MR parameters. In the longer term, it could be feasible to evaluate brain function using fMRI methodology, which would simplify greatly the current assessment of motor and cognitive impairment of the animals.

Conclusion

New MRI based quantitative techniques are now available to investigate the function and structure of brain tissue. It is hoped that the results presented in this dissertation will form the basis of future studies that will assess microscopic structural changes and functional information, not only in the normal or hydrocephalic brain but also in a host of abnormal neurological pathologies. And ultimately, quantitative MRI measurements will likely be combined with physiological information obtained from MR spectroscopy.

More investigations are needed to understand the origins of MR signal changes and particular emphasis has to be given to the validation of MR parameters versus known biological or physiological events. However, when these relationships are established, the availability of MR scanners in the clinic will allow direct application of these methods to the diagnosis and treatment of neurological diseases and disorders.

APPENDIX A
REGIONAL T_2 MATURATION CHANGES

Table A-1: Mean (±SEM) T_2 (in ms) in the PC of control and hydrocephalic rats.

	P4	**P11**	**P21**
C	210 (±8)	141 (±6)	81 (±3)
H	187 (±10)	163 (±13)	79 (±4)

Table A-2: Mean (±SEM) T_2 (in ms) in the AC of control and hydrocephalic rats.

	P4	**P11**	**P21**
C	200 (±6)	139 (±7)	75 (±2)
H	201 (±12)	152 (±12)	74 (±3)

Table A-3: Mean (±SEM) T_2 (in ms) in the BG of control and hydrocephalic rats.

	P4	**P11**	**P21**
C	168 (±5)	131 (±3)	77 (±1)
H	156 (±6)	152 (±5)	75 (±1)

Table A-4: Mean (±SEM) T_2 (in ms) in the TH of control and hydrocephalic rats.

	P4	**P11**	**P21**
C	162 (±5)	129 (±4)	77 (±2)
H	143 (±4)	129 (±4)	73 (±2)

APPENDIX B
MEAN T_2 AND RATE OF CHANGE OF T_2 FOLLOWING SHUNT OR SHAM OPERATION WITH OR WITHOUT FLUID SUPPLEMENTATION

Table B-1: Mean (±SEM) T_2 (in ms) in the PC of the 6 groups studied and the extrapolated control values.

	P8	**P9**	**P10**	**P14**	**P21**
Control	171 (±8)	161 (±8)	151 (±8)	123 (±3)	81 (±2)
CON	198 (±10)	118 (±2)	113 (±4)	97 (±1)	78 (±4)
HON	195 (±11)	140 (±5)	136 (±6)	96 (±1)	84 (±8)
CNF	154 (±13)	168 (±0)	151 (±12)	134 (±11)	76 (±3)
CNN	180 (±2)	152 (±13)	150 (±16)	121 (±1)	75 (±0)
COF	147 (±6)	135 (±8)	117 (±7)	98 (±5)	82 (NA)
HOF	124 (±1)	140 (±6)	128 (±11)	101 (NA)	101 (NA)

Table B-2: Mean (±SEM) T_2 (in ms) in the AC of the 6 groups studied and the extrapolated control values.

	P8	**P9**	**P10**	**P14**	**P21**
Control	167 (±6)	158 (±6)	149 (±6)	120 (±4)	75 (±1)
CON	169 (±4)	113 (±2)	106 (±3)	91 (±2)	74 (±3)
HON	183 (±9)	131 (±7)	135 (±9)	91 (±1)	79 (±5)
CNF	154 (±6)	147 (±3)	146 (±6)	123 (±12)	76 (±4)
CNN	145 (±5)	137 (±8)	123 (±10)	106 (±3)	70 (±1)
COF	132 (±2)	136 (±9)	114 (±8)	92 (±8)	80 (NA)
HOF	131 (±7)	132 (±12)	125 (±9)	95 (NA)	79 (NA)

Table B-3: Mean (±SEM) T_2 (in ms) in the TH of the 6 groups studied and the extrapolated control values.

	P8	**P9**	**P10**	**P14**	**P21**
Control	142 (±4)	138 (±4)	134 (±4)	114 (±2)	77 (±2)
CON	152 (±8)	123 (±2)	124 (±3)	104 (±3)	73 (±1)
HON	159 (±4)	126 (±2)	131 (±4)	104 (±2)	79 (±2)
CNF	150 (±9)	150 (±3)	145 (±11)	120 (±10)	72 (±2)
CNN	153 (±12)	136 (±1)	129 (±1)	113 (±5)	69 (±2)
COF	148 (±6)	140 (±7)	123 (±6)	100 (±9)	79 (NA)
HOF	141 (±2)	138 (±9)	134 (±9)	109 (NA)	82 (NA)

Table B-4: Mean (±SEM) T_2 (in ms) in the BG of the 6 groups studied and the extrapolated control values.

	P8	**P9**	**P10**	**P14**	**P21**
Control	148 (±5)	142 (±5)	137 (±5)	115 (±2)	76 (±1)
CON	156 (±13)	126 (±5)	124 (±2)	97 (±3)	74 (±1)
HON	167 (±5)	136 (±4)	133 (±4)	101 (±2)	80 (±5)
CNF	138 (±3)	135 (±2)	139 (±8)	119 (±11)	75 (±5)
CNN	140 (±3)	127 (±2)	127 (±2)	108 (±2)	72 (±2)
COF	142 (±6)	151 (±7)	128 (±11)	99 (±13)	81 (NA)
HOF	147 (±2)	142 (±13)	138 (±10)	99 (NA)	82 (NA)

Table B-5: Mean (±SEM) rate of T_2 change (in ms per day) in the PC of the 6 groups studied and the extrapolated control values.

	P8-P9	**P9-P10**	**P10-P14**	**P14-P21**
Control	-9.6 (±3.3)	-9.6 (±3.3)	-6.6 (±1.9)	-6.6 (±1.9)
CON	-79.9 (±12.2)	-4.7 (±4.6)	-4.0 (±0.9)	-2.8 (±0.5)
HON	-53.4 (±10.9)	-3.8 (±7.6)	-10.0 (±1.7)	-0.7 (±1.4)
CNF	3.4 (±15.2)	-16.8 (±8.1)	-4.9 (±2.8)	-6.4 (±2.5)
CNN	-23.8 (±7.2)	-6.4 (±5.2)	-7.3 (±1.7)	-4.6 (±2.3)
COF	-11.9 (±7.6)	-20.6 (±21.0)	-4.6 (±3.0)	-2.9 (NA)
HOF	16.5 (±5.5)	-12.8 (±9.1)	-3.8 (NA)	-2.6 (NA)

Table B-6: Mean (±SEM) rate of T_2 change (in ms per day) in the AC of the 6 groups studied and the extrapolated control values.

	P8-P9	**P9-P10**	**P10-P14**	**P14-P21**
Control	-8.9 (±2.9)	-8.9 (±2.9)	-7.7 (±1.9)	-7.7 (±1.9)
CON	-56.0 (±3.9)	-6.9 (±1.9)	-3.8 (±1.0)	-2.6 (±0.8)
HON	-50.2 (±15.1)	3.2 (±6.3)	-10.8 (±2.5)	-1.3 (±0.9)
CNF	-7.1 (±5.7)	-4.9 (±7.1)	-5.7 (±2.2)	-5.6 (±1.6)
CNN	-12.1 (±4.2)	-15.8 (±7.6)	-4.8 (±1.5)	-4.0 (±1.3)
COF	-4.2 (±7.6)	-19.5 (±24.7)	-5.5 (±3.9)	-2.6 (NA)
HOF	0.6 (±5.1)	-6.3 (±16.3)	-7.5 (NA)	-2.3 (NA)

Table B-7: Mean (±SEM) rate of T_2 change (in ms per day) in the TH of the 6 groups studied and the extrapolated control values.

	P8-P9	**P9-P10**	**P10-P14**	**P14-P21**
Control	-4.2 (±1.2)	-4.2 (±1.2)	-4.5 (±0.9)	-4.5 (±0.9)
CON	-28.8 (±8.1)	0.2 (±3.8)	-4.8 (±1.3)	-4.8 (±0.4)
HON	-35.0 (±6.0)	5.4 (±4.7)	-6.8 (±1.6)	-4.0 (±0.8)
CNF	5.5 (±7.5)	-6.1 (±8.4)	-6.8 (±1.7)	-5.7 (±1.6)
CNN	-13.1 (±13.4)	-10.7 (±3.2)	-5.1 (±1.7)	-5.2 (±1.6)
COF	-7.4 (±2.2)	-18.0 (±20.9)	-5.8 (±3.9)	-4.0 (NA)
HOF	-3.5 (±7.9)	-3.6 (±16.8)	-4.5 (NA)	-3.9 (NA)

Table B-8: Mean (±SEM) rate of T_2 change (in ms per day) in the BG of the 6 groups studied and the extrapolated control values.

	P8-P9	**P9-P10**	**P10-P14**	**P14-P21**
Control	-5.2 (±1.4)	-5.2 (±1.4)	-5.6 (±1.2)	-5.6 (±1.2)
CON	-29.7 (±14.2)	-2.7 (±4.3)	-6.6 (±0.6)	-3.3 (±0.6)
HON	-30.8 (±7.4)	-3.0 (±3.2)	-8.0 (±1.4)	-2.5 (±1.2)
CNF	0.3 (±5.2)	1.2 (±6.6)	-5.9 (±1.6)	-5.5 (±1.3)
CNN	-15.3 (±9.8)	-7.2 (±6.9)	-5.6 (±1.3)	-4.4 (±0.9)
COF	8.4 (±1.7)	-20.7 (±25.2)	-7.3 (±6.0)	-3.9 (NA)
HOF	-4.2 (±14.4)	-4.1 (±16.0)	-10.3 (NA)	-2.4 (NA)

APPENDIX C
REGIONAL MATURATION CHANGES OF MONO- AND BIEXPONENTIAL ADC IN CONTROL AND HYDROCEPHALIC RATS

Monoexponential ADC Measurements

Table C-1: Mean (standard deviation) ADC in 10^{-3} $mm^2.s^{-1}$ in both groups at all ages and in all ROIs in the read-phase diffusion orientation.

RP		**P4**	**P11**	**P21**
TH	C	0.96 (±0.09)	0.98 (±0.19)	0.85 (±0.14)
	H	0.90 (±0.09)	1.03 (±0.21)	0.77 (±0.16)
PC	C	0.95 (±0.13)	0.90 (±0.13)	0.90 (±0.14)
	H	0.79 (±0.12)	0.86 (±0.19)	0.81 (±0.14)
AC	C	1.00 (±0.10)	0.82 (±0.08)	0.84 (±0.03)
	H	0.91 (±0.05)	0.98 (±0.14)	0.75 (±0.14)
BG	C	00.96 (±0.11)	0.85 (±0.09)	0.75 (±0.05)
	H	0.86 (±0.21)	0.90 (±0.27)	0.70 (±0.11)
CSF		2.36 (±0.24)	2.77 (±0.35)	2.75 (±0.60)

Table C-2: Mean (standard deviation) ADC in 10^{-3} $mm^2.s^{-1}$ in both groups at all ages and in all ROIs in the read-slice diffusion orientation.

RS		**P4**	**P11**	**P21**
TH	C	0.83 (±0.12)	1.06 (±0.23)	0.87 (±0.15)
	H	0.93 (±0.10)	1.10 (±0.18)	0.81 (±0.15)
PC	C	0.82 (±0.11)	1.06 (±0.07)	0.94 (±0.17)
	H	0.97 (±0.25)	1.22 (±0.26)	1.07 (±0.23)
AC	C	0.86 (±0.16)	0.88 (±0.10)	0.91 (±0.11)
	H	0.94 (±0.17)	1.11 (±0.35)	0.99 (±0.32)
BG	C	0.84 (±0.17)	0.97 (±0.16)	0.84 (±0.11)
	H	1.00 (±0.18)	0.97 (±0.09)	0.86 (±0.18)
CSF		2.70 (±0.20)	2.60 (±0.56)	2.63 (±0.54)

Table C-3: Mean (standard deviation) ADC in 10^{-3} $mm^2.s^{-1}$ in both groups at all ages and in all ROIs in the phase-slice diffusion orientation.

PS		**P4**	**P11**	**P21**
TH	C	0.88 (±0.15)	1.07 (±0.15)	0.90 (±0.15)
	H	0.95 (±0.03)	1.04 (±0.42)	0.86 (±0.14)
PC	C	0.93 (±0.20)	1.04 (±0.04)	0.95 (±0.20)
	H	1.01 (±0.01)	1.23 (±0.22)	0.97 (±0.19)
AC	C	1.02 (±0.19)	0.89 (±0.08)	0.98 (±0.11)
	H	1.00 (±0.04)	1.03 (±0.28)	0.88 (±0.09)
BG	C	1.01 (±0.21)	0.93 (±0.09)	0.96 (±0.12)
	H	1.09 (±0.14)	1.02 (±0.28)	0.86 (±0.15)
CSF		2.97 (±0.41)	2.77 (±0.15)	2.52 (±0.58)

Biexponential ADC Measurements

Table C-4: Mean (standard deviation) f_{fast} in %, ADC_{fast} and ADC_{slow} in 10^{-3} $mm^2.s^{-1}$ in both groups at all ages and in all ROIs in the read-phase diffusion orientation.

RP		**P4**			**P11**			**P21**		
TH	C	80 (9)	1.53 (0.28)	0.19 (0.14)	75 (20)	1.74 (0.77)	0.33 (0.21)	60 (20)	1.70 (0.31)	0.33 (0.21)
	H	73 (17)	1.42 (0.21)	0.33 (0.21)	76 (19)	1.65 (0.47)	0.27 (0.24)	50 (12)	1.86 (0.59)	0.43 (0.09)
PC	C	77 (9)	1.63 (0.39)	0.19 (0.10)	73 (21)	1.59 (0.75)	0.29 (0.22)	62 (21)	1.57 (0.32)	0.37 (0.23)
	H	67 (16)	1.51 (0.12)	0.31 (0.12)	72 (14)	1.72 (0.49)	0.26 (0.15)	56 (19)	1.78 (0.51)	0.42 (0.10)
AC	C	68 (6)	1.98 (0.55)	0.37 (0.08)	67 (16)	1.44 (0.33)	0.37 (0.13)	62 (23)	1.67 (0.73)	0.38 (0.21)
	H	65 (13)	1.83 (0.41)	0.34 (0.14)	78 (12)	1.39 (0.21)	0.28 (0.17)	43 (17)	2.01 (0.53)	0.48 (0.13)
BG	C	69 (5)	1.95 (0.57)	0.31 (0.08)	70 (16)	1.41 (0.44)	0.34 (0.15)	64 (22)	1.53 (0.76)	0.30 (0.21)
	H	59 (20)	2.02 (0.66)	0.43 (0.25)	72 (22)	1.88 (0.98)	0.26 (0.25)	41 (10)	2.11 (0.64)	0.44 (0.10)

Table C-5: Mean (standard deviation) f_{fast} in %, ADC_{fast} and ADC_{slow} in 10^{-3} $mm^2.s^{-1}$ both groups, at all ages and in all ROIs in the read-slice diffusion orientation.

RS		**P4**			**P11**			**P21**		
TH	C	78	1.34	0.22	61	2.34	0.47	63	1.69	0.35
		(27)	(0.64)	(0.26)	(21)	(0.57)	(0.22)	(13)	(0.55)	(0.15)
	H	81	1.49	0.25	76	1.65	0.27	69	1.47	0.27
		(11)	(0.46)	(0.15)	(19)	(0.47)	(0.24)	(13)	(0.21)	(0.15)
PC	C	79	1.51	0.22	78	1.72	0.24	59	2.02	0.46
		(16)	(0.37)	(0.20)	(21)	(0.65)	(0.25)	(18)	(1.39)	(0.18)
	H	71	1.86	0.28	72	1.72	0.26	72	1.71	0.29
		(16)	(0.28)	(0.15)	(14)	(0.49)	(0.15)	(24)	(0.80)	(0.25)
AC	C	74	1.52	0.28	68	1.58	0.31	61	1.62	0.47
		(14))	(0.44)	(0.23)	(22)	(0.44)	(0.25)	(10)	(0.30)	(0.08)
	H	63	1.90	0.42	78	1.39	0.28	71	1.40	0.30
		(10)	(0.52)	(0.11)	(12)	(0.21)	(0.17)	(19)	(0.30)	(0.26)
BG	C	79	1.54	0.21	66	1.70	0.36	64	1.53	0.30
		(16)	(0.51)	(0.24)	(25)	(0.58)	(0.22)	(22)	(0.76)	(0.21)
	H	73	1.82	0.32	72	1.88	0.26	67	1.44	0.28
		(17)	(0.51)	(0.26)	(22)	(0.98)	(0.25)	(19)	(0.33)	(0.19)

Table C-6: Mean (standard deviation) f_{fast} in %, tr(ADC_{fast}) and tr(ADC_{slow}) in 10^{-3} $mm^2.s^{-1}$ in both groups at all ages and in all ROIs in the phase-slice diffusion orientation.

PS		**P4**			**P11**			**P21**		
TH	C	60 (20)	2.00 (0.66)	0.43 (0.15)	54 (12)	2.28 (0.67)	0.59 (0.12)	60 (25)	1.71 (0.72)	0.38 (0.23)
	H	65 (17)	1.59 (0.31)	0.43 (0.18)	88 (11)	1.32 (0.37)	0.05 (0.02)	51 (21)	2.03 (0.33)	0.41 (0.12)
PC	C	49 (8)	2.55 (0.72)	0.49 (0.12)	51 (14)	2.35 (0.69)	0.57 (0.12)	48 (38)	2.78 (1.76)	0.49 (0.30)
	H	65 (13)	1.97 (0.41)	0.40 (0.17)	82 (19)	1.84 (0.33)	0.14 (0.20)	45 (7)	2.70 (0.59)	0.58 (0.09)
AC	C	68 (7)	1.76 (0.47)	0.32 (0.05)	61 (32)	1.57 (0.67)	0.39 (0.29)	56 (34)	2.29 (1.17)	0.42 (0.36)
	H	65 (14)	1.90 (0.38)	0.40 (0.17)	85 (13)	1.40 (0.12)	0.11 (0.07)	46 (28)	2.09 (0.90)	0.54 (0.21)
BG	C	72 (7)	1.49 (0.39)	0.26 (0.05)	68 (21)	1.56 (0.61)	0.35 (0.17)	53 (34)	2.29 (1.17)	0.42 (0.36)
	H	76 (17)	1.60 (0.37)	0.28 (0.24)	77 (28)	1.74 (0.47)	0.15 (0.21)	55 (37)	2.21 (1.56)	0.41 (0.29)

APPENDIX D
LIST OF PUBLICATIONS

This appendix presents the scientific communications published from the work carried out during these doctoral graduate studies. The list is organized in chronological order.

Papers

C.M. Mohr, W.M. King, A.J. Freeman, R.W. Briggs, C.M. Leonard, Influence of Stimulus Intensity on the Activation of Auditory Cortex Investigated with fMRI, *the Journal of the Acoustical Society of America (JASA)*, vol. 105 (5), p. 2738-2745, May 1999.

B. Crosson, J.R. Sadek, J.A. Bobholz, D. Gockay, C.M. Mohr, C.M. Leonard, L. Maron, E.J. Auerbach, S. Browd, R.W. Briggs, Activity in the Paracingulate and Cingulate Sulci during word Generation: an fMRI study of functional anatomy *Cerebral Cortex*, vol. 9 (4), p. 307-316, June 1999.

D. Gökçay, C.M. Mohr, B. Crosson, C.M. Leonard, J.A. Bobholtz, LOFA: Software for Individualized Localization of Functional MRI Activity, *Neuroimage*, vol. 10, p. 749-755, December 1999.

C.M. Leonard. M. Eckert, L.J. Lombardino, T. Oakland, J. Kranzler, C. Crandell, C.M. Mohr, W.M. King, A.J. Freeman, Anatomical Risk Factors for Dyslexia, *Cerebral Cortex*, *in preparation*, 2000.

B. Crosson, J.R. Sadek, L. Maron, D. Gökçay, C.M. Mohr, E.J. Auerbach, A.J. Freeman, R.W. Briggs, Relative shift from medial to lateral frontal cortex, during externally versus internally guided word generation, *in preparation*, 2000.

C.M. Mohr, J.D. Bui, S.J. Blackband, H.C. Jones, MRI volumetric and T_2 Measurements of Brain Maturation in Hydrocephalic H-Tx Rats, *in preparation*, 2000.

C M. Mohr, B.J. Carter, S.J. Blackband, H.C. Jones, Shunt Efficiency studied by T_2 Changes in Neonatal Hydrocephalic Rats, *in preparation*, 2000.

Abstracts

A. J. Freeman, C.M. Mohr, W.K. King, R.W. Briggs, C.M. Leonard, Effect of Stimulus Intensity on the Volume of Activated Cortex in Auditory fMRI, *V^{th} ISMRM Scientific Meeting*, Vancouver, Canada, April 1997

W. King, C. Crandell, A. Freeman, J. Kranzler, C. Leonard, L. Lombardino, C.M. Mohr, T. Oakland, Neurobiological foundations of reading disabilities, Part 2, Auditory processing in college students with and without developmental dyslexia, *Society for the Scientific Study of Reading* Annual Meeting, April 1998.

C. M. Leonard, W. K. King, L. J. Lombardino, A. J. Freeman, C.M. Mohr, J. Kranzler,T. Oakland, Neurobiological foundations of reading disabilities, Part 3. College students with compensated dyslexia do not have anomalous asymmetry of the planum, *Society for the Scientific Study of Reading,* Annual Meeting, April 1998.

D. Gokcay, C.M. Mohr, B. Crosson, C.M. Leonard, J.A. Bobholtz , Software for ROI analysis of fMRI images based on Anatomic Landmarks, *Human Brain Mapping,* Annual Conference, Montreal, Canada, June 1998.

C.M. Mohr, J.D. Bui, H.C. Jones, S.J. Blackband, MR Quantitation of T_2 and ADC at three stages of neonatal rat hydrocephalus, *VIIth ISMRM annual meeting*, Philadelphia, USA, May 1999.

C.M. Mohr, J.D. Bui, H.C. Jones, S.J. Blackband, MR Quantitation of T_2 and ADC at three stages of neonatal rat hydrocephalus, *Society For Neuroscience* annual meeting, Miami, USA, November 1999.

C.M. Mohr, B.J. Carter,J.S. Depelteau, S.J. Blackband, H.C. Jones, T_2 Changes following shunt-treatment in hydrocephalic H-Tx rats, *VIIIth ISMRM annual meeting*, Denver, USA, April 2000.

C.M. Mohr, B.J. Carter,J.S. Depelteau, S.J. Blackband, H.C. Jones, T_2 Changes following shunt-treatment in hydrocephalic H-Tx rats, A*nnual Meeting on Spina Bifida and Hydrocephalus*, Atlanta, USA, June 2000

LIST OF REFERENCES

RM Abrams, AA Hutchison, KJ Gerhardt (1989). Effect of high-intensity sound on local cerebral glucose utilization in fetal sheep. *Brain Res Dev Brain Res*, **48**, 1-10.

SF Akber (1996). NMR relaxation data of water proton in normal tissues. *Physiol Chem Phys Med NMR*, **28**, 205-238.

Y Assaf, Y Cohen (1998). Non-mono-exponential attenuation of water and N-acetyl aspartate signals due to diffusion in brain tissue. *J Magn Reson*, **131**, 69-85.

Y Assaf, Y Cohen (1999). Structural information in neuronal tissue as revealed by q-space diffusion NMR spectroscopy of metabolites in bovine optic nerve. *NMR Biomed*, **12**, 335-344.

PA Bandettini, A Jesmanowicz, EC Wong, JS Hyde (1993). Processing strategies for time-course data sets in functional MRI of the human brain. *Magn Reson Me.*, **30**, 161-173.

C Baratti, AS Barnett, C Pierpaoli (1999). Comparative MR imaging study of brain maturation in kittens with T_1, T_2, and the trace of the diffusion tensor. *Radiology*, **210**, 133-142.

D Barnes, BE Du, WI McDonald, G Johnson, PS Tofts (1986). The NMR signal decay characteristics of cerebral oedema. *Acta Radiol Suppl*, **369**, 503-506.

C Beaulieu, FR Fenrich, PS Allen (1998). Multicomponent water proton transverse relaxation and T2-discriminated water diffusion in myelinated and nonmyelinated nerve. *Magn Reson.Im*, **16**, 1201-1210.

JW Belliveau, KK Kwong, DN Kennedy, JR Baker, CE Stern, R Benson, et al (1992). Magnetic resonance imaging mapping of brain function. Human visual cortex. *Invest Radiol*, **27 Suppl 2**, S59-S65

H Benveniste, LW Hedlund, GA Johnson (1992). Mechanism of detection of acute cerebral ischemia in rats by diffusion-weighted magnetic resonance microscopy. *Stroke*, **23**, 746-754.

E Berenyi, I Repa, P Bogner, T Doczi, E Sulyok (1998). Water content and proton magnetic resonance relaxation times of the brain in newborn rabbits. *Pediatr Res*, **43**, 421-425.

JR Binder, JA Frost, TA Hammeke, SM Rao, RW Cox (1996). Function of the left planum temporale in auditory and linguistic processing. *Brain*, **119**, 1239-1247.

JR Binder, SM Rao, TA Hammeke, JA Frost, PA Bandettini, JS Hyde (1994). Effects of stimulus rate on signal response during functional magnetic resonance imaging of auditory cortex. *Brain Res Cogn Brain Res*, **2**, 31-38.

N Bloembergen, EM Purcell, RV Pound (1948). Relaxation effects in nuclear magnetic resonance absorption. *Phys Rev*, **73**, 679-712.

S Bluml, JG McComb, BD Ross (1997). Differentiation between cortical atrophy and hydrocephalus using 1H MRS. *Magn Res Med*, **37**, 395-403.

CA Boillat, HC Jones, GL Kaiser, NG Harris (1997). Ultrastructural changes in the deep cortical pyramidal cells of infant rats with inherited hydrocephalus and the effect of shunt treatment. *Exp Neurol*, **147**, 377-388.

PA Bottomley, CJ Hardy, RE Argersiner, G Allen-Moore (1987). A review of 1H nuclear magnetic resonance relaxation in pathology: are T1 and T2 diagnostic? *Med Phys*, **14**, 1-37.

M Brant-Zawadzki, HM Bartowski, DA Ortehndahl, LH Pitts, NM Hylton (1984). NMR in experimental cerebral edema: T1 and T2 calculations. *AJNR Am J Neuroradiol*, **5**, 125-129.

KP Braun, RA De Graaf, WP Vandertop, RH Goosken, KA Tulleken, K Nicolay (1998). In vivo 1H MR spectroscopic imaging and diffusion weighted MRI in experimental hydrocephalus. *Magn Reson Med*, **40**, 832-839.

KP Braun, RM Dijkhuizen, RA De Graaf, K Nicolay, WP Vandertop, RH Gooskens, et al (1997). Cerebral ischemia and white matter edema in experimental hydrocephalus: a combined in vivo MRI and MRS study. *Brain Res*, **757**, 295-298.

KP Braun, P Van Eijsden, WP Vandertop, RA De Graaf, RH Gooskens, KA Tulleken, et al (1999). Cerebral metabolism in experimental hydrocephalus: an in vivo 1H and 31P magnetic resonance spectroscopy study. *J Neurosurg*, **91**, 660-668.

GG Briggs, RD Nebes (1975). Patterns of hand preference in a student population. *Cortex*, **11**, 230-238.

DL Buckley, JD Bui, MI Phillips, T Zelles, BA Inglis, HD Plant, et al (1999). The effect of ouabain on water diffusion in the rat hippocampal slice measured by high resolution NMR imaging. *Magn Reson Med*, **41**, 137-142.

JD Bui, DL Buckley, MI Phillips, SJ Blackband, (1999). Nuclear magnetic resonance imaging measurements of water diffusion in the perfused hippocampal slice during N-methyl-D-aspartate-induced excitotoxicity. *Neuroscience*, **93**, 487-490

SJ Blackband, SC Grant, DL Buckley, S Gibbs, AG Webb, TH Mareci (2000). Multiple component water diffusion observed in isolated neurons. *Proceedings of the VIIIth ISMRM meeting*, Denver, USA.

RB Buxton, EC Wong, LR Frank (1998). Dynamics of blood flow and oxygenation changes during brain activation: the balloon model. *Magn Reson Med*, **39**, 855-864.

Y Chang, YS Kim, MJ Kim, SK Hwang, RS Han, DS Kang (2000). The sequential proton MRS and diffusion studies of kaolin-induced hydrocephalic cat brain. *Proceedings of the VIIIth ISMRM meeting* , Denver, USA.

PD Chumas, JM Drake, MR Del Bigio, M Da Silva, UI Tuor (1994). Anaerobic glycolysis preceding white-matter destruction in experimental neonatal hydrocephalus. *J Neurosurg*, **80**, 491-501.

T Chun, CG Filippi, N Relkin, RD Zimmerman, AM Ulug (2000). Diffusion changes in normal pressure hydrocephalus. *Proceedings of the VIIIth ISMRM meeting*, Denver, USA.

RT Constable, AW Anderson, J Zhong, JC Gore (1992). Factors influencing contrast in fast spin-echo MR imaging. *Magn Reson Imaging*, **10**, 497-511.

RG Corkill., MR Garnett, AM Blamire, B Rajagopalan, TAD Cadoux-Hudson., P Styles (2000).. Pre-operative diffusion imaging and proton spectroscopy of the periventricular white matter can distinguish between good and poor outcome from surgery in normal pressure hydrocephalus. *Proceedings of the VIIIth ISMRM meeting* , Denver, USA.

RW Cox (1996). AFNI: software for analysis and visualization of functional magnetic resonance neuroimages. *Comput Biomed Res*, **29**, 162-173.

MC Da Silva, JM Drake, C Lemaire, A Cross, UI Tuor (1994). High-energy phosphate metabolism in a neonatal model of hydrocephalus before and after shunting. *J Neurosurg*, **81**, 544-553.

MC Da Silva, S Michowicz, JM Drake, PC Chumas, UI Tuor (1995). Reduced local cerebral blood flow in periventricular white matter in experimental neonatal hydrocephalus-restoration with CSF shunting. *J Cereb Blood Flow Metab*, **15**, 1057-1065.

MR Del Bigio, MC Da Silva, JM Drake, UI Tuor (1994). Acute and chronic cerebral white matter damage in neonatal hydrocephalus. *Can J Neurol Sci*, **21**, 299-305.

EA DeYoe, PA Bandettini, J Neitz, D Miller, P Winans (1994). Functional magnetic resonance imaging (FMRI). of the human brain. *J Neurosci Methods*, **54**, 171-187.

T Ernst, R Kreis, BD Ross (1993). Absolute quantitation of water and metabolites in the human brain. I. Compartments and water. *J Mag Res Series B*, **102**, 1-8.

A Dhankhar, BE Wexler, RK Fulbright, T Halwest, AM Blamire, RG Shulman (1997). Functional magnetic resonance imaging assessment of the human brain auditory cortex response to increasing word presentation rates. *J Neurophysiol*, **77**, 476-483.

RM Dijkuizen, RA De Graff, KA Tulleken, K Nicolay (1999). Changes in the diffusion of water and intracellular metabolites after excitotoxic injury and global ischemia in neonatal rat brain. *J Cereb Blood Flow Metab*, **19**, 341-349.

T Ebisu, S Naruse, Y Horikawa, S Ueda, C Tanaka, M Uto, et al (1993). Discrimination between different types of white matter edema with diffusion-weighted MR imaging. *J Magn Reson Imaging*, **3**, 863-868.

WA Edelstein, JM Hutchinson, G Johnson, T Redpath (1980). Spin warp NMR imaging and applications to human whole-body imaging. *Phys Med Biol*, **25**, 751-756.

U Felderhoff-Mueser, MA Rutherford, WV Squier, P Cox, EF Maalouf, SJ Counsell, et al (1999). Relationship between MR imaging and histopathologic findings of the brain in extremely sick preterm infants. *AJNR Am J Neuroradiol*, **20**, 1349-1357.

J Finsterbusch, J Frahm (1999)., Diffusion-weighted single-shot line scan imaging of the human brain. *Magn Res Med*, **42**, 772-778.

JC Ford, DB Hackney, E Lavi, M Phillips, U Patel (1998). Dependence of apparent diffusion coefficients on axonal spacing, membrane permeability, and diffusion time in spinal cord white matter. *J Magn Reson Imaging*, **8**, 775-782.

Y Fu, K Tanaka, S Nishimura (1990). Evaluation of brain edema using magnetic resonance proton relaxation times. *Adv Neurol* , **52**, 165-176.

CR Genovese, DC Noll, WF Eddy (1997). Estimating test-retest reliability in functional MR Imaging I: statistical methodology. *Magn Reson Med*, **38**, 497-507.

P Gideon, C Thomsen, F Gjerris, PC Sorensen, O Henriksen (1994). Increased self-diffusion of brain water in hydrocephalus measured by MR imaging. *Acta Radiol*, **35**, 514-519.

BG Goodyear, R Menon (1997). The effect of absolute luminous intensity on BOLD fMRI response in primary visual cortex. *Proceedings of the Vth ISMRM meeting*, **1**, Vancouver, Canda.

A Haase (1990). Snapshot FLASH MRI. Applications to T1, T2, and chemical-shift imaging. *Magn Reson Med*, **13**, 77-89.

A Haase, D Matthaei, R Bartkowski, E Duhmke, D Leibfritz (1989). Inversion recovery snapshot FLASH MR imaging. *J Comput Assist Tomogr*, **13**, 1036-1040.

PC Hanlow, RJ Gooskens, M Van Schooneveld, CA Tulleken, MS Van Der Knapp, JA Faber, et al (1997). The effect of intracranial pressure on myelination and the relationship with neurodevelopment in infantile hydrocephalus. *Dev Med Child Neurol*, **39**, 286-291.

NG Harris, HC Jones, S Patel (1994). Ventricle shunting in young H-Tx rats with inherited congenital hydrocephalus: a quantitative histological study of cortical grey matter. *Childs Nerv Syst* , **10**, 293-301.

NG Harris, HC Jones, SCR Williams (1992). MR imaging for measurements of ventricles and cerebral cortex in postnatalrats (H-TX strain). with progressive inherited hydrocephalus. *Exp Neurol*, **118**, 1-6.

NG Harris, JP McAllister, JM Conaughty, HC Jones (1996). The effect of inherited hydrocephalus and shunt treatment on cortical pyramidal cell dendrites in the infant H-Tx rat. *Exp Neurol*, **141**, 269-279.

NG Harris, HD Plant, RW Briggs, HC Jones (1996). Metabolite changes in the cerebral cortex of treated and untreated infant hydrocephalic rats studied using in vitro 31P-NMR spectroscopy. *J Neurochem*, **67**, 2030-2038.

NG Harris, HD Plant, BA Inglis, RW Briggs, HC Jones (1997). Neurochemical changes in the cerebral cortex of treated and untreated hydrocephalic rat pups quantified with in vitro 1H-NMR spectroscopy. *J Neurochem*, **68**, 305-312.

J Hennig, A Nauerth, H Friedburg (1986). RARE imaging: a fast imaging method for clinical MR. *Magn Reson Med* , **3**, 823-833.

BA Holland, DK Haas, D Norman, M Brant-Zawadzki, TH Newton (1986). MRI of normal brain maturation. *AJNR Am J Neuroradiol*, **7**, 201-208.

Y Horikawa, S Naruse, C Tanaka, K Hirakawa, H Nishikawa (1986). Proton NMR relaxation times in ischemic brain edema. *Stroke*, **17**, 1149-1152.

EW Hsu, NR Aiken, SJ Blackband (1996). Nuclear magnetic resonance microscopy of single neurons under hypotonic perturbation. *Am J Physiol*, **271**, C1895-C1900

EW Hsu, NR Aiken, SJ Blackband (1997). A study of diffusion isotropy in single neurons by using NMR microscopy. *Magn Reson Med,* **37**, 624-627.

CE Johanson, DJ Reed, DM Woodbury (1976). Developmental studies of the compartmentalization of water and electrolytes in the choroid plexus of the neonatal rat brain. *Brain Res*, **116**, 35-48.

HC Jones, RW Andersohn (1998). Progressive changes in cortical water and electrolyte content at three stages of rat infantile hydrocephalus and the effect of shunt treatment. *Exp Neurol*, **154**, 126-136.

HC Jones, RM Bucknall, NG Harris (1991). The cerebral cortex in congenital hydrocephalus in the H-Tx rat: a quantitative light microscopy study. *Acta Neuropathol (Berl)*, **82**, 217-224.

HC Jones, NG Harris, RW Briggs, SCR Williams (1995a). Shunt treatment at two postnatal ages in hydrocephalic H-Tx rats quantified using MR imaging. *Exp Neurol*, **133**, 144-152.

HC Jones, KM Rivera, NG Harris (1995b). Learning deficits in congenitally hydrocephalic rats and prevention by early shunt treatment. *Child Nerv Syst*, **11**, 655-660.

HC Jones, NG Harris, JR Rocca, RW Andersohn (1997). Progressive changes in cortical metabolites at three stages of infantile hydrocephalus studied by in vitro NMR spectroscopy. *J Neurotrauma*, **14**, 587-602.

HC Jones, HK Richards, RM Bucknall, JD Pickard (1993). Local cerebral blood flow in rats with congenital hydrocephalus. *J Cereb Blood Flow Metab*, **13**, 531-534.

SG Kim, W Richter, K Ugurbil (1997). Limitations of temporal resolution in functional MRI. *Magn Reson Med*, **37**, 631-636.

DF Kohn, N Chinookoswong, SM Chou (1981). A new model of congenital hydrocephalus in the rat. *Acta Neuropathol (Berl.)*., **54**, 211-218.

LL Latour, K Svoboda, PP Mitra, CH Sotak (1994). Time-dependent diffusion of water in a biological model system. *Proc Natl Acad Sci U.S.A.*, **91**, 1229-1233.

PC Lauterbur (1973). Image formation by induced local interactions: examples employing nuclear magnetic resonance. *Nature,* **242**, 190-191.

D Le Bihan, J Delannoy, RL Levin (1989). Temperature mapping with MR imaging of molecular diffusion: application to hyperthermia. *Radiology*, **171**, 853-857.

A Lehmenkuhler, E Sykova, J Svoboda, K Zilles, C Nicholson (1993). Extracellular space parameters in the rat neocortex and subcortical white matter during postnatal development determined by diffusion analysis. *Neuroscience*, **55**, 339-351.

CM Leonard, C Puranik, JM Kuldau, LJ Lombardino (1998). Normal variation in the frequency and location of human auditory cortex landmarks. Heschl's gyrus: where is it? *Cereb Cortex.*, **8**, 397-406.

GP Liney, AJ Knowles, DJ Manton, LW Turnbull, SJ Blackband, AHorsman (1996). Comparison of conventional single echo and multi-echo sequences with a fast spin-echo sequence for quantitative T2 mapping: application to the prostate. *J Magn Reson Im*, **6**, 603-607.

I Loubinoux, A Volk, J Borredon, S Guirimand, B Tiffon, J Seylaz, et al (1997). The effects of a butanediol treatment on acute focal cerebral ischemia assessed by quantitative diffusion and T2 MR imaging. *Magn Reson Im*, **15**, 1045-1055.

EM Massicotte, MR Del Bigio (1999). Human arachnoid villi response to subarachnoid hemorrhage: possible relationship to chronic hydrocephalus. *J Neurosurg*, **91**, 80-84.

S Majumbar, JC Gore (1987). Effects of selective pulses on the measurement of T2 and apparent diffusion in multiecho MRI. *Magn Reson Med*, **4**, 120-128.

S Majumbar, SC Orphanoudakis, A Gmitro, M O'Donnell, JC Gore (1986). Errors in the measurements of T_2 using multiple-echo MRI techniques. II. Effects of static field inhomogeneity. *Magn Reson Med*, **3**, 562-574.

P Mansfield (1984). Real-time echo-planar imaging by NMR. *Br Med Bull*, **40**, 187-190.

DW Marquardt (1963). An algorithm for least-square estimations of non-linear parameters. *J Soc Ind. Appl Math.* **11**, 431-441.

M Masumura (1987). Proton relaxation time of immature brain. I. Measurement of proton relaxation time (T1 and T2). in immature rat brain by 1H-NMR spectroscopy. *Childs Nerv Syst*, **3**, 2-5.

JC Mazziotta, ME Phelps, RE Carson, DE Kuhl (1982). Tomographic mapping of human cerebral metabolism: auditory stimulation, *Neurol*, **32**, 921-937.

SJ Millen, VM Haughton, Z Yetkin (1995). Functional magnetic resonance imaging of the central auditory pathway following speech and pure-tone stimuli. *Laryngoscope*, **105**, 1305-1310.

E Miot-Noirault, L Barantin, S Akoka, A Le Pape (1997). T2 relaxation time as a marker of brain myelination: experimental MR study in two neonatal animal models. *J Neurosci Methods*, **72**, 5-14.

JA Miyan, MI Khan, Y Kawarada, T Sugiyama, CM Bannister (1998). Cell death in the brain of the HTx rat. *Eur J Pediatr Surg*, **8 Suppl 1**, 43-48.

ME Moseley, Y Cohen, J Mintorovitch, L Chileuitt, H Shimizu, J Kucharczyk, et al (1990). Early detection of regional cerebral ischemia in cats: comparison of diffusion- and T_2-weighted MRI and spectroscopy. *Magn Reson Med*, **14**, 330-346.

S Mori, PC van Zijl (1996). Diffusion weighting by the trace of the diffusion tensor within a single scan. *Magn Reson Med*, **33**, 41-52.

E Moser, C Teichtmeister, M. Diemling (1996). Reproducibility and postprocessing of gradient-echo functional MRI to improve localization of brain activity in the human visual cortex, *Magn Reson Im*, **14**, 567-579.

RV Mulkern, H Gudbjartsson, CF Westin, HP Zengingonul, W Gartner, CR Guttman, et al (1999). Multi-component apparent diffusion coefficients in human brain. *NMR Biomed*, **12**, 51-62.

T Niendorf, RM Dijkhuizen, DG Norris, C van Lookeren, K Nikolay (1996). Biexponential diffusion attenuation in various states of the brain tissue: implications for diffusion-weighted imaging. *Magn Reson Med*, **36**, 847-857.

JJ Neil (1997). Measurement of water motion (apparent diffusion). in biological systems. *Concepts Magn Res*, **9**, 385-401.

DC Noll, JD Cohen, CH Meyer, W Schneider (1995). Spiral K-space MR imaging of cortical activation. *J Magn Reson Imaging*, **5**, 49-56.

DC Noll, CR Genovese, LE Nystrom, AL Vazquez, SD Forman, WF Eddy, JD Cohen (1997). Estimating test-retest reliability in functional MR Imaging II: application to motor and cognitive studies *Magn. Reson. Med.*, **38**, 508-517.

DG Norris, P Bornert, T Reese, D Leibfritz (1992). On the application of ultra-fast RARE experiments. *Magn Reson. Med*, **27**, 142-164.

DG Norris, T Niendorf (1995). Interpretation of DW-NMR data: dependence on experimental conditions. *NMR Biomed*, **8**, 280-288.

H Nose, T Morimoto, K. Ogura (1983). Distribution of water losses among fluid compartments of tissues under theral dehydration in the rat. *Jpn J Physiol*, **33**, 1019-1029.

S Ogawa, TM Lee, AR Kay, DW Tank (1990). Brain magnetic resonance imaging with contrast dependent on blood oxygenation. *Proc Natl Acad Sci USA*, **87**, 9868-9872.

S Ogawa, DW Tank, R Menon, JM Ellerman, SG Kim, H Merklel (1992). Intrinsic signal changes accompanying sensory stimulation: functional brain mapping with magnetic resonance imaging. *Proc Natl Acad Sci USA*, **89**, 5951-5955.

S Ogawa, RS Menon, DW Tank, SG Kim, H Merkle, JM Ellermann, *et al.* (1993). Functional brain mapping by blood oxygenation level-dependent contrast magnetic resonance imaging. A comparison of signal characteristics with a biophysical model. *Biophys J*, **64**, 803-812.

L Pauling (1977). Magnetic properties and structure of oxyhemoglobin. *Proc Natl Acad Sci USA*, **74**, 2612-2613.

VB Penhune, RJ Zatorre, JD MacDonald, AC Evans (1996). Interhemispheric anatomical differences in human primary auditory cortex: probabilistic mapping and volume measurement from magnetic resonance scans. *Cereb Cortex*, **6**, 661-672.

SE Petersen, PT Fox, MI Posner. M Mintun, ME Raichle (1988). Positron emission tomographic studies of the cortical anatomy of single-word processing. *Nature*, **114**, 585-589.

J PfeufferJ, SW Provencher, R Gruetter (1999). Water diffusion in rat brain in vivo as detected at very large b values is multicompartmental. *MAGMA.*, **8**, 98-108.

C Pierpaoli, P Jezzard, PJ Basser, A Barnett, G Di Chiro (1996). Diffusion tensor MR imaging of the human brain. *Radiology*, **201**, 637-648.

CS Poon, RM Henkelman (1992). Practical T_2 quantitation for clinical applications. *J Magn Reson Imaging*, **2**, 541-553.

C Price, R Wise, S Ramsay, K Friston, D Howard, K Patterson, R Frackowiak (1992). Regional response differences within the human auditory cortex when listening to words. *Neurosci. Lett.*, **146**, 179-182.

YS Ra, JH Shin, ST Kim, JH Lee, BW Kwun (2000). Cerebral Metabolic Abnormalities in Children with hydrocephalus by localized 1H MR spectrocopy. *Proceedings of the VIIIth ISMRM meeting* , Denver, USA.

GE Rees, AM Howseman, O Josephs, C Frith, K Friston (1997). Characterizing the relationship between BOLD fMRI contrast and cerebral blood flow by varying stimulus presentation rate. *Proceedings of the Vth ISMRM meeting,* Vancouver, Canada.

HK Richards, RM Bucknall, HC Jones, JD Pickard (1989). The uptake of [14C]deoxyglucose into brain of young rats with inherited hydrocephalus. *Exp Neurol*, **103**, 194-198.

H Rumpel, R Buchli, J Gehrmann, A Aguzzi, O Illi, E Martin (1995). Magnetic resonance imaging of brain edema in the neonatal rat: a comparison of short and long term hypoxia-ischemia. *Pediatr Res*, **38**, 113-118.

H Sakuma, Y Nomura, K Takeda, T Tagami, T Nakagawa, Y Tamagawa, et al (1991). Adult and neonatal human brain: diffusional anisotropy and myelination with diffusion-weighted MR imaging. *Radiology*, **180**, 229-233.

JS Schoeniger, NR Aiken, E Hsu, SJ Blackband (1994). Relaxation-time and diffusion NMR microscopy of single neurons. *J.Magn Reson B*, **103**, 261-273.

CL Shoesmith, R Buist, MR Del Bigio (2000). MR Magnetic resonance imaging study of extracellular fluid tracer movement in brains of immature rats with hydrocephalus. *Neurol Res*, **22**, 111-116.

Y Shtyrov, T Kujala , J Ahveninen, M Tervaniemi, P Alku, RJ Ilmoniemi,- R Naatanen (1998). Background acoustic noise and the hemispheric lateralization of speech processing in the human brain: magnetic mismatch negativity study, *Neurosc Lett*, **251**, 141-144.

H Steinmetz, G Furst, HJ Freund (1989). Cerebral Cortical Localization: Application and Validation of the Proportional Grid System in MR Imaging. *J of Comp Assis Tomo*, **13**,10-19

H Steinmetz, RJ Seitz (1991). Functional Anatomy of Language Processing: Neuroimaging and the Problem of Individual Variability. *Neuropsychologia*, **29**, 1149-1161.

EO Stejskal, JE Tanner (1965). Spin diffusion measurements: spin echoes in the presence of time-dependent field gradients. *J Chem Phys*, **42**, 288-292.

JC Strainer, JL Ulmer, FZ Yetkin, VM Haughton, DL Daniels, SJ Millen (1997). Functional MR of the primary auditory cortex: an analysis of pure tone activation and tone discrimination. *AJNR Am J Neuroradiol*, **18**, 601-610.

A Szafer, J Zhong, AW Anderson, JC Gore (1995). Diffusion-weighted imaging in tissues: theoretical models. *NMR Biomed*, **8**, 289-296.

J Talairach, G Szikla, P Tournoux (1967). *Atlas d'anatomie stereotaxique du telencephale*, Masson, Paris.

T Talavage, WB Edmister (1998). Saturation and non-linear response in auditory cortex. *Neuroimage*, **7**, S362.

RW Thatcher, C Biver, R McAlaster, A Salazar (1998). Biophysical linkage between MRI and EEG coherence in closed head injury. *Neuroimage*, **8**, 307-326.

UI Tuor, P Kozlowski, MR Del Bigio, B Ramjiawan, S Su, K Malisza, *et al.* (1998). Diffusion- and T_2-weighted increases in magnetic resonance images of immature brain during hypoxia-ischemia: transient reversal posthypoxia. *Exp Neurol*, **150**, 321-328.

DB Twieg (1983). The k-trajectory formulation of the NMR imaging process with applications in analysis and synthesis of imaging methods. *Med Phys*, **10**, 610-621.

AM Ulug, CG Filippi, M Souweidane, RD Zimmerman (1999). Use of Diffusion Imaging for Assessing the Treatment of Obstructive Hydrocephalus. *Proceedings of the VIIth ISMRM meeting*, Philadelphia, USA.

Z Vajda, E Berenyi, P Bogner, I Repa, T Doczi, E Sulyok (1999). Brain adaptation to water loading in rabbits as assessed by NMR relaxometry. *Pediatr Res*, **46**, 450-454.

A Van der Toorn, RM Dijkuizen, CA Tulleken, K Nicolay (1996). Diffusion of metabolites in normal and ischemic rat brain measured by localized 1H MRS. *Magn Reson Med*, **36**, 914-922.

KP Whittall, AL MacKay, DA Graeb, RA Nugent, DK Li, DW Paty (1997). In vivo measurement of T_2 distributions and water contents in normal human brain. *Magn Reson Med*, **37**, 34-43.

KP Whittall, AL MacKay, DK Li (1999). Are mono-exponential fits to a few echoes sufficient to determine T2 relaxation for in vivo human brain?. *Magn Reson Med*, **41**, 1255-1257.

CF Williams, TW Redpath, FW Smith (1996). The influence of stimulated echoes on contrast in fast spin-echo imaging. *Magn Reson Im*, **14**, 419-428.

R Wise, F Chollet, U Hadar, K Friston, E Hoffner, K Frackowiak (1991). Distribution of cortical neural networks involved in word comprehension and word retrieval, *Brain*, **114**, 1805-1817.

FZ Yetkin, TL McAuliffe, RW Cox, and VM Haughton (1996). Test-retest precision of functional MR in sensory and motor task activation, *AJNR. Am J Neuroradiol,* **17**, 95-98.

RJ Zatorre, AC Evans, E Meyer, A Gjedde (1992). Lateralization of phonetic and pitch discrimination in speech processing. *Science*, **256**, 846-849.

BIOGRAPHICAL SKETCH.

Cécile M. Mohr was born in Nancy, France, on December 27, 1972. She completed her high school degree in 1990 in Grenoble, France, and pursued with the "classes préparatoires aux grandes écoles" at the lycée Champollion in Grenoble. In 1992, she entered the Ecole Nationale Supérieure de Physique de Grenoble (ENSPG), where she specialized in nuclear engineering. For her last year of ENSPG, two French fellowships allowed her to join the University of Florida department of Nuclear and Radiological Sciences. After completing her French degree in 1995, she stayed at the University of Florida and completed her Master of Science in medical physics in 1997. she pursued her studies and, with the support of Dr. Christiana Leonard, joined the laboratory of Dr. Stephen Blackband at the University of Florida Brain Institute. There, she worked both on functional magnetic resonance imaging techniques and the development of *in vivo* quantitative magnetic resonance methods to study the brain. In May 2000, she received her Ph.D. in medical physics from the University of Florida.

Cécile plans to work in the exciting field of medical imaging and her goal in life is to balance both an exciting career and quality time with friends and family.

I certify that I have read this study and that in my opinion it conforms to acceptable standards of scholarly presentation and is fully adequate, in scope and quality, as a dissertation for the degree of Doctor of Philosophy.

Wesley E. Bolch

Wesley E. Bolch, Chairman
Associate Professor of Nuclear and
Radiological Engineering

I certify that I have read this study and that in my opinion it conforms to acceptable standards of scholarly presentation and is fully adequate, in scope and quality, as a dissertation for the degree of Doctor of Philosophy.

Stephen J. Blackband
Associate Professor of Neuroscience

I certify that I have read this study and that in my opinion it conforms to acceptable standards of scholarly presentation and is fully adequate, in scope and quality, as a dissertation for the degree of Doctor of Philosophy.

Jeffrey R. Fitzsimmons
Professor of Nuclear and Radiological
Engineering

I certify that I have read this study and that in my opinion it conforms to acceptable standards of scholarly presentation and is fully adequate, in scope and quality, as a dissertation for the degree of Doctor of Philosophy.

David E. Hintenlang
Associate Professor of Nuclear and
Radiological Engineering

I certify that I have read this study and that in my opinion it conforms to acceptable standards of scholarly presentation and is fully adequate, in scope and quality, as a dissertation for the degree of Doctor of Philosophy.

Hazel C Jones

Hazel C. Jones
Research Professor of Pharmacology and
Therapeutics

I certify that I have read this study and that in my opinion it conforms to acceptable standards of scholarly presentation and is fully adequate, in scope and quality, as a dissertation for the degree of Doctor of Philosophy.

Christiana M Leonard

Christiana M. Leonard
Professor of Neuroscience

This dissertation was submitted to the Graduate Faculty of the College of Engineering and to the Graduate School and was accepted as partial fulfillment of the requirements for the degree of Doctor of Philosophy.

May 2000

M. J. Ohanian
Dean, College of Engineering

Winfred M. Phillips
Dean, Graduate School